Manuscrit d'Habilitation à Diriger des Recherches
(Université Joseph Fourier - Grenoble I)

Antennes optiques à base de fils photoniques : concepts fondamentaux et applications à l'optique quantique

Julien Claudon

Equipe mixte CEA-CNRS *Nanophysique et Semiconducteurs*,
CEA/INAC/SP2M, Grenoble

Soutenance prévue le 1er juillet 2014 devant le jury suivant :

Jean-Jacques Greffet,	Professeur (Rapporteur) Université Paris-Sud, Institut d'Optique (Palaiseau)
Pascale Senellart,	Directeur de Recherche CNRS (Raporteur) Laboratoire de Photonique et de Nanostructures (Marcoussis)
Pierre Viktorovitch,	Directeur de Recherche CNRS (Rapporteur) Institut des Nanotechnologies de Lyon
Vahid Sandoghdar,	Professeur Max Planck Institute for the Science of Light (Erlangen)
Benoit Boulanger,	Professeur Université Joseph Fourier (Grenoble I), Institut Néel

Table des matières

Avant-propos

Contexte. J'ai été recruté en décembre 2006 comme chercheur CEA au sein de l'équipe mixte CEA-CNRS "NanoPhysique et SemiConducteurs" (NPSC), à Grenoble. Plus précisément, j'ai rejoint l'équipe "nanophotonique arséniures" animée par Jean-Michel Gérard. Je développe en particulier des structures photoniques qui permettent de contrôler efficacement l'émission spontanée d'un émetteur. Ces recherches conjuguent des aspects fondamentaux, comme le contrôle de l'interaction lumière-matière, et des perspectives plus appliquées, comme le développement de dispositifs opto-électroniques innovants (sources de photons uniques très brillantes, microlasers à bas seuils...). Dans ce contexte, les hétérostructures semiconductrices appartenant à la famille des arséniures présentent un double intérêt. Tout d'abord, les boîtes quantiques InAs/GaAs réalisées par croissance épitaxiale constituent des atomes artificiels mésoscopiques aux propriétés très attractives avec une émission rapide, efficace et monochromatique à basse température. D'autre part, la structuration des semiconducteurs GaAlAs par diverses techniques de salle blanche est aujourd'hui très avancée — et d'ailleurs toujours en constant progrès. Cette maturité technologique offre une très grande liberté pour structurer l'environnement électromagnétique de la boîte en l'intégrant par exemple dans une microcavité ou un guide d'onde monomode.

Choix des résultats présentés. Depuis mon arrivée au CEA, j'ai principalement contribué à deux thématiques scientifiques : la réalisation et l'étude de microlasers à modes de galerie employant un ensemble de boîtes quantiques comme milieu à gain et le développement d'antennes optiques à base de fils photoniques. J'ai également été impliqué dans d'autres activités, surtout à travers la réalisation d'échantillons : la génération non-linéaire de rayonnement THz dans une microcavité (collaboration avec le groupe de Giuseppe Leo, Laboratoire Matériaux et Phénomènes Quantiques, Paris) et des projets explorant la commutation optique ultrarapide d'une microcavité (collaboration avec le groupe de Willem Vos, Université de Twente, Pays-Bas). Dans ce manuscrit, j'ai choisi de développer uniquement les travaux portant sur les antennes à fil photonique.

Organisation de l'équipe, collaborations. Chacune des réalisations présentées dans ce manuscrit implique une étape de design, un effort de fabrication (croissance par épitaxie par jets moléculaires et structuration des échantillons en salle blanche) et enfin une étude optique sur un banc de micro-photoluminescence cryogénique. Les résultats présentés dans ce manuscrit sont ainsi le fruit d'un travail d'équipe, qui a en particulier impliqué trois

chercheurs de l'équipe NPSC : Joël Bleuse, Jean-Michel Gérard et moi-même. Tous les calculs numériques nécessaires au design des structures ont été réalisés par Niels Gregersen (DTU Fotonik, Danemark) et Philippe Lalanne (Institut d'Optique, Bordeaux).

A titre personnel, j'ai tout d'abord fortement contribué à développer la micro/nano structuration des échantillons en salle blanche. Cette structuration définit directement l'environnement électromagnétique de l'émetteur, et régit donc son émission spontanée. Il s'agit d'une étape décisive pour toutes les études que nous menons, relativement peu développée avant mon arrivée. J'ai ainsi travaillé successivement au sein des salles blanches PROMES, CEA/LETI/DOPT et au sein de la Plate-forme de Technologie Amont (PTA). J'ai co-encadré (avec Jean-Michel Gérard), la thèse de Nitin Singh Malik (2008 - 2011), qui a permis de réaliser pour la première fois des antennes à fils photoniques de type "aiguille" et "trompette". Les objets décrits dans ce manuscrit ont été obtenus à partir de structures épitaxiales planaires, dont la croissance à été réalisée par Maela Bazin, Périne Jaffrennou, Marion Ducruet et Emmanuel Dupuy.

Je m'intéresse également au design et à la physique des structures, en utilisant dans une première approche des modèles analytiques ou semi-analytiques. Bien sûr, l'étude rigoureuse d'une nanostructure photonique peut rarement être conduite "sur un coin de table", et nécessite la mise en œuvre de méthodes numériques dédiées. J'ai eu la chance de pouvoir collaborer avec Niels Gregersen et Philippe Lalanne : ils utilisent tous deux des méthodes numériques permettant d'accéder à une vision "microscopique" du comportement de la lumière dans les différents éléments de la structure photonique, ce qui permet de guider très efficacement le design.

Les mesures optiques sur la première génération d'antenne ont été réalisées par Joël Bleuse. Les fils photoniques elliptiques et les trompettes photoniques ont été étudiés par Mathieu Munsch, qui a réalisé un postdoc dans l'équipe (2010-2012) et avec qui j'ai beaucoup interagi.

Enfin, j'ai rédigé la plupart des articles décrivant les résultats expérimentaux obtenus sur les fils photoniques, et je suis impliqué dans la rédaction et le suivi de plusieurs contrats de recherche obtenus par l'équipe (Fondation Nanosciences, ANR, Europe).

Organisation du manuscrit. Ce manuscrit s'articule autour de quatre chapitres. Le chapitre introductif présente tout d'abord les motivations associées au contrôle de l'émission spontanée en phase condensée, en se focalisant sur l'obtention d'une émission spontanée monomode. Dans ce contexte, il détaille plus particulièrement l'intérêt des microcavités optiques et de certaines classes de guides d'ondes optiques. Le second chapitre décrit la dynamique d'émission spontanée dans un fil photonique, en s'appuyant sur une combinaison de résultats théoriques et expérimentaux. Le troisième chapitre montre comment, en structurant les extrémités d'un fil photonique, on peut réaliser une antenne optique très performante, qui extrait l'émission d'une source lumière ponctuelle et la structure en un faisceau directif. Comme première application dans le domaine de l'optique quantique, nous avons ainsi réalisé des sources de photons uniques très brillantes, en intégrant une boîte quantique spectralement isolée dans une telle antenne. Enfin, le dernier chapitre présente

quelques travaux en cours et explore quelques pistes de travaux futurs.

Langues utilisées. Les chapitres 1, 2 et 3 sont rédigés en anglais, le chapitre final qui décrit quelques perspectives de recherche à moyen terme est rédigé en français.

Chapitre 1

Introduction

Together with absorption and stimulated emission, spontaneous emission is one of the three fundamental mechanisms that govern light-matter interaction. In this introductory chapter, we briefly recall the basics of this process, and show how it can be controlled with a proper engineering of the electromagnetic environment seen by the emitter. We focus on solid-state systems build out of semiconductor heterostructures, for which such a control combines a fundamental interest with appealing application prospects. In particular, we discuss how single-mode spontaneous emission can be achieved using microcavities and certain kinds of waveguides. Finally, the chapter introduces photonic wires, a class of high-index waveguides that feature key assets for a broadband control of spontaneous emission.

1.1 Spontaneous emission in tailored electromagnetic environments

Spontaneous emission (SE) is the random and irreversible decay of an electronic excited state, which relaxes towards a lower energy state by emitting a photon. This decay is induced by the coupling of an optically active transition to the vacuum electric field fluctuations associated with a continuum of optical modes. After a few elements of theory (section 1.1.1), we consider the coupling of a point-like, two-level emitter to three distinct electromagnetic environments : the 3D continuum of propagating modes supported by a bulk dielectric material (section 1.1.2), a localized quasi-mode confined by an optical cavity (section 1.1.3) and the 1D continuum of propagating modes associated with a single-mode waveguide (section 1.1.4). These results will serve as a basis for the next section, which discusses single-mode spontaneous emission in solid-state photonic structures.

1.1.1 Elements of theory

We consider a two-level atom whose excited state $|e\rangle$ and ground state $|g\rangle$ are separated by an energy $\hbar\omega_{\mathrm{em}}$; the corresponding vacuum wavelength is λ_{em}. The emitter is point-like (very small as compared to λ_{em}) and light-matter interaction is restricted to the dipolar

order. The interaction Hamiltonian with the electromagnetic field then takes the form $-\hat{\mathbf{d}}.\hat{\mathbf{E}}(\mathbf{r}_{\rm em})$, with $\hat{\mathbf{d}}$ the atomic dipole operator and $\hat{\mathbf{E}}(\mathbf{r}_{\rm em})$ the electric field operator at the location $\mathbf{r}_{\rm em}$ of the emitter. We now consider a continuum of electromagnetic modes $\{\mu\}$ that feature the same electrical field amplitude and the same polarization at the location of the emitter. The atom is initially in its excited state $|e\rangle$ and the field modes are in their vacuum state $|0\rangle$. According to the Fermi Golden rule, the population of $|e\rangle$ decays exponentially in time with a rate Γ_μ given by :

$$\Gamma_\mu = \frac{2\pi}{\hbar^2}\left|\langle e,0| - \hat{\mathbf{d}}.\hat{\mathbf{E}}(\mathbf{r}_{\rm em})|g,1\rangle\right|^2 \rho_\mu(\omega_{\rm em}). \tag{1.1}$$

We assume in the following a linear dipole for the optical transition. To separate the contributions associated with the emitter and the ones associated with its environment, Eq 1.1 can be rewritten as :

$$\Gamma_\mu = \frac{2\pi}{\hbar^2}\big(d_{\rm em}^2 \times \cos^2\theta \times E_{\rm zpf}^2(\mathbf{r}_{\rm em}) \times \rho_\mu(\omega_{\rm em})\big), \tag{1.2}$$

with $d_{\rm em}^2 = |\langle e|\hat{\mathbf{d}}|g\rangle|^2$. The influence of the electromagnetic environment on Γ_μ is apparent through two terms : $\rho_\mu(\omega_{\rm em})$, the spectral density of optical states *at the emitter frequency* and $E_{\rm zpf}^2(\mathbf{r}_{\rm em}) = |\langle 0|\hat{\mathbf{E}}(\mathbf{r}_{\rm em})|1\rangle|^2$, the intensity of the zero-point fluctuations associated with one mode *at the emitter location*. Finally, the light-matter coupling also depends on the relative alignment of the atomic dipole with the local field polarization ($\cos^2\theta$ factor).

As first envisioned by Purcell when considering the coupling to a resonant cavity [81], a proper engineering of the photonic environment allows controlling ρ_μ and $E_{\rm zpf}^2$, and thus Γ_μ. In the following, this point will be illustrated by successively considering an emitter coupled to to a 3D continuum of states, a localized (0D) cavity mode and a 1D continuum associated with a propagating guided mode (Fig. 1.1). We will not enter into the full details of the field quantization : we provide the mode structure obtained from classical electromagnetism and the associated spectral density. The local intensity of the zero-point fluctuations is obtained from a semi-classical argument, by normalizing the electromagnetic energy of one mode to $\frac{1}{2}\hbar\omega$.

1.1.2 Spontaneous emission in bulk material

We first consider an atom immersed in a linear, homogeneous, isotropic dielectric material. This simple case is generally taken as a reference to assess the modification of spontaneous emission in more complex electromagnetic environments. The material features a refractive index n and dispersion effects are neglected ($\mathrm{d}n/\mathrm{d}\omega = 0$). The associated electromagnetic environment can be decomposed as an infinite set of propagating plane waves characterized by their wave vector $\mathbf{k}$ and their linear polarization vector. They satisfy the linear dispersion relation $\omega = \frac{c}{n}|\mathbf{k}|$, with c the speed of light in vacuum. For the sake of calculations, we consider a finite volume V of material ($V \gg \lambda_{\rm em}^3$) and apply periodic boundary conditions. For one plane wave, the zero-point fluctuations at the emitter

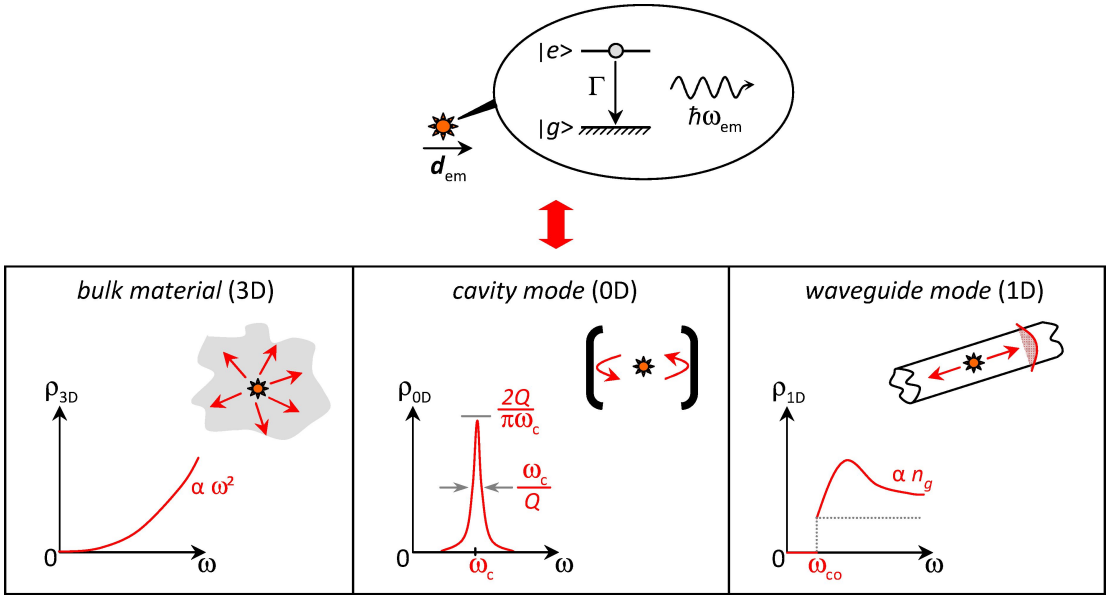

FIGURE 1.1 – **Spontaneous emission in three photonic environments.** We sketch the important parameters that characterize the emitter and the density of optical states associated with each environment.

location read $E_{\mathrm{zpf}}^2 = \frac{\hbar\omega_{\mathrm{em}}}{2\epsilon_0 n^2 V}$, with ϵ_0 the dielectric permittivity of vacuum. Including the two-fold polarization degeneracy, the spectral density of modes reads :

$$\rho_{3\mathrm{D}}(\omega) = \frac{\omega^2 n^3 V}{\pi^2 c^3}, \tag{1.3}$$

which leads to the SE decay rate :

$$\Gamma_0 = \frac{d_{\mathrm{em}}^2 \omega_{\mathrm{em}}^3 n}{3\pi\hbar\epsilon_0 c^3}. \tag{1.4}$$

In this final expression, the material volume V disappears. The factor $1/3$ is due to the averaging over all the relative dipole-polarization orientations. Note that Γ_0 is proportional to the cube of the emitter frequency, and to the refractive index of the host material.

1.1.3 Coupling to a localized cavity mode

The enhancement of spontaneous emission resulting from the resonant coupling to a cavity mode was first proposed by Purcell, as early as in 1946 [81]. An optical cavity confines light in the three directions of space, thus giving rise to a discrete energy spectrum. We focus on a single optical resonance characterized by its angular frequency ω_c and a spatial distribution of the electrical field $\mathbf{E}(\mathbf{r})$. In a real cavity, photons remain trapped during a finite mean time $\tau_c = Q\omega_c$, where Q is the quality factor of the cavity resonance. In the frequency domain, the finite storage time translates into a spectral broadening : each

mode features a Lorentzian profile with a full width at half maximum $\Delta\omega_c = \omega_c/Q$. In the so-called weak coupling regime of cavity quantum electrodynamics, the lossy cavity mode can be treated as a quasi-mode, *i.e.* a continuum with a spectral density of states characterized by a Lorentzian profile :

$$\rho_{0\mathrm{D}}(\omega) = \frac{2Q}{\pi\omega_c} \frac{\left(\frac{\omega_c}{2Q}\right)^2}{(\omega-\omega_c)^2 + \left(\frac{\omega_c}{2Q}\right)^2}, \tag{1.5}$$

which satisfies the normalization condition $\int \rho_{0\mathrm{D}}(\omega)\mathrm{d}\omega = 1$. In the weak coupling regime, the radiative relaxation of the emitter into the cavity mode remains an irreversible process. The corresponding SE rate reaches a maximum $\Gamma_{\mathrm{cav}}^{\mathrm{max}}$ when the cavity-emitter coupling is optimal, which implies three conditions. First, the emitter frequency should match the cavity resonance, to maximize the density of state : $\rho_{0\mathrm{D}}^{\mathrm{max}} = \rho_{0\mathrm{D}}(\omega_c) = \frac{2Q}{\pi\omega_c}$. Second, the emitter should be located on a maximum of the electrical field. Noting n the refractive index at this location, the maximum amplitude of zero-point fluctuations can be written as :

$$E_{\mathrm{zpf}}^{\mathrm{max}} = \sqrt{\frac{\hbar\omega_{\mathrm{em}}}{2\epsilon_0 n^2 V_{\mathrm{eff}}}}, \quad \text{with} \quad V_{\mathrm{eff}} = \frac{\iiint n(\mathbf{r})^2 |\mathbf{E}(\mathbf{r})|^2 \mathrm{d}^3\mathbf{r}}{n^2 \max|\mathbf{E}(\mathbf{r})|^2}. \tag{1.6}$$

Here, V_{eff} characterizes the spatial confinement of the cavity mode. Finally, the emitter optical dipole should be aligned along the local mode polarization at the electrical field maximum. When these three conditions are simultaneously fulfilled, one obtains :

$$\Gamma_{\mathrm{cav}}^{\mathrm{max}} = \frac{2d_{\mathrm{em}}^2 Q}{\hbar\epsilon_0 n^2 V_{\mathrm{eff}}}. \tag{1.7}$$

To quantify the enhancement of spontaneous emission into the cavity mode, one generally introduces the Purcell factor $F_p = \Gamma_{\mathrm{cav}}^{\mathrm{max}}/\Gamma_0$, where Γ_0 is the emission rate of the same emitter immersed in a bulk material with a refractive index n (see section 1.1.2) :

$$F_p = \frac{3}{4\pi^2} \frac{Q(\lambda_c/n)^3}{V_{\mathrm{eff}}}, \tag{1.8}$$

F_p, which only depends on the ratio Q/V_{eff}, constitutes a figure of merit of the cavity. By increasing Q and decreasing V_{eff}, it is thus possible to enhance Γ_{cav} so that it largely exceeds the bulk SE rate Γ_0. However, when the spatial and spectral matching conditions are not fulfilled, the magnitude of the effect rapidly decreases. Note also that this result is valid for a monochromatic emitter.

1.1.4 Coupling to a propagating guided mode

In a waveguide, light is free to propagate along one direction while being confined in the two transverse directions. For the sake of simplicity, we consider an infinite waveguide that supports a single family of guided modes. Assuming a propagation along the z axis with a scalar propagation constant k_z, the electrical field associated to a guided mode

takes the general form $\mathbf{E}(\mathbf{r}_\perp)\exp[j(\omega t - k_z z)]$, with $\mathbf{E}(\mathbf{r}_\perp)$ the electric field distribution in a plane perpendicular to $\hat{\mathbf{z}}$. For the sake of calculations, we consider a finite section of the waveguide, with a length $L_z \gg \lambda_{\mathrm{em}}$. Using periodic boundary conditions along the z-axis, the 1D continuum of guided modes is characterized by the spectral density :

$$\rho_{1\mathrm{D}}(\omega) = \begin{cases} 0 & \text{if } \omega < \omega_{\mathrm{co}} \\ \frac{L_z}{\pi|v_g(\omega)|} & \text{if } \omega \geq \omega_{\mathrm{co}} \end{cases}, \tag{1.9}$$

where $v_g = \mathrm{d}\omega/\mathrm{d}k_z$ is the group velocity of the guided mode. This expression includes the two counter propagating guided modes. Above a possible cut-off at an angular frequency ω_{co}, a point-like optical dipole integrated inside the structure will always experience a coupling to guided modes.

We now evaluate $\Gamma_{\mathrm{wg}}^{\mathrm{max}}$, the maximum emission rate into the guided mode. If one excludes slow-light structures, in which v_g can be much smaller than c over a generally narrow spectral region, $\rho_{1\mathrm{D}}$ features a weak spectral dependence. When this spectral dependence is neglected, two conditions remain. First, the emitter should be located on a maximum of the electrical field ; we note n the refractive index at this location. The amplitude of zero-point fluctuation associated with one guided mode then reaches :

$$E_{\mathrm{zpf}}^{\mathrm{max}} = \sqrt{\frac{\hbar\omega_{\mathrm{em}}}{2\epsilon_0 n^2 L_z S_{\mathrm{eff}}}} \quad \text{with} \quad S_{\mathrm{eff}} = \frac{\iint n(\mathbf{r}_\perp)^2 |\mathbf{E}(\mathbf{r}_\perp)|^2 \mathrm{d}^2\mathbf{r}_\perp}{n^2 \mathrm{max}|\mathbf{E}(\mathbf{r}_\perp)|^2}. \tag{1.10}$$

S_{eff} characterizes the transverse confinement of the guided mode. Second, the emitter dipole should be aligned along the local mode polarization. When these two conditions are fulfilled, one obtains :

$$\Gamma_{\mathrm{wg}}^{\mathrm{max}} = \frac{d_{\mathrm{em}}^2 \omega_{\mathrm{em}}}{\hbar\epsilon_0 n^2 S_{\mathrm{eff}} |v_g|}. \tag{1.11}$$

As expected, L_z has disappeared from this expression. Similarly than for the cavity case, one defines the waveguide generalized Purcell factor $F_{\mathrm{p,wg}} = \Gamma_{\mathrm{wg}}^{\mathrm{max}}/\Gamma_0$:

$$F_{\mathrm{p,wg}} = \frac{3}{4\pi} \frac{(\lambda_{\mathrm{em}}/n)^2}{S_{\mathrm{eff}}} \frac{n_{\mathrm{g}}}{n}. \tag{1.12}$$

Here, $n_g = c/|v_g|$ is the group index of the guided mode. Eq. 1.12 defines a figure of merit for the SE coupling to a guided mode and shows a profound analogy with the Purcell factor of a cavity. We have indeed the correspondences $S_{\mathrm{eff}} \leftrightarrow V_{\mathrm{eff}}$ (spatial mode confinement) and $n_g/n \leftrightarrow Q$ (density of states). To maximize $F_{\mathrm{p,wg}}$, one should minimize S_{eff} and maximize the group index. In the next section, we use these theoretical results to show how single-mode spontaneous emission can be achieved in a solid-state environment using optical microcavities and single-mode waveguides.

1.2 Single-mode spontaneous emission in the solid state

1.2.1 Motivations

Spontaneous emission control (and especially single-mode emission) offered by solid-state photonic systems combines a fundamental interest with appealing application prospects. On the one hand, a solid-state structure provides a monolithic and convenient platform to investigate light-matter interaction. On the other hand, as first noted by Yablonovitch in a seminal paper [112], spontaneous emission control can vastly improve the performance of various optoelectronic devices, including light emitting diodes, semiconductor lasers, photovoltaic cells or quantum-light sources.

We focus here on solid-state structures that define a single-mode environment around a point-like artificial atom, such as a semiconductor quantum dot. This strategy first allows collecting a large fraction of the artificial atom emission, and thus represents an appealing route for improving the brightness of quantum light sources [71, 72, 78, 88, 103, 95]. Reversibly, a photon impinging on the emitter will be efficiently absorbed, opening possibilities for the realization of single-photon switches [27, 84, 63, 106, 13]. More generally, the coupling between a single optical mode and a single atom-like emitter lies at the root of a wide range of elegant quantum optics experiments and may constitute the node of future quantum networks. In such a "quantum internet", one hopes to control complex quantum state superpositions in arrays of localized quantum nodes which coherently exchange information by emitting and absorbing photons [52]. The first steps in this direction have been performed with quantum dots, with the recent demonstration of entanglement between a localized spin trapped in the dot and a propagating photon [23, 33].

The fraction β of spontaneous emission coupled to an optical mode of interest M reads [(1)] :

$$\beta = \frac{\Gamma_{\mathrm{M}}}{\Gamma_{\mathrm{M}} + \gamma}, \tag{1.13}$$

with Γ_{M} the spontaneous emission rate into M and γ the emission rate into the whole continuum of other modes. When the condition $\Gamma_{\mathrm{M}} \gg \gamma$ is fulfilled, a large fraction of spontaneous emission is dynamically funneled into a single optical channel. A first route to bring β close to 1 consists in enhancing Γ_{M}, the emission rate into the mode of interest. In practice, this can be achieved by coupling the emitter to a localized mode, by using slow-light effects and/or by exploiting a strong spatial confinement of the mode. Alternatively, one can also suppress the emission in the "unwanted" modes. This second approach is in general very challenging, both from design and experimental point of views, because it requires a control over a 3D continuum of modes. Three decades ago, these ideas gave birth to photonic crystals, which feature a bandgap of forbidden photonic states. Alternatively, a strong inhibition of SE can also be obtained in much simpler structures, such as the photonic wires investigated in this manuscript which exploit a dielectric screening effect. In the following we show how single-mode emission can be obtained in two important classes of structures : optical microcavities and certain kinds of single-mode waveguides.

(1). We neglect here non-radiative decay channels.

1.2.2 Purcell effect and optical microcavities

In most microcavities, the coupling rate γ to radiation modes is on the order of Γ_0. Thus, achieving an emission rate into the cavity mode $\Gamma_{\text{cav}} \sim 10 \times \Gamma_0$ is sufficient to ensure a nearly perfect single-mode emission ($\beta > 0.9$). Fifteen years after the first demonstration of the Purcell effect in atomic physics [41], a significant acceleration of SE in the optical domain was demonstrated for an ensemble of semiconductor quantum dots integrated in a micropillar cavity (averaged $\Gamma_{\text{cav}}/\Gamma_0 = 4$, corresponding to $F_p = 32$, Ref. [37]). Two technological advances critically contributed to this success : i) the development of optically active quantum dots (QD), which feature sharp emission lines at cryogenic temperature and ii) the progresses in the structuration of semiconductor materials at the micro/nano scale, which allowed defining a high-Q microcavity around the emitter. Some years later, this first demonstration was followed by experiments with a *single* QD coupled to a micropillar [91], a microdisk [71] and a photonic crystal cavity [28]. When such a cavity features a directive far-field emission (this is in particular the case for VCSEL-like and micropillar cavities) bright single-photon sources can be realized [71, 72, 78, 88, 95, 34].

Though very successful to bring β close to 1, the cavity-based approach however suffers from limitations which are intrinsically associated with its resonant nature [(2)]. In the references mentioned above, Q typically exceeds 10^3, meaning that the associated relative operation bandwidth is below 10^{-3}. By changing the temperature, the resonance energy of a self-assembled InAs QD can be tuned over ~ 1 meV. Since the fundamental emission is inhomogeneously dispersed over 50 meV, only a small fraction of the dots can be tuned on resonance. When further considering the random location of the emitter, the device fabrication yield drops in the $10^{-2} - 10^{-3}$ range. This not only made the first experiments with single emitters very "painful", but also hindered the development of more complex systems. Nowdays, this severe practical issue has been solved by the advent of deterministic fabrication techniques, which allows defining a spectrally-matched cavity around a selected single QD [8, 24]. Nevertheless, optimal SE control is achieved when the emitter is monochromatic as compared to $\Delta\omega_c$ [(3)]. Thus, this approach is in general less efficient for spectrally-broad emitters, such as QDs operated at room temperature or colored centers in diamond. Similarly, the simultaneous collection of several detuned transitions imposes the use of multi-resonant cavities, which, despite a recent demonstration [25], remains rather complex. As a last example, future developments of linear optics quantum computing schemes [53] will likely require a large number of single-photon sources that are spectrally matched. Because it is difficult to tune a monolithic solid-state cavity, the realization of a simultaneously bright and widely tuneable single-photon source with this approach seems

(2). The interest of microcavities extends well beyond the Purcell effect, which appears in the so-called "weak coupling" limit of cavity quantum electrodynamics. By increasing the light-matter coupling and decreasing the losses (often dominated by the photonic part) one enters the "strong coupling" regime, where the emitter and the cavity coherently and reversibly exchange a photon [118, 85, 80]. This rich physics lies beyond the scope of the present manuscript, but it is clear that a single mesoscopic atom coupled to a microcavity constitutes one of the central paradigm of (solid-state) quantum optics.

(3). If the emitter homogeneous linewidth $\Delta\omega_{\text{em}}$ is much larger than $\Delta\omega_c$, the cavity Q-factor appearing in Eq. 1.8 should be replaced by the emitter Q-factor $\omega_{\text{em}}/\Delta\omega_{\text{em}}$, see Ref. [6].

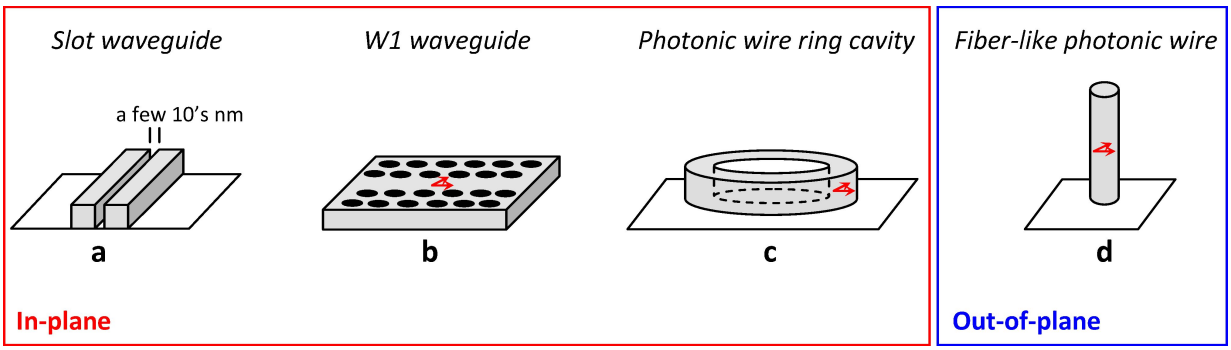

FIGURE 1.2 – **Dielectric waveguides for single-mode emission.** (a) Slot waveguide : For a guided mode with an in-plane, transverse polarization, the electrical field is confined in the tiny void between the two waveguides (proposals : Refs. [4, 82]). (b) W1 waveguide defined by removing a line of holes in a photonic crystal membrane (proposals : Refs. [66, 57], experiment : Ref. [64]). (c) Planar cavity formed with a closed photonic wire (proposal : Ref. [20], experiment : Ref. [121]). (d) Out-of plane, fiber-like photonic wire investigated in this manuscript. The red arrows indicate the orientation of the QD optical dipoles, for a growth axis perpendicular to the substrate.

quite challenging. All these points constitute a strong motivation to explore alternative, non-resonant strategies for SE control. In this perspective, using an optical waveguide instead of a resonant cavity is a natural solution for increasing the available operation bandwidth.

1.2.3 Single-mode emission in waveguides

Plasmonic and dielectric slot waveguides. A waveguide ensuring a strong transverse confinement of the guided mode [$S_{\text{eff}} \ll (\lambda_{\text{em}}/n)^2$] ensures $\Gamma_{\text{wg}} \gg \Gamma_0$. Similarly than in the microcavity case, this leads to $\beta \to 1$, however over a large operation bandwidth. Along this line, plasmonic waveguides have been extensively investigated [1, 40, 17, 32], but the issue of absorption losses has proven rather difficult to overcome [40, 17, 32]. More recently, dielectric slot waveguides have also been proposed (Fig. 1.2(a), Refs. [4, 82]). For a transverse polarization, the electric field is highly confined in the tiny void which separates the waveguides. This system looks promising, however a demonstration of this strategy with a solid-state emitter has not been reported yet.

Photonic crystal waveguides. Instead of increasing Γ_{wg}, single-mode emission can also be achieved through a pronounced inhibition of the SE into the whole continuum of radiation modes. Indeed, if $\gamma \ll \Gamma_0$, a decent coupling to the guided mode ($\Gamma_{\text{wg}} \sim \Gamma_0$), easily achieved with dielectric confinement, is sufficient to ensure $\beta \to 1$. More than twenty years ago, these considerations have motivated the proposal of a 3D photonic bandgap structure, host for a single-mode line defect [113]. Today, even though the quality of 3D photonic crystals improves steadily [5, 59], the realization of such complex structures remains a

technological challenge. Fortunately, high β's can also be obtained with much simpler geometries, albeit with some constraints on the emitter polarization. Indeed, $\beta = 0.89$ was demonstrated with quantum dots integrated in a W1 waveguide defined in photonic crystal membrane (Fig. 1.2(b), Refs. [66, 57, 64]). Moreover, slow-light effects, occurring for example near the edges of the Brillouin zone, can also be exploited to enhance Γ_{wg} [105]. This however comes at a price : a very low group velocity implies a smaller operation bandwidth and a large sensitivity to photonic disorder [70]. Fortunately, these issues can be mitigated in dispersion engineered waveguides, to obtain a moderate group index on a larger bandwidth [61]. Globally, these structures constitute very promising building blocks for future integrated photonic quantum chips.

In-plane and out-of-plane photonic wires. Photonic wires offer a very simple alternative to photonic crystal waveguides. These high index waveguides were initially proposed and demonstrated in the context of planar, high-β microlasers, using a quantum well as a gain medium (Fig. 1.2(c), Refs. [20, 121]). Similarly than for photonic crystal waveguides, the planar wire geometry is well suited to realize integrated photonic chips. Note that the achievable β for a *planar* wire is however smaller than for a photonic crystal waveguide. For a transverse optical dipole, the coupling to radiation modes is strongly suppressed by a robust dielectric screening effect. This screening effect, which will discussed into more details in the next chapter, is however absent for a longitudinal dipole. For an embedded QW (or QD), this leads to a maximum β of 0.65 (see Ref. 11 in [57]).

Building on the pioneering work of Refs. [20, 121], this manuscript presents recent achievements with fiber-like photonic wires that embed self-assembled QDs. Our main objective is to optimize the collection of light in the far-field : a "vertical" wire, perpendicular to the substrate, is then a natural choice [Fig. 1.2(d)]. Moreover, if the wire axis coincides with the growth axis, the two optical dipole components of self-assembled QDs are now perpendicular to the wire axis. The limitation imposed by the longitudinal polarization is then bypassed and β's up to 0.95 can be achieved in an infinitely-long wire [31, 11]. Finally, the far-field emission of the wire can be shaped into a directive beam through a proper engineering of its terminations (*ie* by integrating a bottom mirror and a top taper). The resulting nanowire antenna [(4)] represents an appealing opportunity for efficiently harnessing light emission or detection [42, 30, 31]. This manuscript mostly focuses on the field of solid-state quantum optics and the realization of bright sources of quantum light. However, the concepts that will be developed in the next chapters may be relevant for other optoelectronics applications, including light emitting diodes, microlasers and photovoltaic cells [62, 115].

(4). An antenna is a device that couples an electromagnetic dipole to a directive far-field beam. This concept is thus not restricted to metallic structures, which are often employed for radiofrequency dipoles. Generally speaking, an antenna can be realized with dielectric materials, or with a combination of metal and dielectrics.

Chapitre 2

Spontaneous emission dynamics in a photonic wire

A fiber-like photonic wire is a cylindrical waveguide made of a dielectric material with a large refractive index n and surrounded by a cladding with a low index n_c. Specifically, we consider here a GaAs wire ($n = 3.45$) immersed in a vacuum background ($n_c = 1$). We are interested in the monomode regime where only the fundamental guided mode (HE_{11}) is supported by the wire. This situation is very simple from a conceptual point of view and also enables a straightforward far-field engineering, as described later. This chapter details the SE dynamics of an embedded emitter featuring transverse optical dipole components, a configuration which simultaneously optimizes the coupling to HE_{11} and suppresses the coupling to the 3D continuum of non-guided modes (radiation modes). In section 2.1, we first analyze theoretically the SE dynamics of a single linear dipole. In section 2.2, we build on these results to investigate the SE of an embedded QD. After reviewing recent experimental results in section 2.3, we finally show in section 2.4 how the polarization of the emitted photons can be controlled in wires having an anisotropic section.

2.1 Coupling to guided and radiation modes : theory

2.1.1 Coupling to the fundamental guided mode

Guided modes. As schematized in Fig 2.1(a), we consider an infinite wire with a circular section of diameter d. The wire axis is oriented along the z direction and we are interested in the guided modes which propagate along this direction ; the scalar propagation constant is denoted k_z. The full derivation of the mode structure can be found in Ref. [90], as well as in most classical textbooks. In a cylindrical basis (r, θ, z) adapted to the symmetry of the problem, the electromagnetic field associated with guided modes takes the general form :

$$\left\{ \begin{array}{c} \mathbf{E}(\mathbf{r},t) \\ \mathbf{H}(\mathbf{r},t) \end{array} \right\} = \left\{ \begin{array}{c} \mathbf{E}_{l,m}(r) \\ \mathbf{H}_{l,m}(r) \end{array} \right\} e^{\pm jl\theta} e^{j(\omega t - k_z z)}, \tag{2.1}$$

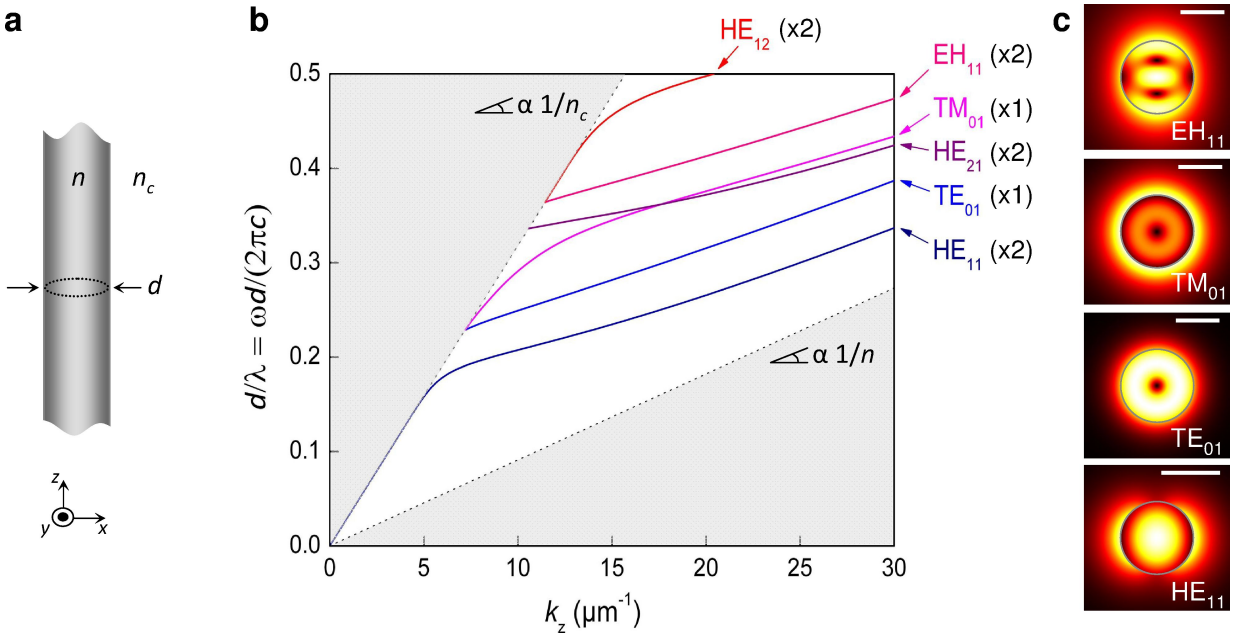

FIGURE 2.1 – **Guided modes in a GaAs wire.** (a) Waveguide geometry : we consider an infinitely-long wire having a circular section. (b) Calculated dispersion curve of the first guided modes : $d/\lambda = \omega d/(2\pi c)$ is plotted against the propagation constant k_z. The polarization degeneracy is plotted next to the mode label. (c) Map of the in-plane electrical field amplitude associated with some of the first guided modes (HE_{11}, TE_{01}, TM_{01}, and EH_{11}). The profile of HE_{11} is calculated for a reduced diameter $d/\lambda = 0.25$, with λ the free space wavelength. For the other modes, we use $d/\lambda = 0.37$; all the scale bars represent 200 nm.

with $l \in \mathbb{N}$ and $m \in \mathbb{N}^\star$. In general, such a waveguide supports hybrid modes that are neither pure TE ($E_z = 0$) nor pure TM ($H_z = 0$). The common practice is to compare the relative magnitude of E_z and H_z for a given wire diameter : if E_z dominates, the mode is noted EH_{lm} (TM-like mode, somewhat confusing !). Alternatively, if H_z dominates it is noted HE_{lm} (TE-like mode). The only mode family that features a pure TE/TM symmetry corresponds to $l = 0$. These modes are denoted $TE_{l=0,m}$ and $TM_{l=0,m}$, with $m \geq 1$. The waveguide always supports a fundamental guided mode HE_{11}, without any cutoff. Its dispersion relation is plotted in Fig. 2.1(b), together with the one of the next guided modes : TE_{01}, TM_{01}, HE_{21}, EH_{11} and HE_{12}. Owing to the $e^{\pm jl\theta}$ factor appearing in Eq. 2.1 all these modes feature a two-fold polarization degeneracy, at the exception of TE_{01} and TM_{01} ($l = 0$).

In the following, we are interested in the monomode regime in which an emitter embedded in the wire is only coupled to the fundamental guided mode. The emitter is point-like and features a linear, transverse optical dipole with a vacuum wavelength $\lambda = 950$ nm. It will thus couple to the in-plane electric field component of the guided modes. In Fig. 2.1(c), we have plotted the in-plane amplitude (*i.e.* $[E_x^2 + E_y^2]^{1/2}$) of some of the first guided modes.

mode	HE_{11}	TE_{01} | TM_{01}	HE_{21}	EH_{11} | HE_{12}
$\left(\frac{d}{\lambda}\right)_{co}$	0	$\frac{2.405}{\pi\sqrt{n^2-n_c^2}}$	$(\star)$	$\frac{3.832}{\pi\sqrt{n^2-n_c^2}}$
	0	0.229	0.336	0.364
$\mathbf{E}(0,0)$	$\neq \mathbf{0}$	**0**		$\neq \mathbf{0}$

TABLE 2.1 – **Cutoff of the first guided modes**. The cutoff of TE_{01} and TM_{01} is proportional to the first zero of the Bessel function J_0. The cutoff of EH_{11} and HE_{12} is proportional to the first zero of J_1. For HE_{21} $(\star)$, one has to solve a slightly more complex equation, as detailed in Ref. [90]. We provide numerical values in the case of a GaAs wire surrounded by air ($n = 3.495$ and $n_c = 1$). The last line indicates the value of the electric field on the wire axis.

When appropriate, we have chosen a linear polarization basis and plotted the mode with a polarization oriented along the horizontal axis. In particular, TE_{01}, TM_{01} and HE_{21} feature a null electric field amplitude on the wire axis. An analytical expression of the mode cutoffs, as well as numerical values for a GaAs wire surrounded by air, are shown in table 2.1. For on-axis emitters, the wire remains single-mode for $d/\lambda < 0.366$, a value that corresponds to the cutoff of EH_{11}. For off-axis emitters, investigated later in paragraph 2.2, single mode operation holds for $d/\lambda < 0.229$, which corresponds to the cutoff of TE_{01} and TM_{01}.

Coupling to the fondamental guided mode(HE_{11}). We now evaluate the SE rate Γ_M into $M = HE_{11}$ for an on-axis emitter with a transverse dipole. As discussed above, HE_{11} is not a pure TE mode. In particular, for wire diameters leading to a tight transverse confinement of the mode, E_z can be rather strong when approaching the wire sidewalls. However, the mode features a transverse local polarization ($E_z = 0$) on the wire axis. At this location, the intensity of the zero-point fluctuations is inversely proportional to the effective surface :

$$S_{\text{eff}} = \frac{\iint n(x,y)^2 |\mathbf{E}(x,y)|^2 \mathrm{d}x\mathrm{d}y}{n^2 |\mathbf{E}(0,0)|^2}. \tag{2.2}$$

We use here a definition that slightly differs from the Eq. 1.10 of the introductory chapter. Equation 2.2 is well suited to evaluate the zero-point fluctuations on the wire axis : depending on the wire diameter, this location does not necessarily correspond to the absolute maximum of the electric field. With this new definition of S_{eff} (and keeping in mind that $E_z = 0$), one can use Eq. 1.12 to directly compute Γ_M/Γ_0, with Γ_0 the SE rate of the emitter immersed in bulk GaAs.

Figure 2.2 shows the relevant characteristics of HE_{11} plotted against the reduced wire diameter d/λ (note the horizontal log scale). The top panel shows S_{eff}, the middle one shows the effective index $n_{\text{eff}} = c\frac{k_z}{\omega}$ and the group index $n_g = c\frac{\mathrm{d}k_z}{\mathrm{d}\omega}$ and the bottom one shows the normalized SE rate of an on-axis emitter. When considering the mode lateral confinement, one can distinguish two limiting cases. For $d \ll \lambda/n$, the effective index n_{eff} approaches n_c : the mode is largely deconfined in the wire background. In this "bad" waveguide regime, the dispersion is asymptotically linear and the group index is very close to n_c. In this small

diameter regime, S_{eff} increases very steeply when d/λ is reduced. In the large diameter regime ($d \gg \lambda/n$), the effective index n_{eff} approaches n : most of the mode energy lies inside the wire. Asymptotically, the dispersion curve approaches the one of a plane wave propagating in the material constituting the wire. We thus have $n_g \to n$. In this regime, the mode surface S_{eff} scales approximately as d^2. As shown in the bottom panel of Fig. 2.2, the optimal SE coupling to HE_{11} is achieved for $d/\lambda \sim \lambda/n$. More precisely, for $d/\lambda = 0.235$, an optimal transverse confinement of the mode [$S_{\text{eff}} = 0.41 \times (\lambda/n)^2$] associated with a slightly increased group index ($n_{\text{g}} = 1.55 \times n$) results in a maximal emission rate $\Gamma_{\text{M}} = 0.9 \times \Gamma_0$. This value, close to the one obtained in bulk GaAs, is the signature of a good coupling between the emitter and the guided mode.

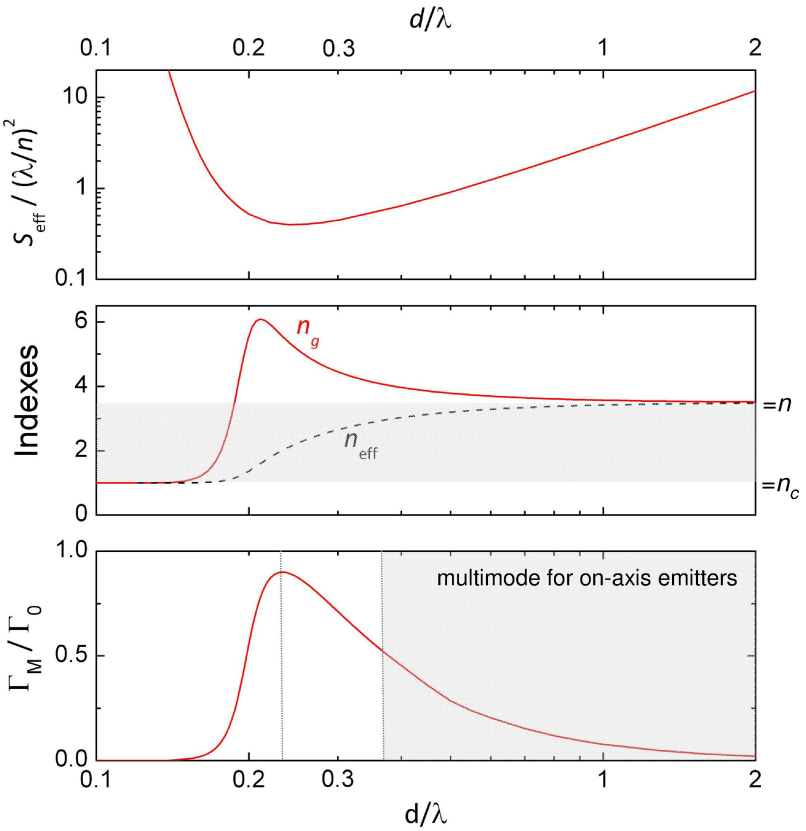

FIGURE 2.2 – **Coupling to HE_{11}.** We consider an infinite wire of diameter d. All quantities are plotted against the reduced diameter d/λ, with λ the vacuum operation wavelength. The three horizontal axis are in log scale. Top panel : Effective surface S_{eff} of HE_{11} normalized to $(\lambda/n)^2$ (see main text for the definition). Note the vertical log scale. Middle panel : Group index n_g and effective index n_{eff} (vertical linear scale). Bottom panel : Normalized emission rate into HE_{11}, Γ_M/Γ_0, calculated for a linear, transverse optical dipole located on the wire axis. The vertical scale is linear. The shaded area indicates the multimode regime for an on-axis emitter. For off-axis emitters, the multimode regime appears for smaller diameters (dashed line).

2.1.2 Dielectric screening and coupling to radiation modes

Figure 2.3 shows the relevant normalized SE rates for an on-axis emitter with a transverse optical dipole, which is located on the axis of a photonic wire. The figure reproduces the normalized SE rate into HE_{11} that has been already discussed in the previous paragraph. It also illustrates the coupling to EH_{11}, which is guided in the wire for $d/\lambda > 0.364$. Finally, it shows γ/Γ_0, the normalized SE rate into the 3D continuum of non-guided modes (radiation modes). For $d/\lambda < 0.3$, γ is much smaller than Γ_0, with γ/Γ_0 below 0.1. Such a striking inhibition of SE results from a pronounced dielectric screening effect. To get a simple insight on the phenomenon, we first consider a wire with a vanishingly small diameter, which can be described within the electrostatic approximation.

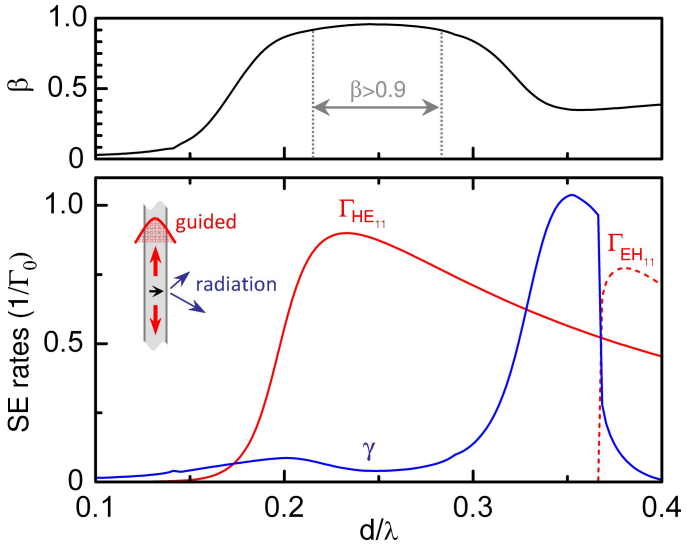

FIGURE 2.3 – **SE dynamics in a photonic wire.** We still consider an infinitely-long wire having a circular section. On its axis, the wire embeds a transverse optical dipole with a vacuum wavelength $\lambda = 950$ nm. The bottom panel presents the relevant spontaneous emission rates (normalized to Γ_0) as a function of the wire reduced diameter d/λ. The top panel shows the calculated β-factor plotted against d/λ — adapted from Ref. [22].

Dielectric screening in the electrostatic approximation. When $d \ll \lambda/n$, wave propagation inside the wire can be neglected, making it possible to solve the problem analytically. The physical mechanism underlying dielectric screening is illustrated in Fig. 2.4(a) for an incident electric field $\mathbf{E}_{\text{inc}}$ oriented perpendicularly to the wire axis. $\mathbf{E}_{\text{inc}}$ generates an homogeneous polarization in the material, which in turn results in the appearance of positive and negative charges at the wire surface. Inside the wire, the surface charges generate a depolarization field $\mathbf{E}_{\text{dep}}$ opposite to $\mathbf{E}_{\text{inc}}$:

$$\mathbf{E}_{\text{dep}} = -\frac{(\frac{n}{n_c})^2 - 1}{(\frac{n}{n_c})^2 - 1 + p}\mathbf{E}_{\text{inc}}, \tag{2.3}$$

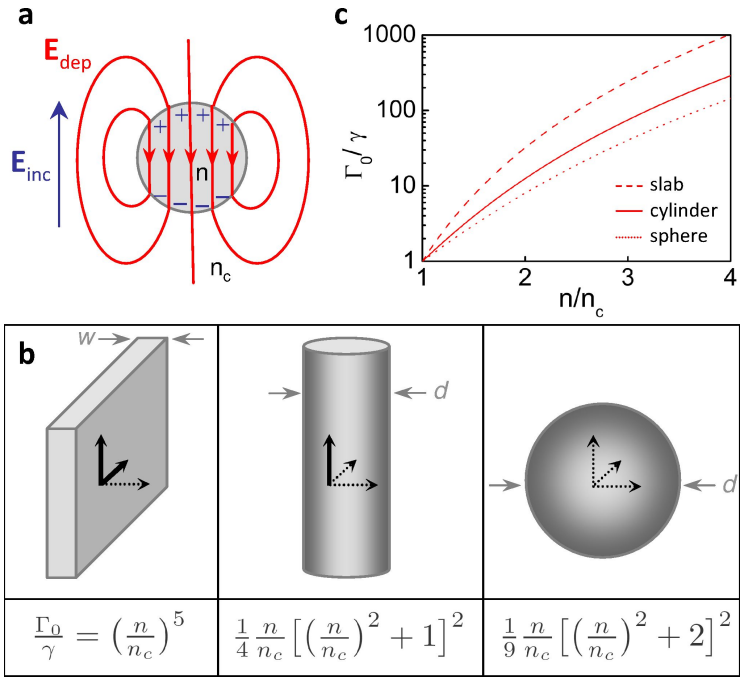

FIGURE 2.4 – **Dielectric screening in the electrostatic approximation.** (a) Sketch illustrating the physics of dielectric screening in a cylindrical wire. The shaded disk represents the wire section. (b) Dielectric screening in an infinite slab, an infinitely-long cylinder and a sphere. Electrical dipoles polarized along "small" dimension(s) of the structure are screened (dotted arrows) and the associated inhibition factor Γ_0/γ is given. Dipoles oriented along "large" dimensions (solid arrows) do not experience screening. The electrostatic approximation is valid for $w, d \ll \lambda/n$. (c) Γ_0/γ versus n/n_c for screened dipole(s) in these three geometries — reproduced from Ref. [22].

where p is an integer which depends on the considered geometry and is equal to 2 in the cylinder case. For $(n/n_c)^2 \gg 1$, $\mathbf{E}_{\text{dep}}$ approaches $-\mathbf{E}_{\text{inc}}$ and the total field $\mathbf{E}_{\text{inc}} + \mathbf{E}_{\text{dep}}$ is strongly reduced. Following Ref. [114], we deduce from reciprocity arguments that, inside the wire, the zero point fluctuations of non-guided modes are damped, leading to a reduced SE rate :

$$\frac{\gamma}{\Gamma_0} = \frac{p^2}{\frac{n}{n_c}\left[(\frac{n}{n_c})^2 - 1 + p\right]^2}. \tag{2.4}$$

This result, valid in the electrostatic limit, holds for any transverse dipole orientation and for any dipole location (even off-axis). With a similar reasoning, one finds that dielectric screening is however absent for a longitudinal dipole, for which $\gamma/\Gamma_0 = n_c/n$ [67]. Interestingly, dielectric screening is a general phenomenon that also occurs in other geometries, including thin infinite slabs or tiny spheres. As schematized in Fig. 2.4(b), screening occurs for dotted dipoles oriented along small dimension(s) of the structure and is absent for solid dipoles parallel to large or infinite dimensions. For a dipole experiencing the screening effect, Eqs. 2.3 and 2.4 are still valid using $p = 1$ for a slab [48] and $p = 3$ for a sphere [114].

The refractive index contrast considerably influences the magnitude of dielectric screening and thus the related SE inhibition. This property is illustrated by Fig. 2.4(c), which shows the inhibition factor Γ_0/γ as a function of n/n_c in a slab, a cylinder and a sphere. For large index contrasts, Γ_0/γ follows a $p^{-2}(n/n_c)^5$ scaling law, leading to drastic effects. As an example, for a tiny GaAs wire immersed in vacuum, Γ_0/γ reaches the remarkable value of 144.

Wires with a finite diameter. Cylinders with a larger diameter ($d \sim \lambda/n$), which support a well confined fundamental mode, require a numerical treatment. Compared to the simple situation described in the last paragraph, three major differences arise. First, emitters with different locations in the wire section will experience different couplings to radiation modes. Second, the magnitude of the screening is globally decreased. Nevertheless, the effect is still strong enough to ensure $\gamma/\Gamma_0 < 0.1$ for $d/\lambda < 0.3$ for an on-axis emitter (see bottom panel in Fig. 2.3). Finally, the screening becomes highly anisotropic. As seen in Fig. 2.6, a dipole with a radial orientation always experiences a significant screening. By contrast, a tangential dipole located close to the wire sidewalls experiences a relatively large coupling to the continuum of radiation modes.

2.2 β-factor of an embedded quantum dot

Integrating a self-assembled QD inside a wire is interesting for at least two reasons : i) to realize bright sources of quantum light, as shown in the next chapter and ii) a QD is a point-like nanostructure that can be used as a local probe of the electromagnetic environment defined by the wire. We first review in this section basic optical properties of self-assembled InAs QDs. Our main goal is to precise the optical dipole associated with elementary excitations in the dot. Next, we exploit the results of section 2.1 to discuss the SE of a QD embedded in a photonic wire.

2.2.1 Basic optical properties of self-assembled InAs/GaAs QDs

Since our samples are not intentionally doped, we will focus on a neutral QD (without resident electron nor hole) ; the case of a singly charged QD will be discussed in the end of the section. For a comprehensive and pedagogical discussion of the aspects that are briefly summarized below, the interested reader may refer to the HDR manuscript of G. Cassabois (in French) [16].

Morphology of a self-assembled InAs/GaAs QD. The formation of self-assembled QDs is a spontaneous process driven by elastic strain. We discuss here the InAs/GaAs system, for which the lattice parameter of InAs exceeds the one of GaAs by 7 %. In the early stage of the growth of InAs on top of a planar GaAs single crystal, one defines a coherent planar InAs layer on GaAs. As the InAs thickness increases, this layer accumulates a large compressive stress. As a result, above a critical thickness of 1.7 InAs monolayer,

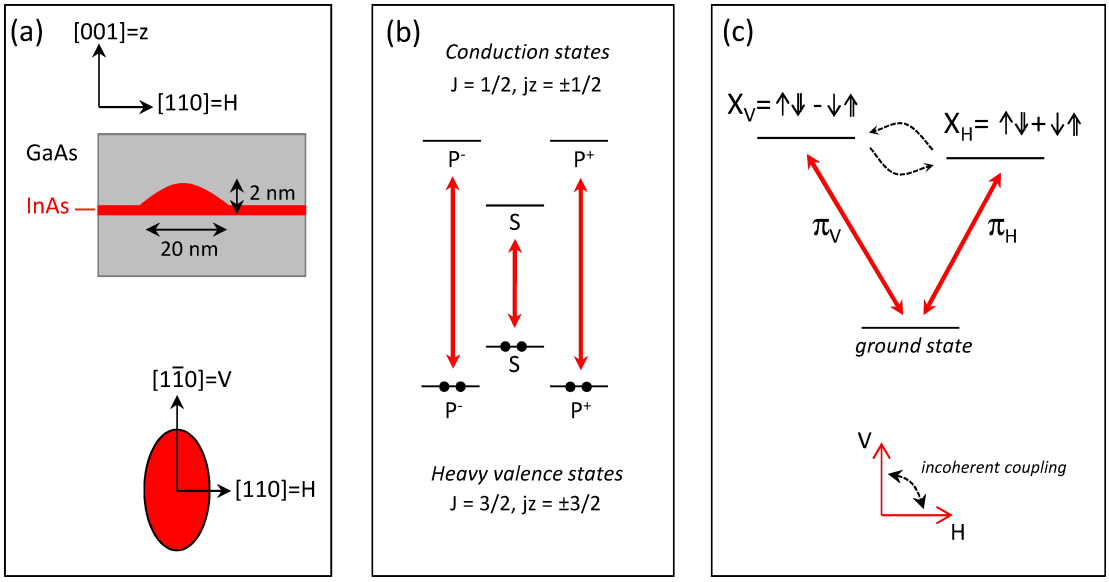

FIGURE 2.5 – **Self-assembled InAs/GaAs QDs.** (a) Typical morphology of a self-assembled QD. Usually, these dots deviate from a perfect cylindrical symmetry and can exhibit a slight elongation along one crystal direction. (b) Ground state of a neutral QD, in the electron picture. The center of the valence band involves heavy states ($J = \frac{3}{2}$, $j_z = \pm\frac{3}{2}$). The red arrows represent allowed interband transitions between envelope states. (c) Bright excitons in a neutral QD, in the electron-hole pair picture (the dark excitons are not shown). In general, the shape anisotropy leads to a fine structure splitting between the two bright states, which feature linear optical dipoles aligned along the crystalline axis.

the planar layer undergoes a structural transition. Stress is then locally relaxed through the spontaneous formation of coherent 3D islands, which grow by partially depleting the neighboring InAs layer. In order to obtain optically active structures, these islands are generally caped with a top GaAs layer. Further morphological changes occur during this step : the shape of the island is modified, and the intermixing of gallium and indium atoms modifies the internal composition of the dot. A typical structure obtained with this fabrication route is schematized in Fig. 2.5(a). The dot is a flat, lens shaped structure that lies on an ultrathin (and rough) InAs quantum well : the wetting layer. Inside the dot, the 3D confinement of charge carriers leads to discrete energy levels, for both the valence and conduction bands. This constitutes a fundamental feature of these structures, often called "artificial atoms". In a first approach, the wetting layer may be considered as a 2D continuum with a smooth cutoff, associated with the film roughness. Above the bandgap energy, the GaAs barrier provides a 3D continuum of electronic states.

Construction of single particle states. In a semiconductor QD, the confined electronic states can be described in the frame of the envelope function formalism. Each electronic wave function is then decomposed as the product of two factors. The first one describes

"short" scale variations, associated with the periodic crystal potential ; this factor is equal to the so-called atomic function of the Bloch state of the bulk materials. The second one, the envelope function, accounts for spatial variations on "large" scales, associated with carrier confinement in the nanostructure.

Since InAs and GaAs are direct band gap semiconductors, optical interband transitions involve states close to the center of Brillouin zone. To precise the nature of those states, we introduce the electron orbital and spin angular momentum $\mathbf{L}$ and $\boldsymbol{\sigma}$; the eigenvalues of $\mathbf{L}^2$ take the form $\hbar^2 L(L+1)$. For the zinc blend crystals under consideration, the center of the conduction band involves $L = 0$ states and features a two-fold spin degeneracy. The valence states are constructed with $L = 1$ states, yielding a 3×2 degeneracy. A strong spin-orbit interaction lifts the degeneracy of the valence sextuplet, while leaving the energy of the conduction states unchanged. To take into account spin-orbit interaction, one conveniently introduces the total angular momentum $\mathbf{J} = \mathbf{L} + \boldsymbol{\sigma}$ and note $\hbar^2 J(J+1)$ the eigenvalues of $\mathbf{J}^2$. The quadruplet of valence states with $J = \frac{3}{2}$ do not experience any energy shift, while the $J = \frac{1}{2}$ doublet is shifted towards energies low enough so that it can be neglected. Furthermore, shape and strain-field asymmetries lift the degeneracy of the $J = \frac{3}{2}$ valence quadruplet. Indeed, we have seen that a self-assembled QD features a flat lens morphology, leading to an anisotropic spatial confinement. In addition, a residual in-plane compressive strain is present in the dot. In first approximation, these effects feature a cylindrical symmetry, whose axis coincides with the growth direction. This direction is chosen as the quantization (z) axis and we note $\hbar j_z$ the eigenvalues of J_z, the projected total angular momentum. In the $\{|J, j_z\rangle\}$ basis, the fundamental valence state is a heavy state doublet ($J = \frac{3}{2}$, $j_z = \pm\frac{3}{2}$), while the light state doublet ($J = \frac{3}{2}$, $j_z = \pm\frac{1}{2}$) is rejected at energies low enough so that it can be safely neglected.

The envelope states feature a cylindrical symmetry, reminiscent of the dot (idealized) shape. They are indexed by the eigenvalue m of the projected orbital momentum L_z. The fundamental envelope state corresponds to $m = 0$ and features no degeneracy ; by analogy with atomic physics it is denoted S. The first excited shell features a two-fold degeneracy : it is composed of the envelope states P^+ and P^- which correspond to $m = +1$ and $m = -1$, respectively. Figure 2.5(b) illustrates the ground state of a neutral quantum dot in the electronic picture adopted so far.

Optically active interband excitations. We now consider an elementary interband excitation, obtained by promoting a confined electron from the valence S shell to the conduction S shell. We adopt the electron — hole picture, in which a full valence band with a missing electron is represented by a hole, whose physical properties are opposite to the one of the missing electron. Depending on the projection of the electron spin ($\uparrow$ or $\downarrow$) and the one of the hole pseudo-spin ($\Uparrow \leftrightarrow j_z = +\frac{3}{2}$ or $\Downarrow \leftrightarrow j_z = -\frac{3}{2}$), four excitonic [(1)] states are possible : $|\uparrow\Downarrow\rangle$, $|\downarrow\Uparrow\rangle$, $|\uparrow\Uparrow\rangle$ and $|\downarrow\Downarrow\rangle$. Out of these, only $|\uparrow\Downarrow\rangle$ and $|\downarrow\Uparrow\rangle$ are optically

(1). Though corresponding to common usage, using the term "exciton" to designate an electron-hole pair trapped in a self-assembled QD may be misleading. An exciton usually refers to an electron-hole pair bound by Coulomb interaction. A self-assembled QD features lateral dimension that are smaller than the exciton Bohr radius : the Coulomb interaction is thus smaller than the electron and hole confinement energies. In

active : they are called bright excitons. They correspond to an electron—hole pair total projected angular moment $j_z^{eh} = \pm 1$. In contrast, $|\uparrow\Uparrow\rangle$ and $|\downarrow\Downarrow\rangle$, which are characterized by $j_z^{eh} = +2$ and -2, are dark excitons.

In fact, the ensemble of excitonic states exhibits a fine structure associated with electron-hole exchange interactions. Those split the bright and dark excitons and reject the dark states towards low energies by a few hundreds of μeV. Moreover, a real QD generally deviates from a perfect cylindrical symmetry and is often elongated along one direction (the $[1\bar{1}0]$ direction in Fig. 2.5(a)). As shown in Fig. 2.5(c), this reduction of symmetry splits the bright excitonic doublet in two states $X_V = |\uparrow\Downarrow\rangle - |\downarrow\Uparrow\rangle$ and $X_H = |\uparrow\Downarrow\rangle + |\downarrow\Uparrow\rangle$ (the normalization factor is omitted for simplicity). They are no more eigenstates of J_z^{eh} and their recombination is associated with the emission of linearly polarized photons, along the V and H directions, respectively. The energy separation between X_V and X_H is the fine structure splitting S ; we will in the last chapter that this quantity plays a critical role for the emission of entangled photon pairs by a QD. For a typical as-grown QD, S generally amounts to a few tens of μeV.

How to model the optical dipole of an exciton trapped in a QD ? In a neutral QD, each bright exciton corresponds to a linear optical dipole oriented along a QD eigenaxis, perpendicular to the growth axis. If such a dot is immersed in an anisotropic photonic environment, each of these excitons will recombine independently at its own rate. This is for example exploited in Ref. [108] to reveal the anisotropic nature of a photonic crystal membrane. However, the dots studied in this manuscript behave differently. Even when they are located in a strongly anisotropic photonic environment (for example an elliptical wire), a mono-exponential decay is observed in time-resolved PL experiments. We attribute this feature to a spin-flip between the bright states that takes place on a time scale faster than the radiative decay. Such an *incoherent* coupling, mediated by some degree of freedom of the environment, could be either a direct process (double electron and hole spin-flip), or a two step process, *via* the dark states. In the following, we compute the dot decay rate as the arithmetic average of the rate of each dipole. We note that such a model also reproduce the decay of singly charged excitons, that can be described as two *coherently* coupled linear optical dipoles.

2.2.2 Coupling to the HE_{11} mode family for an embedded QD

As seen in the previous paragraph, a self-assembled QD features optical dipole components perpendicular to the growth axis, which coincides here with the wire axis. In the following, the QD is modeled as two coupled, orthogonal linear optical dipoles with identical oscillator strengths and perfect radiative yields. The QD luminescence then decays with a single rate, which is the arithmetic mean of the individual dipole SE rates. We are

this strong confinement regime, the energy of the trapped electron-hole pair is weakly renormalized by the Coulomb terms.

interested in the fraction β of SE coupled to the whole HE_{11} mode family. It comprises two modes which share the same dispersion law and feature orthogonal linear polarizations.

On-axis emitter. By symmetry, when the QD is located on the wire axis, β is identical to the one of a single linear optical dipole :

$$\beta = \frac{\Gamma_M}{\Gamma_M + \Gamma_g + \gamma}. \tag{2.5}$$

Here Γ_M, Γ_g and γ are the SE rate of a linear dipole into HE_{11}, possibly other guided modes and radiation modes, respectively. Figure 2.3 shows that β reaches a maximum value of 0.95 for $d/\lambda = 0.24$, the signature of an almost perfect single-mode emission. This result is achieved thanks to a good coupling to the fundamental guided mode ($\Gamma_M \sim \Gamma_0$), combined with a pronounced inhibition of the coupling to radiation modes. In addition, $\beta > 0.90$ is maintained for d/λ in the $0.21 - 0.28$ range. Such a large interval relaxes fabrication constraints and is also the hallmark of a very broad operation bandwidth $\Delta\lambda/\lambda = 0.26$ (this result is confirmed when the refractive index dispersion of GaAs is taken into account).

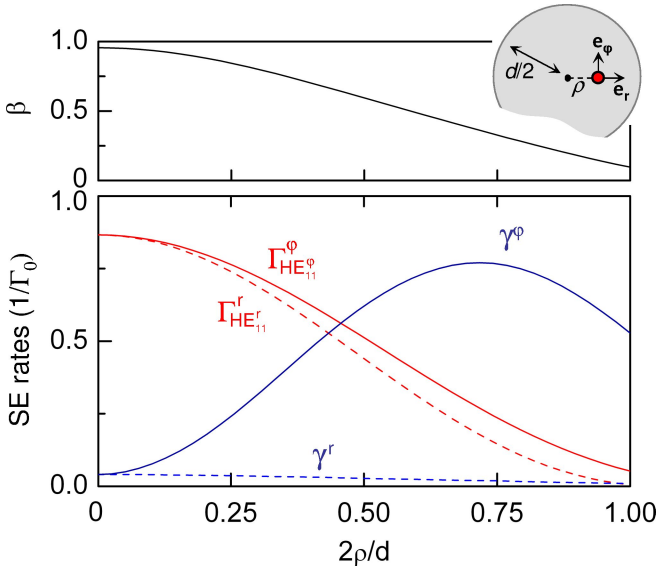

FIGURE 2.6 – **SE dynamics for an off-axis emitter.** The calculations are conducted for an infinite wire with $d/\lambda = 0.23$. Bottom panel : relevant SE rates (normalized to Γ_0) versus the reduced emitter-axis distance $2\rho/d$, for a radial (r) and an azimuthal (φ) optical dipole. For each orientation, the dipole couples similarly to one of the two polarization-degenerate HE_{11} modes (linear polarization basis spanned by $\mathbf{e}_r$ and $\mathbf{e}_\varphi$). In contrast, the coupling to the radiation modes is strongly affected by the dipole orientation. Top panel : β-factor as a function of $2\rho/d$, calculated for an isotropic, in-plane emitter (see text for details) — reproduced from Ref. [22].

Off-axis emitter. Off-axis emitters break the problem symmetry, making it necessary to separate the contributions of dipoles oriented along radial and azimuthal directions. These are respectively spanned by $\mathbf{e}_r$ and $\mathbf{e}_\varphi$, as shown as an inset in Fig. 2.6. In this linear polarization basis, the HE_{11} mode family consists of two modes M^r and M^φ, with an in-plane dominant polarization oriented along $\mathbf{e}_r$ and $\mathbf{e}_\varphi$. For an in-plane, isotropic emitter, the fraction β of SE coupled to the HE_{11} mode family can still be calculated with Eq. 2.5, using the average rates $\Gamma_M = \frac{1}{2}(\Gamma^r_{M^r} + \Gamma^\varphi_{M^\varphi})$, $\Gamma_g = \frac{1}{2}(\Gamma^r_g + \Gamma^\varphi_g)$ and $\gamma = \frac{1}{2}(\gamma^r + \gamma^\varphi)$. Here, the SE rates indexed by the superscripts r and φ correspond to linear dipoles of radial and azimuthal orientation, respectively. As seen in Fig. 2.6, β decreases with the emitter-axis distance ρ. This is due to the reduced coupling to the HE_{11} modes and to the pronounced increase in γ^φ. For $d/\lambda > 0.23$, the presence of higher order guided modes degrades β for off-axis emitters (not shwon).

Enhancing the β-factor with a bottom mirror. As detailed later in chapter 3, a mirror located below the wire can further accelerate the SE into HE_{11}. Such a mirror is designed to reflect the HE_{11} photons propagating downward back into the wire, in the upward HE_{11} mode. For a gold-silica mirror, the amplitude modal reflectivity $|r_b|$ reaches 0.95, giving birth to a pronounced standing wave pattern between the emitter and the mirror. Positioning the emitter on an electrical field antinode accelerates the SE rate into the upward HE_{11} mode by a factor $1 + |r_b| \approx 2$ (Ref. [31]). This of course improves β, especially for off-axis emitters. One randomly located QD out of 15 then experiences $\beta > 0.9$ and one QD out 5 experiences $\beta > 0.8$. When considering the coupling to a single mode, the spatial and spectral randomness inherent to self-assembled InAs QDs does not compromise the device fabrication yield. From a practical point of view, photonic wires may appear more convenient than microcavity-based structures which require deterministic fabrication methods to achieve a reasonable fabrication yield [8, 24]. There is however a price to pay : the SE rate enhancement in a photonic wire is quite modest, which can be a limitation for some advanced applications. Indeed, a moderate acceleration of SE (by typically a factor of $4-5$) is generally desirable to realize sources of indistinguishable single photons or a entangled photon pairs with QDs. We propose in chapter 4 a possible strategy to implement such an acceleration, while preserving a reasonable operation bandwidth.

2.3 Spontaneous emission dynamics : experiments

Reference [11] investigates experimentally the SE dynamics of single InAs QDs embedded in GaAs wires. These wires were obtained by etching a planar GaAs sample containing a single layer of self-assembled InAs QDs. In fact, we report here results obtained on complete wire antennas : the wires are supported by a bottom planar mirror and feature a top "needle-like" taper. More details on the design and fabrication of such antennas will be provided in the next chapter; a SEM picture of a representative wire can found in Fig. 3.4(c). The optical measurements were conducted at cryogenic temperature (5 K) in a time-resolved micro-photoluminescence setup. The results reported below were obtained

on single excitonic lines, with a low excitation power, far below the saturation of the excitonic transition. The clean-room processes to obtain such structures have been developed by Nitin Singh Malik (PhD student under my supervision at the time) and myself. The experiments were performed by Megan Creasey (visiting PhD student) and Joël Bleuse.

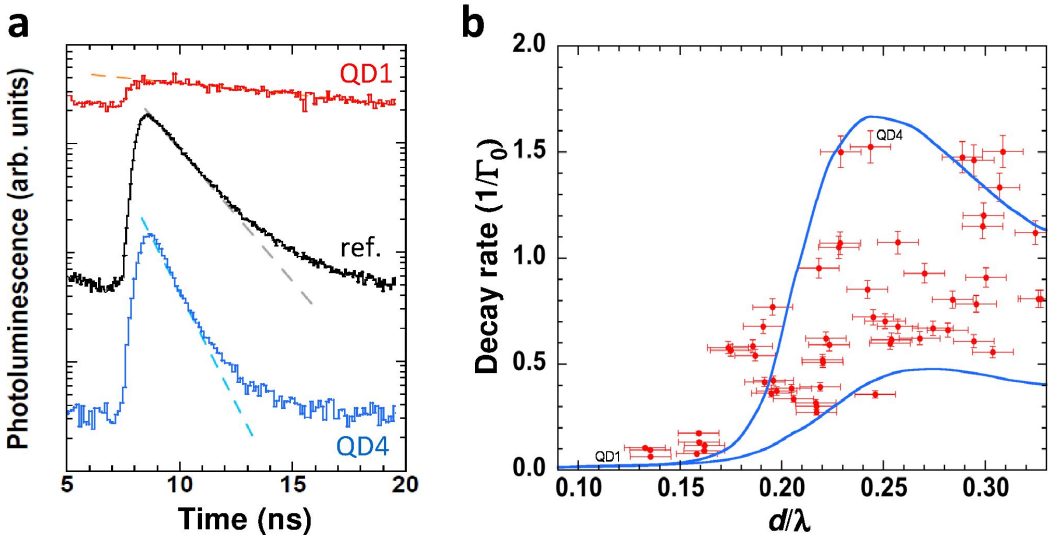

FIGURE 2.7 – **Inhibition and enhancement of SE in a photonic wire.** The measurements have been done on tapered wires lying on a bottom planar mirror, shown in Fig 3.4(c). (a) Time traces of the photoluminescence decays of the excitonic line associated with a single QD embedded in "small" and "large" wires ($d/\lambda = 0.13$ and 0.25 for QD1 and QD4, respectively). The reference curve (ref.) has been measured on the sample before etching. (b) Compilation of the measured decay rates of 60 single QDs in photonic nanowires with various diameters. The data are bounded by the calculated maximum and minimum total SE rates (solid lines), which are obtained by varying the lateral position of the emitter in the wire — adapted from Ref. [11].

Inhibition and enhancement of spontaneous emission. The coupling to radiation modes can be investigated in "thin" wires, for which γ dominates the total SE rate. As shown in Fig. 2.3, this regime is achieved for $d/\lambda < 0.17$ in an infinitely-long wire. For a fabricated wire with $d/\lambda = 0.13$, the luminescence decay rate Γ of an embedded QD can be as low as $0.045\,\mathrm{ns}^{-1}$, far below the reference decay rate $\Gamma_0 = 0.71\,\mathrm{ns}^{-1}$ of similar QDs embedded in bulk GaAs (Fig. 2.7(a)). Generally speaking, achieving an inhibition factor $\Gamma_0/\Gamma = 16$ is remarkable, because this requires a demanding control over a 3D continuum of optical modes. Moreover, this result is achieved here with a very simple structure (a dielectric cylinder), whereas large inhibition factors are usually obtained with much more complex structures, such as 2D or 3D photonic crystals [77, 107, 59] or photonic Tamm structures [35]. In a larger wire, with $d/\lambda = 0.25$, one can investigate the coupling to HE_{11}. The fastest excitonic line then exhibits an emission rate $\Gamma = 1.1\,\mathrm{ns}^{-1}$, corresponding to a SE

enhancement factor $\Gamma/\Gamma_0 = 1.55$, close to the maximal value predicted for a wire featuring a bottom mirror ($\Gamma/\Gamma_0 = 1.7$). When combined, these results confirm the potential of photonic wires to achieve an efficient spontaneous emission control.

To further verify the agreement with theory, we have conducted a systematic survey of the emission rate of 60 QDs embedded in wires with various diameters, with d/λ in the $0.13 - 0.33$ range. The experimental results are shown as dots in Fig. 2.7(b), together with the calculated maximum and minimum normalized emission rate, shown as solid curves. Again, this calculation was conducted assuming an isotropic, in-plane emitter. Two regimes can be distinguished on this plot. Below $d/\lambda \approx 0.16$, SE is strongly inhibited and SE rates are quite uniform : Γ/Γ_0 is dominated by γ which is relatively independent of the QD location in the wire section ; QD1 belong to this limit. Above $d/\lambda \approx 0.16$, Γ/Γ_0 increases and shows stronger variations associated to the spatial variations of $\Gamma_{\rm M}$ and γ. The global agreement between theory and experiments demonstrates a rather good understanding of SE dynamics in photonic nanowires. Still, one can notice that some experimental points are above the calculated decay rate, especially in the inhibited part of the plot. This is likely due to non-radiative processes that are discussed in the next paragraph.

Estimation of the QD radiative yield. Modulating the local photonic density of states seen by an emitter is a powerful strategy for determining its radiative yield $\eta_{\rm rad}$, a quantity that is usually difficult to measure. Such a method has been used on colloidal quantum dots covered — or not — by a liquid droplet [14], and more recently on ensembles of self-assembled InAs QDs located at various distances from a semiconductor-air interface [51]. Here, we illustrate and apply this method by comparing two situations : (1) single QD embedded in a "small" wire and (2) ensemble of QDs immersed in bulk GaAs (as-grown sample). The decay rate extracted from a time-resolved PL experiment is the sum of two contributions : a radiative (=SE) decay rate and a non-radiative one. For the two situations described above, the PL decay rates can be expressed as $\Gamma_{\rm PL}^{\rm nw} = \Gamma_{\rm rad}^{\rm nw} + \Gamma_{\rm nr}^{\rm nw}$ and $\Gamma_{\rm PL}^{\rm bulk} = \Gamma_{\rm rad}^{\rm bulk} + \Gamma_{\rm nr}^{\rm bulk}$. The subscripts "rad" and "nr" stand for radiative and non-radiative, respectively. Assuming that the non-radiative channel is not affected by the modification of the environment ($\Gamma_{\rm nr}^{\rm bulk} = \Gamma_{\rm nr}^{\rm nw} = \Gamma_{\rm nr}$), one obtains :

$$\Gamma_{\rm nr} = \frac{\Gamma_{\rm PL}^{\rm nw} - \left(\frac{\Gamma_{\rm rad}^{\rm nw}}{\Gamma_{\rm rad}^{\rm bulk}}\right)\Gamma_{\rm PL}^{\rm bulk}}{1 - \left(\frac{\Gamma_{\rm rad}^{\rm nw}}{\Gamma_{\rm rad}^{\rm bulk}}\right)}. \tag{2.6}$$

Since the considered environments are simple enough to be described theoretically in a faithful way, the ratio $\Gamma_{\rm rad}^{\rm nw}/\Gamma_{\rm rad}^{\rm bulk}$, which is independent of the emitter, can be calculated. The radiative yield $\eta_{\rm rad} = (\Gamma_{\rm PL} - \Gamma_{\rm nr})/\Gamma_{\rm PL}$ is then immediately deduced. In a wire with $d/\lambda = 0.13$, a calculation of the local density of optical states yields $\Gamma_{\rm rad}^{\rm nw}/\Gamma_{\rm rad}^{\rm bulk} = 1/32$. Using the experimental values $\Gamma_{\rm PL}^{\rm nw} = 45\,\mu{\rm s}^{-1}$ and $\Gamma_{\rm PL}^{\rm bulk} = 0.71\,{\rm ns}^{-1}$, one obtains the bulk radiative yield $\eta_{\rm rad}^{\rm bulk} = 0.97$. Importantly, the relatively low non-radiative rate obtained in this "small" wire implies that in wires with a larger diameter (~ 200 nm), for which the radiative rate is close to $\Gamma_{\rm rad}^{\rm bulk}$, the radiative yield will be also very close to one. In fact, this

result is consistent with the thorough study conducted in Ref. [51] : considering a typical bulk SE rate, the non-radiative processes start to compete with the radiative one for an emitter-interface distance typically below 50 nm.

A few remarks on bottom-up wires. A QD integrated in a wire can also be elegantly obtained by a direct growth approach [97, 100, 46]. In such a bottom-up structure, the QD is defined as a longitudinal heterostructure in a wire which is thin enough to ensure a good electronic confinement. It is generally profitable to realize a lateral over-growth, in order to limit or suppress the detrimental influence of the surface states on the dot optical properties. Recently, a pronounced SE inhibition (by a factor of 12) was observed in thin bottom-up InP wires containing a single InAsP QD [15]. This result shows the interest of the direct-growth approach to obtain QD with a large radiative yield, and with optical dipole compatible with an optimal spontaneous emission control. This approach also leads to wires embedding exactly a single QD, located precisely on the wire axis. We will see in the next chapter that efficient optical antennas have also been realized by direct growth.

However, SE inhibition is not systematically observed in thin bottom-up wires. As an example, a very short lifetime (500 ps at cryogenic temperature) was observed for a CdSe QD integrated in a ZnSe wire [100]. At this stage, several reasons could explain this result. First, let us notice that the relative stability of the lifetime in the $5 - 100$ K temperature range tends to exclude a non-radiative decay channel. A first explanation could be that the fundamental optical transition is not built with pure heavy holes states. Indeed, a valence band mixing could lead to a dipole component aligned with the wire axis, a direction for which the radiative yield is Γ_0/n_c. Alternatively, the experiments were conducted with wires lying on a substrate : it is possible that this high index half space modifies significantly the electromagnetic environment and thus suppresses the inhibition effect. Further experiments, preferentially on vertically standing nanowires, will be necessary to elucidate this point.

2.4 Controlling the polarization with elliptical wires

Some applications (high-β microlasers, emission of indistinguishable photons) require a control over the polarization of the emitted photons. In a circular wire, a "true" single-mode emission can only be achieved using a highly polarized emitter, which is not the case for usual semiconductor emitters. Reference [73] demonstrates how this limitation can be overcome with photonic wires featuring a moderately anisotropic section.

Specifically, we consider a wire with an elliptical section of major diameter $d_\parallel = \lambda/n$ and minor diameter $d_\perp = d_\parallel/2$. Such a structure supports only two non-degenerate guided modes : $M_\parallel$ and $M_\perp$, with an in-plane polarization respectively oriented along the major and minor axis of the wire section. Figure 2.8(a) shows that $M_\perp$ is completely deconfined outside the wire while $M_\parallel$ remains tightly confined. In this high index structure, the interplay of the field boundary condition and a moderate shape anisotropy leads to a very large optical anisotropy. On the wire axis, the calculated intensity of the zero point fluc-

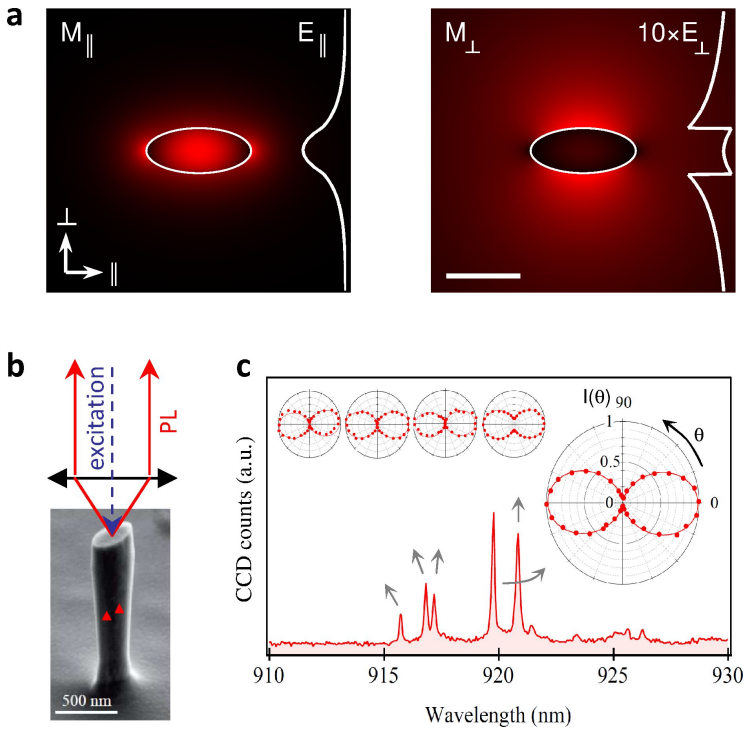

FIGURE 2.8 – **Polarization control in an elliptical wire.** (a) Selective deconfinement of the guided mode $M_\perp$ in an elliptical wire ($d_\parallel = \lambda/n, d_\perp = d_\parallel/2$). The two color plots picture $E_\parallel$ and $E_\perp$, the dominant in-plane electric field components associated with the modes $M_\parallel$ and $M_\perp$, respectively. For clarity, $E_\perp$ has been multiplied by 10. The linear plot on the right of the panels shows the evolution of $E_\parallel$ and $10\times E_\perp$ for a cut along the ellipse short axis. The scale bar represents 200 nm. (b) Experimental configuration and SEM micrograph of a GaAs wire with an elliptical section. (c) Micro-photoluminescence spectrum recorded on a single wire at 5 K. The polarization analysis associated with five isolated spectral lines is shown in the insets — adapted from Ref. [73].

tuations associated with $M_\parallel$ is typically 100 time larger than the one associated with $M_\perp$. Since dielectric screening is still very efficient in these structures, an emitter with in-plane dipole components embedded inside the wire experiences a single-mode electromagnetic environment. In an infinitely-long wire, the theoretical fraction of SE coupled to $M_\parallel$ reaches $\beta_\parallel = 0.92$. Similarly than for the cylinder case, $\beta_\parallel$ could be further improved by inserting a mirror below the wire.

Polarization control has been demonstrated experimentally on GaAs wires having an elliptical section. To this end, we have developed a specific fabrication process : it was indeed very important to precisely control the geometry of the wire section. We employ here a 100 nm thick nickel hard mask, whose geometry is faithfully transferred to GaAs during the anisotropic etching of the wire. In the wire shown in Fig. 2.8(b), the major and minor section diameters in the QD plane are 280 nm and 130 nm, respectively. The optical measurements were conducted by Mathieu Munsch, during his postdoc in the team. A

typical μPL spectrum, recorded under pulsed optical excitation, is shown in Fig. 2.8(c). It features 5 sharp lines, associated with excitonic complexes trapped in 2 distinct QDs. The insets show the polarization analysis of each lines. The 5 line emissions exhibit very similar linear polarizations oriented along the major axis of the wire section. The polarization ratio $I_{\parallel}/(I_{\parallel}+I_{\perp})$ reaches the remarkable value of 0.95, proving that SE control in photonic wires can be extended to the polarization degree of freedom.

Summary

To conclude this chapter, SE control in a fiber-like photonic wire relies on the efficient lateral confinement of the fundamental guided mode combined with a dielectric screening effect that suppresses to a large extent the emission into the continuum of non-guided modes. Dielectric screening is very efficient for optical dipoles perpendicular to the wire axis, but is absent for a longitudinal dipole. To achieve optimal performance, it is thus important to choose an emitter with transverse optical dipole components, such as a self-assembled QD. For an on-axis emitter located on the axis of an infinitely-long wire, β reaches 0.95. Moreover, this 1D photonic system offers a very broad operation bandwidth ($\beta > 0.9$ over a 250nm spectral range around 950nm). The β-factor can be further improved — especially for off-axis emitters — by inserting a mirror below the wire. In that case, one randomly located QD out of 15 experiences $\beta > 0.9$ and one QD out 5 experiences $\beta > 0.8$. As far as the β-factor is concerned, the spatial and spectral randomness inherent to self-assembled QDs is not a critical issue. Finally, depending on the targeted application, it is also possible to achieve a linearly polarized emission with a wire featuring a moderately elliptical section.

Chapitre 3

Photonic wire antennas

In this chapter, we show how to realize an optical antenna by tailoring the ends of a photonic wire. The first section presents design guidelines and details the key extra elements of the first generation of wire antennas, namely a planar bottom mirror and a top needle-like taper. Next, section 3.2 describes the first application of this light collection strategy to the field of solid-state quantum optics. By integrating a QD inside such a structure, we have realized a very bright single-photon source using a top-down fabrication process. In section 3.3, we briefly discuss avenues opened by the rapid and recent progress in the direct growth of heterostructure nanowires. Finally, section 3.4 presents a second generation of wire antennas which exploit the opposite tapering strategy, leading to structures that we have nicknamed *photonic trumpets*. In particular, this tapering strategy offers optimal performance for a much broader range of taper angles. Using this approach, we demonstrate a very bright single-photon source that features a Gaussian far-field emission, an important asset for most advanced applications.

3.1 Antenna design

To reach high extraction efficiency, SE control only constitutes a first step that must be completed by a proper engineering of the wire far-field emission. A real wire has of course a finite length, and its far-field emission essentially depends on how light is scattered by the two wire ends. If we consider a vertical wire on a planar substrate, two issues need to be solved. First, half of the photons are emitted downwards : a mirror reflecting them back into the wire, into the upward HE_{11} mode, is required. In the following, $r_b = |r_b|e^{i\phi_b}$ will represent the mirror modal reflectivity (amplitude coefficient associated with HE_{11}). Second, we have seen that an optimal SE control implies a strongly confined HE_{11} mode, on a length scale well below the vacuum wavelength λ. As a consequence, the HE_{11} photons leaving the top facet are strongly scattered to large angles, thus strongly limiting the collection of photons in the far-field [68]. To solve this issue, we borrow a strategy from the guided optics community [3] : a needle-like taper deconfines progressively HE_{11} into the wire background, leading to a directive far-field emission [42]. In addition, the taper

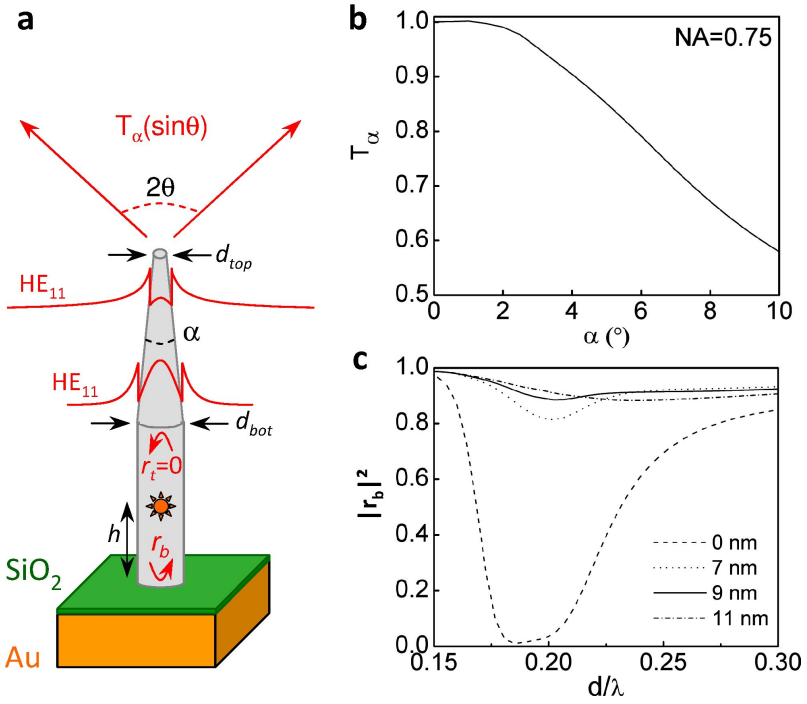

FIGURE 3.1 – **Optimization of the far-field emission.** (a) Photonic wire on a planar gold-silica mirror. The top needle taper ensures a lateral expansion of HE_{11}, leading to a directive far-field emission. (b) Taper transmission into a NA=0.75 collection lens ($T_\alpha(0.75)$) plotted against the tapering angle α. For $\alpha < 10°$, the taper modal reflectivity r_t is negligible. As detailed in Ref. [42], the sharp tip can be truncated without degrading the performance provided that the guided mode is sufficiently deconfined in air. (c) Theoretical modal reflectance of HE_{11} (energy coefficient $|r_b|^2$) of a bare 250 nm thick gold layer (orange curve), and same quantity with a silica spacer, as a function of d/λ. The calculation is repeated for 3 spacer thicknesses (7, 9 and 11 nm) — adapted from Ref. [22].

gradually realizes the transition $n_{\text{eff}} \to n_c$ and thus suppresses the modal reflectivity r_t of the top facet. A complete wire antenna implementing all these elements is schematised in Fig. 3.1(a).

3.1.1 Fabry-Perot model

Our goal is to optimize the collection of the guided photons by a commercial microscope objective located above the wire. To this end, we employ the Fabry-Perot model developed in Ref. [31]. Starting from results obtained for an infinite wire, the model assumes that the reflection of the wire facets only modifies the coupling to the guided mode, but do not influence the coupling to radiation modes. The knowledge of the facet reflectivities and the emitter location is then sufficient to determine the emission rate of the emitter and the collection efficiency of the antenna. In the following, we suppose that $r_t = 0$: our emitter is

thus integrated in a semi-open 1D electromagnetic environment : the bottom mirror reflects the photons emitted downwards back into the wire and the photons propagating upwards freely leave the wire. The emission rate into the guided mode — and thus the extraction efficiency — is maximal when the reflected beam acquires a phase equal to $2\pi m$, with m a strictly positive integer. This condition defines a discrete series of optimal vertical positions h_m for the emitter :

$$\frac{2n_{\text{eff}}h_m}{\lambda} + \frac{\phi_b}{2\pi} = m \tag{3.1}$$

The first term is linked to the optical path in the wire, with n_{eff} the effective index of the guided mode. The second term is the phase acquired after a reflection on the bottom mirror. Low values for m correspond to locations close the mirror. In the 1D geometry under consideration, all the positions h_m lead to the same emission rate into the HE_{11} mode family :

$$\Gamma_M = \Gamma_M^{\infty}(1 + |r_b|), \tag{3.2}$$

with Γ_M^{∞} the emission rate into the HE_{11} modes computed for an infinitly long wire. However, small values for h_m minimize the optical path in the wire and thus lead to a larger operation bandwidth and to a larger diameter tolerance (n_{eff} depends on d). In the following, the emitter will thus be located on the first field antinode above the mirror. Introducing $T_\alpha(\sin\theta)$, the taper transmission into a cone having a numerical aperture $\text{NA} = \sin\theta$, the extraction efficiency reads :

$$\epsilon = \frac{1}{2}\beta^{\infty}\frac{(1 + |r_b|)^2}{1 + \beta^{\infty}|r_b|}T_\alpha(\sin\theta). \tag{3.3}$$

Here, β^{∞} is the SE coupling factor for an infinite wire. Importantly, Eq. 3.3 reduces the optimization of the extraction efficiency to the independent designs of the mirror and top taper. For ideal mirrors and tapers ($|r_b| = 1$ and $T_\alpha(\sin\theta) = 1$) the wire-antenna approach offers an maximum extraction efficiency of $2\beta^{\infty}/(1 + \beta^{\infty}) = 0.98$. In the following, we consider the performance of the top taper and the design of a suitable bottom mirror.

3.1.2 Needle taper

By launching a guided mode into a smoothly tapered section, one expects the mode to adiabatically adapt to slowly varying boundary conditions. In the case of a needle taper, the reduction in the wire diameter progressively deconfines HE_{11} into the wire background and increases the mode lateral dimensions. Needle tapers will be investigated into more details in section 3.4 ; in particular, we will see that for geometrical parameters accessible in a vertical geometry, a needle tapper is usually not perfectly adiabatic. Nevertheless, the relevant figure of merit for light collection is the total transmission T_α into the collection optics. For a NA=0.75 lens, this quantity is plotted in Fig. 3.1(b) as a function of the tapering angle α. The considered tapper features a bottom diameter $d_{\text{bot}}/\lambda = 0.23$, which corresponds to the optimal confinement of HE_{11} and a top diameter $d_{\text{top}}/\lambda = 0.15$. For $\alpha < 2°$, T_α is very close to unity ; for larger angles, the transmission drops below 0.6 for

$\alpha > 10°$. Optimal performances thus require sharp tips, and we will see in the following how they can be obtained from top-down and bottom-up processing routes.

3.1.3 Bottom mirror

The design of the bottom mirror is rather complex, and has been comprehensively discussed in Refs. [30] and [31]. First, one should note that classical approaches relying on Bragg reflection raise many issues for the design and the fabrication. For instance, planar Bragg mirrors made of AlAs and GaAs periods are inefficient, because of their limited angular acceptance. Indeed, light leaving the wire is scattered to large angles, well above the 20° acceptance angle of a planar AlAs/GaAs Bragg mirror. It is possible to reach a satisfying modal reflectivity with a Bragg mirror integrated in the wire [18]. However, for $d \sim \lambda/n$, a significant part of the guided mode energy lies outside the wire. The effective index contrast is thus reduced and achieving a high reflectivity requires a huge number of pairs. Given the small diameter of the structure and the design tolerances, the fabrication of such structures represents a tremendous technological challenge. Bloch-engineered Bragg mirrors, initially introduced for nano-beam cavities [56] and recently demonstrated for sub-micron AlGaAs micropillars [60] may lead to more realistic structures in the future.

A metallic gold layer constitutes an attractive alternative, which offers a large reflectivity over a broad wavelength range. However, Fig. 3.1(c) shows that the modal reflectivity of a gold planar layer drops to nearly zero for the diameters of interest. Though not completely elucidated, this drop is likely caused by a detrimental coupling to surface plasmon modes. Fortunately, a thin dielectric spacer layer ($9 - 11$ nm), inserted between the wire and the metallic layer restores $|r_b|^2 > 0.9$, over the whole range of useful wire diameters. Given its simplicity, broad operation bandwidth and robustness, this approach has been retained for the bottom mirror.

3.2 An ultrabright single-photon source

An on-demand single-photon source is a device that ideally emits a light pulse containing exactly one photon in response to a trigger signal. Semiconductor self-assembled QDs are well established single-photon emitters [36], which can be triggered either with optical [71, 89] or electrical excitation pulses [120]. At cryogenic temperature, they feature a large radiative yield and a fast emission rate, on the nanosecond time scale [51]. However, light extraction from these structures is notoriously difficult, because of the large refractive index of the surrounding semiconductor matrix [9]. This is a critical issue, because for all potential applications (quantum cryptography [39], light flux metrology and linear optics quantum computing [53]), the external efficiency of the source, defined as the probability to collect a photon after a trigger pulse, is a critical figure of merit. In this section, we present a bright single-photon source based on a spectrally-isolated QD inserted in a photonic wire antenna. We successively discuss the device fabrication, optical characterization and performances.

3.2.1 Nanofabrication

The fabrication of these optical antennas has been developed during the PhD of Nitin Singh Malik, basically starting "from scratch". The process flow can be decomposed into four major steps that are presented in Fig. 3.2. The structures were defined within a top-down approach, starting from a planar structure grown by molecular beam epitaxy (step a). Because it is not possible to grow good quality semiconductor on gold, the insertion of the planar Au-SiO_2 mirror necessarily involved a thin film deposition (step b) followed by a delicate flip-chip step (c). The final step (d) in which the tapered wires are defined using dry plasma etching, is also critical.

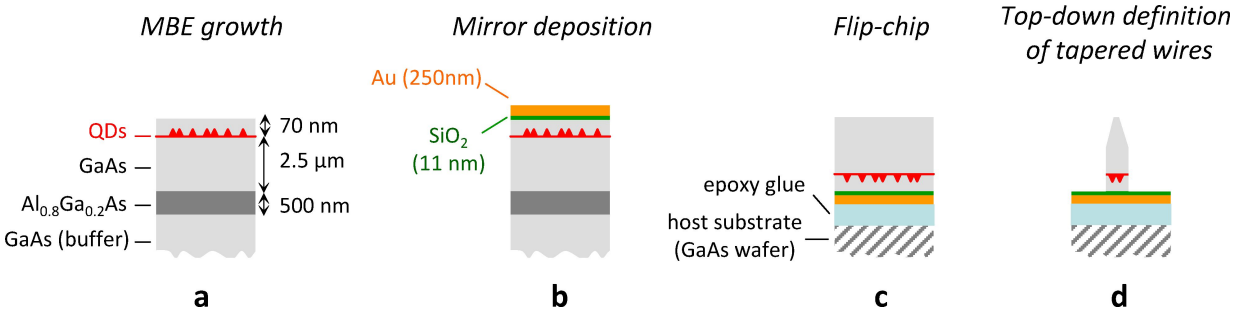

FIGURE 3.2 – **Top-down fabrication of a wire antenna.** The major steps of the process are presented ; the fabrication of a tapered wire is detailed in the next figure.

Molecular Beam Epitaxy (MBE) growth and flip-chip. The planar structure used as a starting point is shown in Fig. 3.2 (a) and was grown by Maela Bazin, during her PhD. It consists of a 2.5 μm thick GaAs layer embedding a single layer of self-assembled InAs QDs, lying on a sacrificial $Al_{0.8}Ga_{0.2}As$ layer. After deposition of the metal-dielectric mirror, using an e-beam evaporation chamber, the mirror side of the sample is glued on an host substrate (a GaAs wafer). The growth wafer is then partially removed by mechanical abrasion. We stop the abrasion $\sim 50\,\mu$m above the epitaxial layer, in order to avoid the formation of dislocations in the active layer. The remaining GaAs is selectively removed by wet etching (citric acid, H_2O_2 diluted in deionized water) with a typical etch rate of 1 μm/min. Finally, the AlGaAs sacrificial layer is selectively removed with concentrated hydrofluoric acid, ideally leaving a mirror flat semiconductor membrane, such as the one shown in Fig. 3.4(a). Of course, nanofabrication life is rarely ideal : the principal difficulty of this flip-chip step was the optimization of the epoxy baking, in order to avoid the formation of bubbles below the membrane. Even though we never achieved a success yield of 100% ; the optimization conducted during Nitin PhD allowed to increase the success yield from an initial 10% to a satisfying 80%. The next step is the structuration of the planar membrane into tapered wires. Since the wire geometry directly conditions the antenna performance, it is the most critical part of the process. We have explored several routes before finding a suitable process to obtain the desired tapered shape.

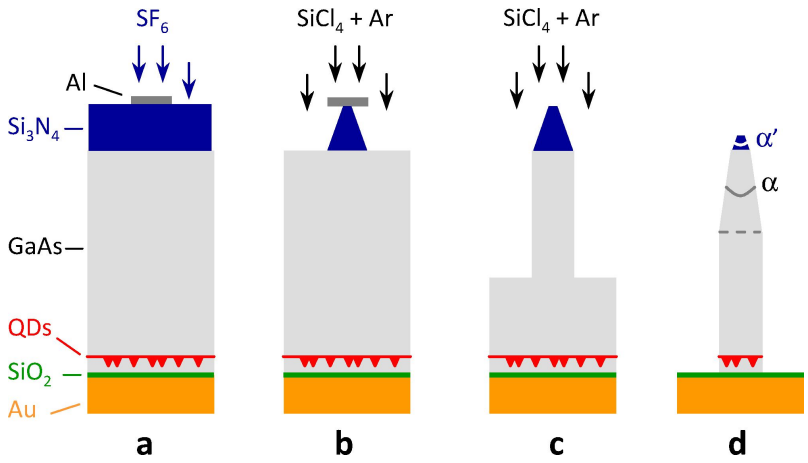

FIGURE 3.3 – **Top-down definition of needle tapers.** To obtain the top needle taper, we transfer the shape of a conical Si_3N_4 mask into GaAs. Due to the pronounced etching speed difference between Si_3N_4 and GaAs, the profile transferred into GaAs is sharpened (see text for details).

Focus Ion Beam (FIB) etching. Our first try to define sharp needles was performed with a FIB, in collaboration with Violaine Salvador. The machine was a Strata 400 dual beam system, employing gallium ions accelerated to 30 kV. The SEM images were very promizing, showing sharp tapers featuring angles below 2°. However, optical measurements were quite disappointing : we never found any optically active QD in the structures having a bottom diameter in the 200 nm range. A systematic study then showed that FIB etching leaves a "dead" layer of about 300 nm on the sidewalls, likely due to the creation of crystalline defects that strongly degrade the QD optical emission. Thus, this technique can be used to realize micron-size structures, but not wires with a 200 nm diameter. In addition, since wires are etched one by one, FIB etching is a time consuming technique.

Reactive ion etching. We thus switched to dry plasma etching using a hard mask defined by e-beam lithography. This etching technique is parallel and is much less aggressive than FIB etching. This step was conducted on a Oxford Reactive Ion Etching (RIE) system available in the CEA/DOPT/LETI clean room. Roughly, the profile achieved in RIE results from three distinct processes :

- Physical etching, due to the impact of accelerated ions on the substrate. This process is anisotropic and generates profiles with a positive slope (larger diameter at the bottom of the structure).
- Chemical etching, associated with chemically active radicals or ions that react on the surface of the substrate. This process is isotropic and leads to an underetching.
- Surface passivation, *i.e.* the deposition of a polymer or oxide layer on the sidewalls. This ingredient is essential to protect the etched structure and to obtain smooth sidewalls.

We have employed a $SiCl_4$-Ar gaz chemistry, well suited to etch GaAs and AlGaAs compounds, and began to explore the wide parameter space (chamber pressure, flow of gases, RF power), in order to obtain the desired conical shape. After numerous tests, we managed to obtain vertical sidewalls and underetched sidewalls (which is a good point to realize the photonic trumpets discussed in section 3.4), but we did not succeed to obtain directly the needle shape.

Two-step RIE etching. We finally obtained the desired tapered wires by using a two-step etching. Its principle, sketched in Fig. 3.3, is to transfer the conical shape of a Si_3N_4 mask into GaAs, after disappearance of a top Al mask. We thus first deposit a 400 nm thick Si_3N_4 layer above the GaAs membrane, and define an array of Al masks by e-beam lithography (a). The wires are defined with two successive reactive ion etching (RIE) steps. The first one uses a SF_6 gaz chemistry and is optimized to etch the Si_3N_4 layer into a cone, with a total opening angle $\alpha' \sim 40°$ (b). The second step, with a $SiCl_4$-Ar gaz chemistry, etches GaAs vertically, starting to define a wire with a diameter identical to the one of the Al mask. At some point, the Al mask is totally consumed, leaving the Si_3N_4 cone directly exposed to the etching (c). The conical shape is then transferred into GaAs, with a reduced tapering angle α because GaAs is etched faster than Si_3N_4 (d). Quantitatively, $\tan(\alpha/2) = \frac{1}{S}\tan(\alpha'/2)$, with $S \sim 10$ the selectivity of the etching. This process allows separating the definition of the bottom part of the wire (its diameter is defined by the Al mask) and the formation of the top taper.

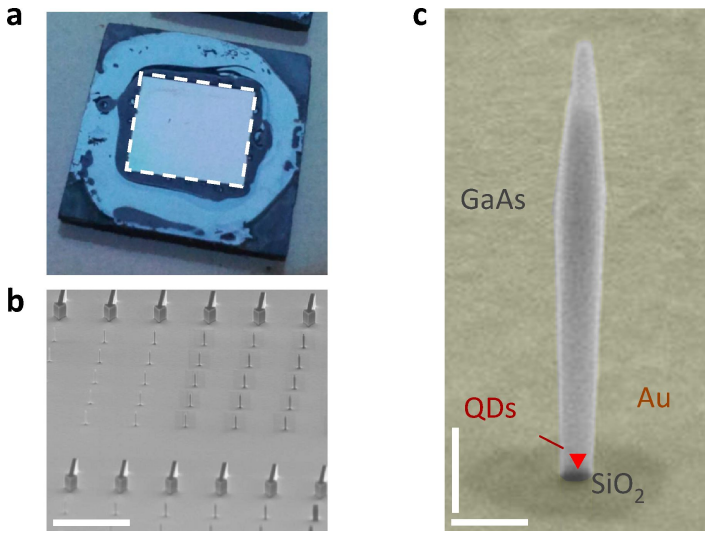

FIGURE 3.4 – **Fabricated device.** (a) Optical microscope view of a GaAs membrane transferred on an host susbtrate. The membrane, whose edges are indicated by dashed lines, is $\sim 5 \times 5$ mm. (b) SEM view of an array of etched photonic wires. Scale bar = 15 μm. (c) Zoom on a representative antenna. The QDs are located 70 nm above the mirror and the two scale bars represent 500 nm — adapted from Ref. [21].

A representative wire antenna obtained with this process is shown in Fig. 3.4(a). The wire features a sharp top taper and is cleanly connected to the bottom planar mirror. The SiO_2 layer appears as a dark disk surrounding the wire base. The wire encompasses a layer of self-assembled InAs QDs, located 80 nm above the mirror. A structure with a 200 nm diameter typically contains 5 spectrally-isolated dots with a random lateral localization. As discussed previously, this double randomness does not compromise significantly the fabrication yield.

3.2.2 Source performance

The source performance was investigated at cryogenic temperature (5 K) in a μPL setup. To excite the source, we used a pulsed Ti-Sapphire laser emitting 200 fs pulses with a repetition rate of 76 MHz. The excitation was non-resonant, with a photon energy above the GaAs bandgap. The measurements were conducted by Joël Bleuse. Figure 3.5(a) shows a series of μPL spectra, recorded for increasing pumping power P. They are dominated by the recombination of a neutral exciton (X) and a neutral biexciton (XX), as confirmed by the dependence of their spectrally-integrated intensity on P (Fig. 3.5(b)). When saturated, the two lines exhibit the same integrated intensity : this represents a first evidence of the broadband collection of the wire antenna.

Single-photon emission. Single-photon emission can be assessed through a measurement of the second order intensity auto-correlation function :

$$g^{(2)}(t, t+\tau) = \frac{\langle I(t)I(t+\tau)\rangle}{\langle I(t)\rangle\langle I(t+\tau)\rangle}, \tag{3.4}$$

where the brackets represent time averaging. For a stationary process, $g^{(2)}$ depends only on the time delay τ. For a given emission line, $g^{(2)}(\tau)$ is measured by spectrally filtering this line with a monochromator an by sending the signal to a Hanbury Brown and Twiss setup. The later employs two silicon Avalanche Photodiodes with a FWHM time-jitter of 300 ps. We consider here the X^0 line and the spectral integration window appears as a rectangle in Fig. 3.5(a). Fig. 3.5(c) shows the raw intensity autocorrelation trace for a non-resonant, pulsed laser excitation which saturates the X^0 line. After correction of a 0.03 background, the fit to theory (solid line) demonstrates $g^{(2)}(\tau = 0) = 0.02$, the signature of a very pure single-photon emission. Note that half of this value corresponds to a residual X^0 population after one repetition period ; the "intrinsic" $g^{(2)}(0)$ of the source is thus even lower, on the order of 0.01.

We attribute the clean $g^{(2)}(0)$, obtained at saturation of the emitter, under a non-resonant pumping to several positive facts :

- The small amount of semiconductor material, which limits the presence of parasitic emitters, and the low number of dots in the structure, which ensures that the lines are well spectrally isolated. Regarding these two points, Fig. 3.5(b) shows a series of clean spectra, without significant background.

- The spectrally-flat coupling to the guided mode, which suppresses non-resonant feeding effects that can be observed when non-monochromatic emitters are inserted in a high-Purcell microcavity [47, 111, 96, 49].
- The moderate SE dynamics ($1/\Gamma = 2.4$ ns), similar to the one of an InAs QD embedded in bulk GaAs, for which clean $g^{(2)}(0)$'s are also observed [89]. This moderate decay rate prevents multiple feeding of the QD from a slowly decaying charge carrier reservoir (for example the wetting layer), as observed with large oscillator strength GaAs QDs [79] or when SE is accelerated by the Purcell effect [38].

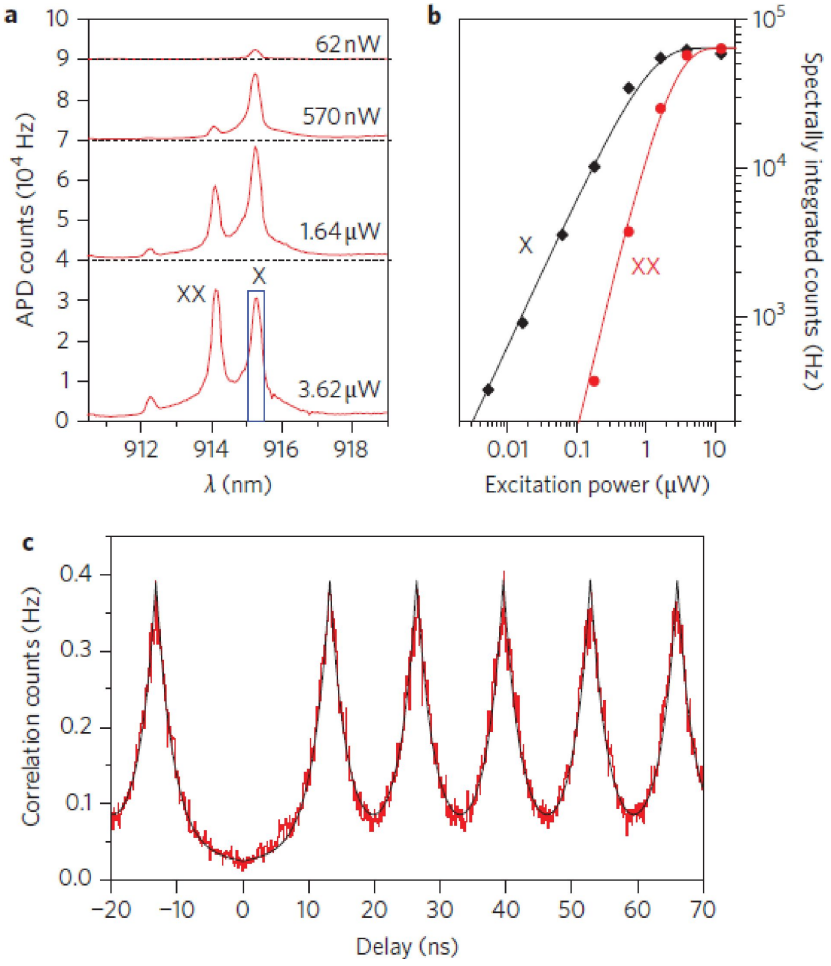

FIGURE 3.5 – **Bright and pure single-photon emission.** (a) μPL spectra of the photonic nanowire shown in Fig. 3.4(c) for increasing values of the optical pump power P. (b) Spectrally integrated counts of X and XX versus P. Below the saturation pump power $P_0 = 1$ mW, they respectively exhibit linear and quadratic dependence on P. (c) Raw autocorrelation trace of the X transition well above saturation ($P/P_0 = 4$), measured over a 0.5-nm spectral range (rectangle window in a). The solid line is a fit to theory — reproduced from Ref. [21].

External efficiency. Besides single-photon purity, the source first-lens external efficiency ϵ_{ext}, defined as the probability to emit a photon into the lens NA after a trigger pulse, is a very important figure of merit. We still consider the X transition and ϵ_{ext} can be decomposed as :

$$\epsilon_{\text{ext}} = (p_{\text{X}\geq 1}.\eta_{\text{rad}}.f_0) \times \epsilon, \tag{3.5}$$

where the terms between parenthesis are linked to the emitter and ϵ is the extraction efficiency of the antenna ; $p_{\text{X}\geq 1}$ is the probability to inject at least an exciton in the QD per excitation pulse, η_{rad} is the radiative efficiency of the dot and f_0 is the fraction of time for which the QD is in a neutral charge state. With a large enough optical pump power, $p_{\text{X}\geq 1}$ can easily be brought close to 1. Within a few percents, η_{rad} is very close to unity, as demonstrated experimentally in section 2.3. However, in the absence of an external electrical field control, charge fluctuations are less controlled in self-assembled QD. Thus, to maximize ϵ_{ext} one should first find a dot with a stable charge state, which is the case for the results reported here. Experimentally, the determination of ϵ_{ext} requires a careful calibration of the setup transmission and detector quantum efficiency. These two factors are aggregated in η_{setup} which is on the order of 10^{-3}. Details on the setup calibration procedure may be found in the Supplementary Material associated with Ref. [74]. At QD saturation, one obtains $\epsilon_{\text{ext}} = 0.72 \pm 0.09$.

In 2010, this result constituted a significant improvement over the state-of-the-art of on-demand single-photon sources ($\epsilon_{\text{ext}} \sim 0.4$). Nowdays, beside the trumpet antennas presented in the next section, there are only two other solid-state systems that reach a similar level of performance :

- A single QD integrated in a micropillar cavity ($\epsilon_{\text{ext}} = 0.78$, Ref. [34]). The structure was obtained thanks to a state-of-the-art semiconductor etching combined with a deterministic lithography technique, to define a cavity around a single dot, resonant with the excitonic transition. In addition, the authors designed a cavity with a moderate Purcell effect in order to limit the non-resonant feeding of the cavity mode by the bi-exciton transition. Finally, an intra-dot pumping, in the p-shell, was used to suppress multiple feeding from an external carrier reservoir. Interestingly, the photons emitted by this source are indistinguishable, thanks to the acceleration of SE provided by the cavity.
- A single molecule integrated in a dielectric planar antenna ($\epsilon = 0.96$ and $\epsilon_{\text{ext}} = 0.75$, Ref. [58]). The source operates at room temperature and employs a single molecule integrated in a low index dielectric stack. Though rather simple, this planar dielectric antenna offers a nearly ideal extraction efficiency over a broad range of wavelengths. It emits a doughnut-like mode that can be collected with a large NA immersion objective. In the future, this promising strategy could also be applied to colloidal quantum dots or NV centers embedded in diamond nanocrystals.

In our first generation of wire antenna, the external efficiency is primarily limited by the taper geometry. Using Eq. 3.3 with $\epsilon = \epsilon_{\text{ext}} = 0.72$, $\beta = 0.9$ and $|r_b|^2 = 0.9$, one obtains a taper transmission of 0.77, corresponding to a tapering angle $\alpha = 6°$. As illustrated in Fig. 3.1(b), decreasing further α (ideally below 2°) represents a natural route to improve

the source brightness. However, etching such ultrasharp needles represents a significant technological challenge. In this context, the direct growth of tapered nanowires constitutes an appealing fabrication route.

3.3 Bottom-up photonic wire antennas

State-of-the-art. The appealing potential of bottom-up semiconductor nanowires for optoelectronic devices, as well as applications beyond pure photonics have stimulated intense research in the last decade [62, 115, 98]. In thin wires that are compatible with a lateral confinement of the charge carriers, optically active QDs have been realized through the insertion of a longitudinal heterostructure [97, 100]. To realize a photonic wire, the first axial growth step is followed by the lateral growth of a shell, which brings the wire diameter in a range compatible with photonic confinement. Following this approach, single-photon emission was demonstrated for a GaAs QD inserted in an AlGaAs photonic wire [46]. In 2012, Ref. [83] reports on the first realization of a complete antenna (top taper and bottom mirror), using a bottom-up InP tapered wire that embeds a single InAsP QD. As seen in Fig. 3.6(a), the wire features a very sharp needle taper ($\alpha = 2°$) which ensures a nearly perfect coupling to the collection optics ($T_{2°}(0.75) = 0.98$). Clearly, a supplementary strong asset of this fabrication strategy is the integration of a single quantum emitter precisely on the wire axis.

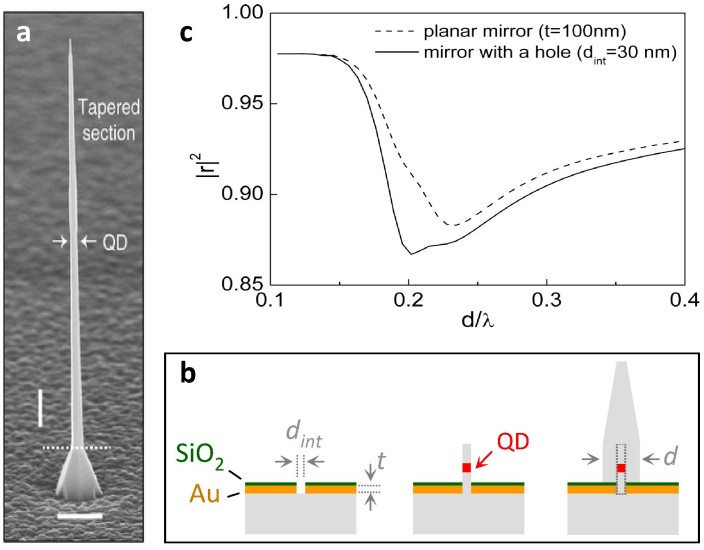

FIGURE 3.6 – **Bottom-up tapered photonic wires.** (a) Tapered InP photonic wire embedding a single InAsP QD, obtained by MOVPE (from Ref. [83]). (b) Proposed strategy to realize directly a tapered wire supported by a metal-dielectric mirror. (c) Calculated modal reflectivity for an Au (100 nm) - SiO_2 (9 nm) mirror featuring a hole with a 30 nm diameter, as a function of d/λ (continuous line). For comparison, the modal reflectivity of the planar mirror (without hole) is also shown as a dashed line.

With this approach, the integration of the bottom mirror is however more problematic. In Ref. [83], it was integrated by spin coating a polymer layer on the epitaxial sample, pealing this layer and the embedded wires and finally back-depositing a gold mirror (no dielectric spacer). With such a fabrication process, the geometry of the cleaved facet is not precisely controlled and the longitudinal position of the emitter with respect to the bottom mirror is loosely defined. In addition, immersing the wire inside a polymer reduces the background-wire index contrast, limiting the maximum β to 0.85 [43]. The resulting extraction efficiency, about 0.42, clearly shows that achieving high external efficiencies requires a simultaneous optimisation of all antenna parts.

Proposal : direct growth of a complete antenna. Building on this pioneering work, we have proposed in Ref. [22] a direct fabrication route for the whole device, which potentially solves the issues associated with the integration of the bottom mirror. The idea, sketched in Fig. 3.6(b), is to cover the growth substrate with metal and dielectric layers, both patterned with tiny holes. The holes will localize the growth of the wire while being small enough to not compromise the reflectivity of the bottom mirror. This proposal is supported by numerical results presented in Fig. 3.6(c). For practical reasons, it is desirable to reduce the thickness of the metal. We thus consider here a 100 nm thick gold layer covered by 9 nm of silica (another metal, like Al could also be employed). Fig. 3.6(c) shows that a 30 nm hole has a minor impact on the reflectivity, and that $|r|^2 > 0.87$ can be obtained with this approach.

3.4 Photonic trumpet antennas

We have seen that very sharp needle tapers can be obtained by a bottom-up approach. However, their top-down fabrication constitutes a very challenging goal. To relax the constraint on the tapering angle, we consider in this section optical antennas that exploit the opposite tapering strategy, leading to a device that we have nicknamed "photonic trumpet". We first compare the two tapering strategies and then discuss the realization of a bright single-photon source based on a photonic trumpet. In particular, the device features a well-controlled Gaussian far-field emission, a key asset for many advanced applications.

3.4.1 Comparing the two tapering strategies

Starting from the diameter d_{bot} which optimizes the β-factor, there are two possibilities to increase the mode surface S_{eff}. As illustrated in Fig. 2.2 (previous chapter), one can either decrease the diameter, which leads to a needle-like taper, or increase it, which leads to a trumpet-like taper. In this paragraph, we compare the tapering strategies in terms of mode transmission along the tapered section and far-field emission. We consider linear tapers characterized by their total opening angle α. For a fair comparison, the top diameters d_{top} are chosen to ensure the same collection of light using a NA=0.75 lens : $d_{\mathrm{top}} = 166\,\mathrm{nm}$ and $d_{\mathrm{top}} = 1.5\,\mu\mathrm{m}$ for the needle and trumpet taper, respectively.

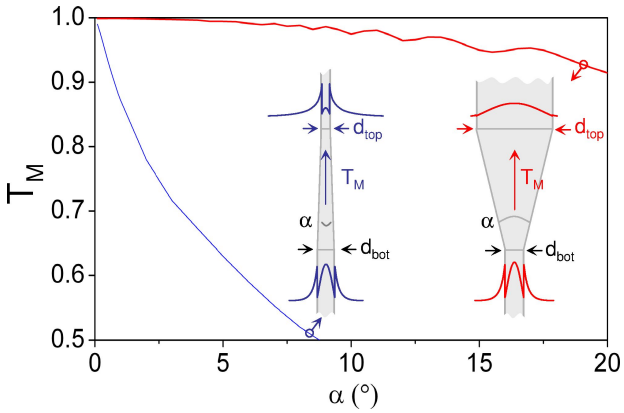

FIGURE 3.7 – **Fundamental guided mode in a tapered wire.** Modal transmission of HE_{11} (T_M), plotted against the tapering angle α for two representative tapers (see text for details). Typical electrical field profiles are also shown (amplitude of the discontinuous component) — reproduced from Ref. [74].

Propagation along the tapered section. To investigate the propagation of HE_{11} along a tapered section, we introduce the modal transmission T_M, which is plotted against α in Fig. 3.7. For α up to 5°, a photonic trumpet ensures a nearly perfect adiabatic expansion of HE_{11}, leading to $T_M > 0.994$. On the other hand, for the same angle range, the needle taper already suffers from significant non-adiabatic losses : a fraction of the injected light is then emitted into free space, before reaching the end of the tapered section. Qualitatively, the striking contrast between the two tapers can be understood by inspecting Fig. 2.2. For a needle taper S_{eff} scales as $d^{-5.5}$ whereas for the trumpet S_{eff} scales as $d^{1.9}$. Along the taper, the rate of change in diameter is governed by α. For a given α, a weaker dependence of S_{eff} on d implies slower changes in the mode profile during its propagation, which eases its adiabatic transformation. In a trumpet with $\alpha > 5°$, HE_{11} experiences an increasing coupling to higher order guided modes. The propagation dynamics is then more complex, with back and forth coupling to higher order guided modes. Still, T_M exceeds 0.95 for α as large as 15°.

Far-field emission : total transmission. We now consider a $h = 12\,\mu$m high trumpet taper emitting into a lens with a numerical aperture (NA) of 0.75, which corresponds to the experimental realization detailed later in the section. Given the high value of T_M, the far-field emission is essentially governed by the scattering of HE_{11} when it reaches the top facet. Since its diameter d_{top} can be accurately controlled by a standard fabrication process, this ensures reproducible taper performances. To suppress the top facet reflectivity, we cover it with a dielectric layer having a $\lambda/4$ optical thickness and a refractive index $n_{\text{ar}} = 1.99$ which is close to the optimal value $\sqrt{n_c n} = 1.86$. For $d_{\text{top}} > 1.5\,\mu$m, the facet reflectivity is then smaller than 10^{-2}. We first consider the total transmission T into a NA=0.75 collection lens for both tapers. For a trumpet taper, this quantity is plotted as a dashed line against α and the corresponding d_{top} in Fig. 3.8(a). Since the taper and top facet

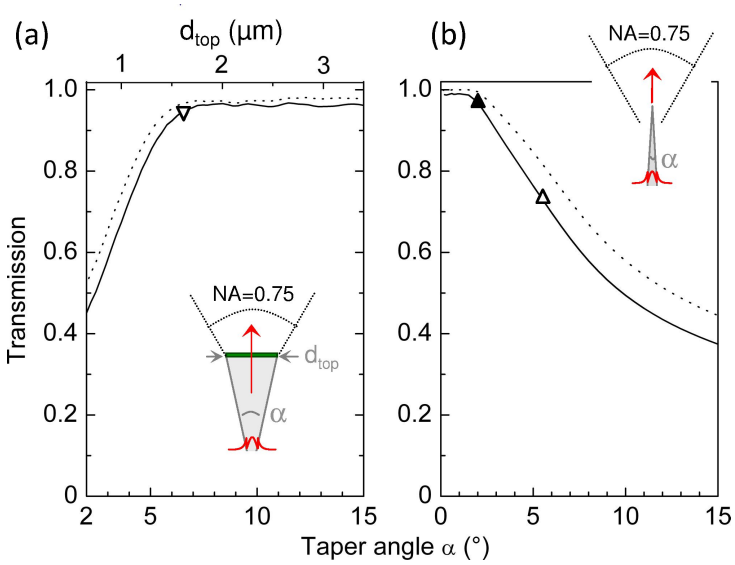

FIGURE 3.8 – **Far-field emission.** (a) Calculated total transmission T into a NA=0.75 lens (dashed line) and mode matching to a Gaussian beam $\mathcal{M}_g$ (solid line). The calculations are conducted for a 12 μm high photonic trumpet — adapted from Ref. [74].

reflectivities are negligible, T essentially depends on the divergence of the output beam. For $d_{\text{top}} > 1.5\ \mu$m, which corresponds to $\alpha > 6°$, T exceeds 0.96. Calculation shows that this result is maintained for very large angles, up to 30°. In this case, the propagation inside the taper is no longer adiabatic, however the output beam is directive enough to ensure a large T. This angle tolerance contrasts with the needle case, illustrated in Fig. 3.8(b). Indeed, achieving $T > 0.96$ imposes a stringent condition on the tapering angle ($\alpha < 3°$). Moreover, an inspection of Fig. 3.7reveals that, even for such small angles, the needle taper is not completely adiabatic. Light leaks into free-space before reaching the taper end. From an external point of view, these leaks are however not necessarily detrimental, as long as they can be collected by the optics.

Far-field emission : transmission to a Gaussian beam. Besides its directivity, the spatial structure of the emitted beam is also important. In particular, a Gaussian structure is desirable for a number of applications or experimental situations (to feed efficiently single photons into a single-mode optical fiber for quantum encrypted communications [39], or, reversibly, to implement an optical switch at the single-photon level [63]). We thus introduce the transmission T_g to a Gaussian beam intercepted by the NA=0.75 collection lens. This figure of merit aggregates both the beam directivity and the mode matching a Gaussian beam $\mathcal{M}_g = T_g/T$. T_g is plotted as a solid line for trumpet and needle tapers in Fig. 3.8(a) and (b), respectively. In the first case, T_g closely follows T : this is expected because of the favourable profile of HE_{11} in the top facet plane (see inset in Fig. 3.7). A needle taper with a small angle ($\alpha < 2°$) can also offer a Gaussian emission. For larger angles however, T_g steeply drops.

To conclude this comparison, both tapers can offer a directive Gaussian emission. However, the trumpet taper offers optimal performance on a much broader range of tapering angles. Of course, such a tolerance considerably alleviates fabrication constraints. In the following, we illustrate the feasibility of trumpet tapers and discuss the performance of a bright single-photon source based on this approach.

3.4.2 Nanofabrication

The optimization of the fabrication process has been conducted in the end of Nitin's PhD. Globally, the process follows the same steps than previously presented in Fig. 3.2. Differences arise in the final step, in which the trumpets are defined by a RIE plasma etching. We also used a $SiCl_4$-Ar gaz chemistry, but the recipe was optimized to provide the right balance between physical sputtering and chemical etching, so as to obtain a constant underetching angle. Another difficulty in the realization was to find a mask that survives during the very long etching time (typically $2-3$ hours).

The initial epitaxial planar structure is presented in Fig. 3.9(a) : the GaAs layer in which the trumpet will be defined is 12 μm high. After deposition of the Au-SiO_2 mirror and flip-chip, the future anti-reflection layer is deposited on the sample (115 nm of Si_3N_4). As illustrated in the next figure panels, we then use e-beam lithography, metal deposition and lift-off to define arrays of 150 nm thick disks made of nickel. The Si_3N_4 layer is then etched in the RIE chamber, using a SF_6 gaz chemistry (b) and the trumpets are defined with the $SiCl_4$-Ar RIE etching mentioned above (c). Finally, the Ni mask is removed with a solution of diluted nitric acid (d).

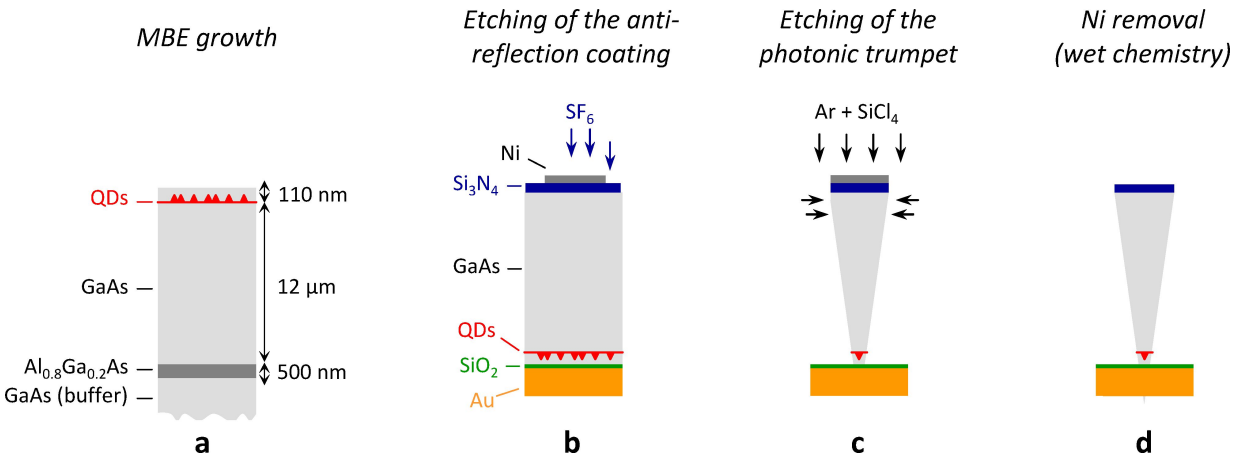

FIGURE 3.9 – **Fabrication of photonic trumpets.** (a) Schematics of the epitaxial planar structure. The deposition of the planar mirror and the flip-chip step are identical to the ones used to fabricate needle antennas. To obtain the top trumpet taper, one first deposits a Si_3N_4 anti-reflection layer and defines a Ni hard mask. The Si_3N_4 is etched (b), and the GaAs is etched with a carefully optimized RIE process, leading to a controlled undercut (c). Finally, the Ni hard mask is removed by wet chemistry (d).

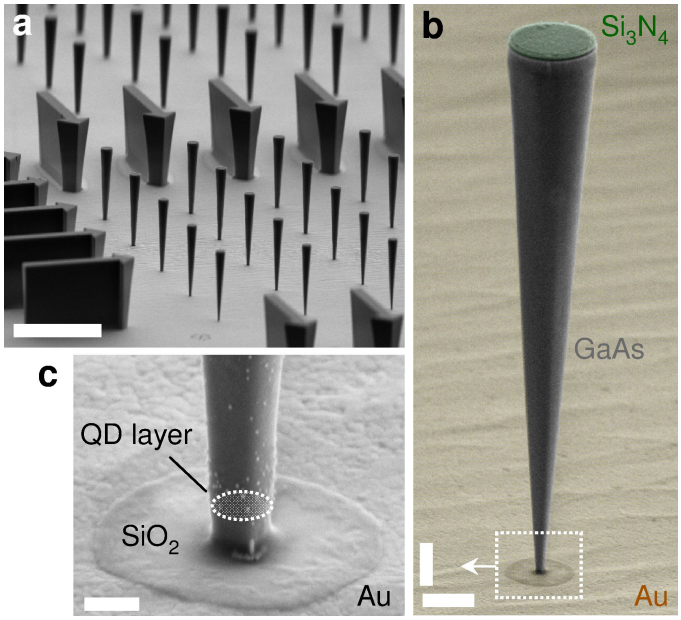

FIGURE 3.10 – **Fabricated trumpet antennas.** (a) Scanning electron microscope view of a large field of devices ; scale bar : 15 μm. (b) Zoom on a representative device (false colors) ; vertical and horizontal scale bars : 1 μm. (c) Zoom on the connection between the trumpet and the integrated mirror ; scale bar : 200 nm — reproduced from Ref. [74].

A false color SEM picture of a representative device is shown in Fig. 3.10(b) : it consists of a 12 μm high cone with a tapering angle $\alpha = 6.5°$. Its top facet features a diameter $d_{\text{top}} = 1.55\,\mu$m and is covered by the Si_3N_4 anti-reflection coating. The bottom part of the trumpet presents a diameter in the $200 - 240$ nm range, corresponding to the optimum mode confinement. The structure is connected to a gold-silica planar mirror and embeds a few ($\sim 5 - 10$) InAs self-assembled QDs, located 110 nm above the mirror. The large SEM view in Fig. 3.9(a) illustrates the reproducibility of the fabrication ; the zooms in Fig. 3.9(b) and (c) show the excellent control over the trumpet geometry, notably the connection to the planar mirror. Despite their high-aspect ratio, these structures are robust enough to be manipulated in the lab without specific precaution. In fact, the final processing step, which involves wetting and de-wetting by a liquid solution, constitutes in itself a stringent test for the structure resistance.

3.4.3 Optical characterization

The device was characterized using the same procedure than described in section 3.2.2 (μPL spectra, measurement of $g^{(2)}(\tau)$ and determination of ϵ_{ext}). To avoid heating of the wire, the excitation energy was tuned below the GaAs bandgap, in the absorption continuum of the QD wetting layer. The measurements were performed by Mathieu Munsch,

who was postdoc in the team at the time. First, Fig. 3.11(a) shows the distribution of light emitted by the QDs in the plane of the top facet. At the location of the QDs, only HE_{11} is guided by the structure and all the QDs contribute to the signal (no spectral filtering). This map, which is a convolution of the setup optical response by the mode profile, features a Gaussian profile, in agreement with the previous theoretical results. Focusing on line 2 appearing in the micro-PL spectra shown in Fig. 3.11(b), the external efficiency at saturation was found to be $\epsilon_{\text{ext}} = 0.75 \pm 0.1$, after correction for residual multi-photon emission. This value is slightly above the one obtained with the needle antenna, and slightly below the 0.89 maximum theoretical value for an ideal emitter integrated in the realized geometry.

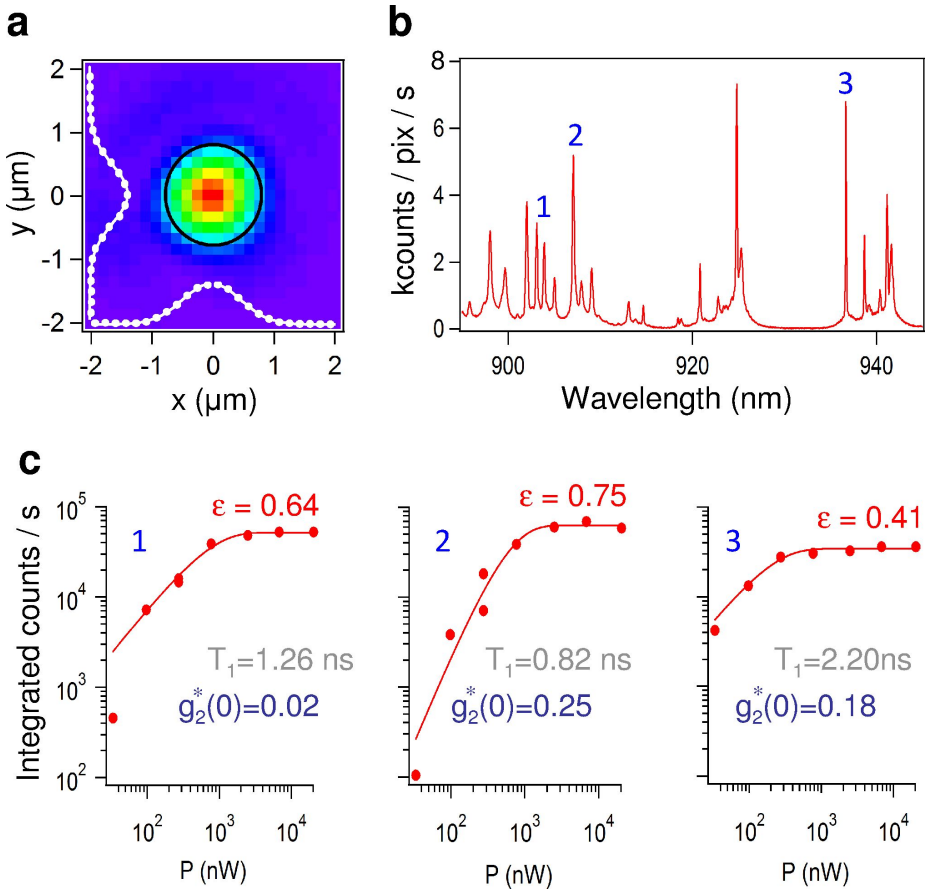

FIGURE 3.11 – **Optical characterization.** (a) Spatial distribution of the intensity in the top facet plane. Two diameter cuts and their fit to a Gaussian profile are also shown. The circle represents the facet circumference. (b) Micro-photoluminescence spectrum, measured at $T = 5\,\text{K}$ for an excitation power $P = 20\,\mu\text{W}$. (c) Spectrally integrated intensity of the lines 1, 2 and 3, extracted from a fit to a Lorentzian lineshape, as a function of P. The solid lines are theory, assuming an excitonic emission (lines 1 and 3) and biexcitonic emission (line 2). For each transition, the luminescence decay time T_1, the background-corrected intensity autocorrelation value $g_2^\star(0)$ is also shown — reproduced from Ref. [74].

Using the calculated value of $\mathcal{M}_g = 0.97$, the external coupling efficiency to a Gaussian beam reaches $\epsilon_{\text{ext}}\mathcal{M}_g = 0.73 \pm 0.09$. Such a large value is very promising for to couple the dot emission to a single-mode optical fiber, with applications to long-range quantum communications. Reversibly, it is also interesting to address efficiently the dot with a Gaussian, free-space, resonant laser beam. The giant non-linearity associated with the saturation of the quantum dot absorption [7, 27] can then be exploited to downscale optical switches down to the single-photon level, as recently demonstrated with a QD-micropillar system [63]. More generally, one can explore the rich physics of 1D atoms (a single quantum system coupled to a single optical mode) in the special case where the optical mode is a guided mode and not a localized cavity mode. In particular, the broadband nature of a waveguide is well suited to realize "multicolor" experiments, in which several detuned transitions may be simultaneously addressed. We will come back to these points in the next chapter.

Summary

In this chapter, we have discussed the design, fabrication and characterization of optical antennas based on photonic wires. Such antennas exploit both the broadband spontaneous emission control provided by a single-mode photonic wire and an engineering of the wire far-field emission using a planar bottom mirror and a tapering of the wire upper extremity. We have considered and realized needle-like and trumpet-like tapers : both strategies lead to large extraction efficiencies. Needle antennas are relatively compact, and compatible with a direct fabrication by growth. Photonic trumpets feature a larger aspect ratio, but are much more tolerant against fabrication imperfections. Moreover, in a near future, realistic improvement in the trumpet geometry should allow us to realize a nearly perfect interface between a embedded emitter and a very low divergence Gaussian beam. Indeed, by further increasing the top facet diameter, we can improve the beam directivity. For example, a 12 μm high trumpet with a top diameter of 2.6 μm ensures $T_g = 0.93$ into a lens with NA=0.5. So far, we have mostly applied the antennas to realize bright sources of single photons. Though it is an important device for quantum communication, the potential of the broadband optical antenna goes well beyond this first realization. In the next chapter, we discuss (in French) some on-going work and research perspectives for the years to come.

Chapitre 4

Travaux en cours et perspectives

Ce chapitre passe tout d'abord en revue quelques projets en cours qui exploitent les trompettes photoniques dans leur forme actuelle. Ensuite, nous verrons pourquoi il est intéressant d'intégrer de nouvelles fonctionnalités à ces objets. En particulier, nous considérerons successivement i) l'intégration d'une nanocavité dans une trompette photonique, pour accélérer l'émission spontanée tout en préservant une bande passante raisonnable pour l'antenne optique et ii) le contrôle des propriétés optiques fines de l'émetteur par un champ externe (champ électrique, contrainte...). Ces approches, qui peuvent être combinées, visent entre autres, la réalisation de sources de lumière quantique avancées.

4.1 Quelques travaux en cours

Dans leur forme actuelle, les structures photoniques décrites dans le chapitre précédent permettent déjà d'étudier de nouveaux phénomènes, dans le cadre de l'optique quantique en guide d'onde ou dans le contexte de l'optomécanique des systèmes hybrides. Ces projets sont menés en étroite collaboration avec des collègues de l'équipe NPSC et de l'Institut Néel.

4.1.1 Optique quantique dans un guide d'onde (spectroscopie résonante)

Un fil photonique contenant une boîte quantique constitue un atome unidimensionnel [102], c'est-à-dire un unique atome couplé à un seul mode électromagnétique (ici le mode guidé fondamental). De plus, grâce au taper supérieur, le mode guidé est très bien couplé à un faisceau Gaussien se propageant dans l'espace libre. Ce type de système, conceptuellement très simple, est néanmoins très riche. Ainsi, un faisceau résonant avec la transition atomique et de faible intensité (typiquement un photon par temps de vie de l'émetteur) suffit à saturer la boîte quantique. C'est le phénomène de non-linéarité géante [7], d'abord démontré avec des microcavités optiques [27] et qui peut être mis à profit pour réaliser un interrupteur tout optique à l'échelle du photon unique [27, 84, 63, 106, 13]. Plus gé-

néralement, lorsqu'un émetteur est fortement couplé au continuum 1D associé à un mode guidé (dans le sens $\beta \to 1$), il devient possible de mettre en évidence des effets d'électrodynamique quantique en guide d'onde, une thématique émergente surtout explorée pour l'instant par des études théoriques [86, 122]. Par exemple, la Ref. [54] propose de générer une interaction non-linéaire entre deux photons de couleur différente, en exploitant un émetteur à trois niveaux.

Dans tous les cas, les effets cohérents mis en jeu sont très sensibles à la stabilité et à la pureté spectrale des émetteurs. Pour les fils gravés, nous avons montré récemment qu'une dérive spectrale de l'exciton, associée à des effets de surface, peut être supprimée avec une passivation des flancs du fil [117]. L'étude de la largeur de raie sous excitation strictement résonante est en cours. Les premiers résultats sont encourageants, avec des largeurs de raies de l'ordre de 5 μeV. A terme, l'intégration d'une nanocavité dans un fil photonique, qui sera discutée dans la section 4.2.3, permettra de diminuer le temps de vie radiatif de l'émetteur et donc de le rendre moins sensible aux phénomènes de déphasage.

Ces thématiques sont explorées en collaboration avec des collègues de l'Institut Néel. Les expériences de spectroscopie résonante sont menées par Gilles Nogues, Jean-Philippe Poizat et al., avec le support théorique d'Alexia Auffèves. Ces thématiques sont soutenues par le projet ANR blanc 'WIFO', dont je suis responsable CEA. Les trompettes photoniques seront également exploitées pour des expériences de spectroscopie résonante non-linéaire (mélange à quatre ondes), dans le cadre de l'ERC starting grant 'PICSEN', portée par Jaceck Kazprack.

4.1.2 Un système hybride pour l'optomécanique

Les systèmes optomécaniques hybrides, dans lesquels un système quantique à deux niveaux est couplé à un mode résonant d'un oscillateur mécanique, suscitent actuellement un grand intérêt [99]. Un tel système crée une passerelle entre les mondes quantique et classique. En effet, un résonateur mécanique est *a priori* un système classique pour deux raisons : i) il est constitué d'un nombre macroscopique d'atomes et, ii) dans la limite des excitations modérées, il peut être décrit par oscillateur harmonique, un système linéaire pour lequel il est difficile d'observer un comportement quantique. A l'opposé, le système à deux niveaux présente une très forte non-linéarité et donc des effets quantiques prononcés. L'objectif est alors de transférer des effets quantiques au mode du résonateur avec des applications potentielles aux technologies quantiques de l'information et à l'exploration de la frontière classique-quantique.

En collaboration avec des collègues de l'Institut Néel, nous avons montré qu'une trompette photonique contenant une boîte quantique constitue un système optomécanique hybride original ([116], couverture de *Nature Nanotechnology*). L'énergie d'un complexe excitonique piégé dans la boîte est ici couplée à un mode de vibration mécanique discret de la trompette, via la contrainte du matériau. Cette méthode de couplage, initialement proposée dans la Ref. [110], permet d'atteindre de grandes valeurs pour le terme de couplage

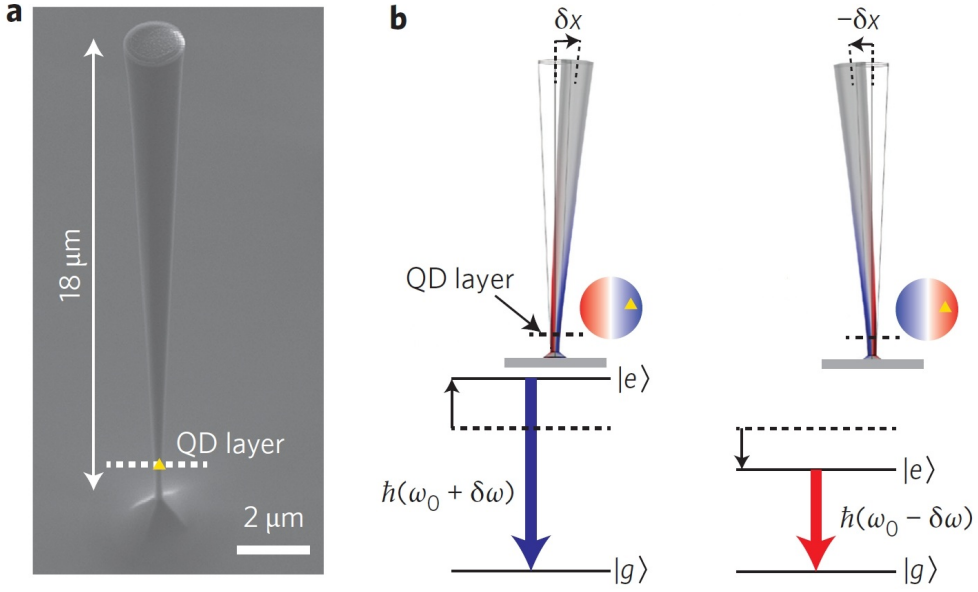

FIGURE 4.1 – **La trompette photonique comme système optomécanique hybride**. (a) Image MEB de la structure. (b) Illustration de l'effet d'une vibration mécanique sur l'énergie d'un exciton piégé dans la boîte quantique. La couleur bleue correspond à une contrainte compressive, le rouge correspond à une expansion — reproduit de la Ref. [116].

optomécanique. Plus précisément, le Hamiltonien du système couplé prend la forme :

$$\mathcal{H} = \hbar\Omega_m\left(\hat{a}^\dagger\hat{a} + \tfrac{1}{2}\right) + \hbar\omega_{eg}\frac{\hat{\sigma_z}}{2} + \hbar g_0(\hat{a}^\dagger + \hat{a})\hat{\sigma}_z. \tag{4.1}$$

Le premier terme, qui correspond à un oscillateur harmonique, décrit un mode de vibration discret résonant à la fréquence angulaire Ω_m ; l'opérateur d'échelle $\hat{a}^\dagger$ crée un phonon dans l'oscillateur. Le second terme décrit la boîte quantique, réduite ici à un système à deux niveaux : l'état fondamental $|g\rangle$ est la boîte vide d'excitation et l'état excité $|e\rangle$ correspond à un exciton piégé dans la boîte. L'énergie séparant ces deux états est notée $\hbar\omega_{eg}$ et $\hat{\sigma}_z = |e\rangle\langle e| - |g\rangle\langle g|$ est l'un des opérateurs de Pauli du système à deux niveaux. Pour finir, le troisième terme introduit un couplage entre l'énergie du système à deux niveaux et la coordonnée spatiale de l'oscillateur mécanique, $\hat{x} = \delta x_{\text{zpf}}/\sqrt{2} \times (\hat{a}^\dagger + \hat{a})$. Cette coordonnée correspond ici à la position de la facette supérieure et δx_{zpf} est l'amplitude RMS des fluctuations de point zéro de cette position. La force du couplage est donnée par g_0, qui a la dimension d'une fréquence angulaire :

$$g_0 = \left.\frac{d\omega_{eg}}{dx}\right|_{x=0} \delta x_{\text{zpf}}. \tag{4.2}$$

La trompette utilisée pour la première série d'expériences a une hauteur de 17 μm, un angle d'ouverture $\alpha = 4°$ et un diamètre à la base de 500 nm (Fig. 4.1(a)). Il n'y a pas de

miroir inférieur : la trompette est directement connectée au substrat de GaAs. On considère ici le mode de vibration fondamental qui correspond à une flexion autour de la base ; ce mode est non dégénéré car la base de la trompette est légèrement asymétrique. Sous vide et aux températures cryogéniques, il résonne à une pulsation $\Omega_m = 2\pi \times (520\,\mathrm{kHz})$ et présente un facteur de qualité $Q_m = 3000$. Comme illustré sur la Fig. 4.1(b), la vibration mécanique induit un champ de contrainte uniaxial qui est maximal au voisinage de la base. En coupe, ce champ de contrainte présente un axe neutre perpendiculaire à la direction de vibration, et son intensité augmente lorsque l'on s'éloigne de cet axe. Pour une boîte hors-axe, la contrainte induit une variation de l'énergie d'un exciton piégé dans la boîte [(1)]. Outre l'extraction efficace et large bande de la lumière émise par la boîte, la géométrie trompette permet ici de concentrer l'énergie élastique au voisinage de la boîte et donc de maximiser le stress vu par cette dernière. Un déplacement de la facette supérieure de 10 nm modifie ici la longueur d'onde d'émission de la boîte de 1 nm. L'amplitude du terme de couplage atteint ainsi $g_0 = 2\pi \times (450\,\mathrm{kHz})$, positionnant ce système hybride à l'orée du régime de couplage "ultrafort" défini par $g_0 > \Omega_m$. Dans ce régime, les positions moyennes de l'oscillateur x_g et x_e pour une boîte dans son état fondamental et excité sont séparées par une distance excédant les fluctuations de point zéro δx_{zpf}.

Les perspectives ouvertes par cette première réalisation sont très riches. Les premières expériences ont démontré l'effet de la vibration mécanique sur l'énergie d'émission de la boîte quantique. Réciproquement, en excitant la boîte quantique en régime résonant pulsé, on peut générer un état de phonon cohérent pour le mode de vibration [**?**]. A plus long terme, on peut aussi envisager une mesure non destructive de l'état de la boîte à travers une mesure de la position de la facette supérieure.

Les trompettes utilisées pour les premières expériences ont un angle d'ouverture relativement modeste ($\alpha = 4°$). Pour augmenter encore le terme de couplage et rentrer franchement dans le régime de couplage ultrafort, il est intéressant d'augmenter α pour concentrer plus encore la déformation élastique à la base de la structure et donc augmenter le stress vu par la boîte. Par ailleurs, des calculs récents ont montré que l'extraction de lumière par la trompette reste très bonne pour des angles d'ouverture allant jusqu'à $30°$ [(2)]. La prochaine génération d'oscillateurs combinera ainsi des propriétés photoniques et mécaniques optimisées.

Les expériences correspondantes sont réalisées par des collègues de l'équipe mixte et de l'Institut Néel (Olivier Arcizet, Gilles Nogues, Jean-Philippe Poizat, Maxime Richard et al.)., avec le support théorique d'Alexia Auffèves.

(1). La partie hydrostatique du champ de contrainte modifie le gap des semiconducteurs et la partie anisotrope modifie l'énergie de la bande de valence.

(2). La transmission du taper est alors multimode : on perd le diagramme de rayonnement Gaussien mais le faisceau émis reste très directif.

4.2 Une nanocavité dans une trompette photonique

Le premier paragraphe de cette section décrit l'émission de photons uniques indiscernables et de paires de photons intriqués en polarisation par une boîte quantique. Ces deux types d'états quantiques constituent une ressource très importante pour les communications quantiques ou le traitement quantique de l'information. Dans ce contexte, nous soulignons l'intérêt d'une accélération de l'émission spontanée pour générer ces états avec une meilleure fidélité. Nous proposons ensuite d'inclure une nanocavité dans la trompette. Pour un volume modal faible, il est possible d'obtenir une accélération significative ($F_p \sim 6$) avec une résonance optique relativement molle ($Q \sim 100$), qui préserve une bande passante de l'ordre de 10 nm.

4.2.1 Photons uniques indiscernables

Des photons indiscernables partagent des modes spatiaux et temporels identiques. Lorsqu'ils arrivent sur les deux ports d'entrée d'un *beam splitter*, une interférence constructive liée à leur nature bosonique génère en sortie des états de Fock à deux photons. Ce phénomène de coalescence est l'un des piliers sur lesquels s'appuie le calcul quantique reposant sur l'optique linéaire [53]. Nous avons vu au chapitre précédent qu'une trompette photonique permet de canaliser l'émission d'un émetteur ponctuel vers un faisceau Gaussien, remplissant la première condition d'indiscernabilité. La seconde condition, portant sur la forme temporelle de la fonction d'onde décrivant le photon, implique tout d'abord une longueur d'onde centrale identique pour les photons. Si on utilise des boîtes quantiques, la dispersion inhomogène inhérente à ces émetteurs impose l'utilisation d'un champ externe pour contrôler l'énergie d'émission et la stabiliser sur une valeur précise ; ce point sera détaillé dans la section 4.3. Ensuite, il faut s'assurer que la largeur spectrale du photon est uniquement limitée par la durée de vie radiative de l'émetteur. En empruntant le langage de la Résonance Magnétique Nucléaire, on définit un temps de cohérence T_2 du photon, correspondant dans le domaine des fréquences angulaires à une largeur de raie à mi-hauteur $\Delta\omega = 2/T_2$. Considérant un émetteur avec une durée de vie radiative moyenne T_1, le degré d'indiscernabilité des photons s'écrit :

$$I = \frac{T_2}{2T_1}, \quad \text{avec} \quad T_2 \leq 2T_1. \tag{4.3}$$

Si la largeur de raie est dominée par la contribution liée à la durée de vie radiative, soit $\Delta\omega = 1/T_1$, les photons émis sont parfaitement indiscernables.

La matrice solide qui entoure une boîte quantique semiconductrice abrite potentiellement plusieurs sources de déphasage. Pour les boîtes InAs/GaAs aux températures cryogéniques, on peut citer au moins deux contributions, dont le contenu fréquentiel et l'amplitude ont été récemment analysés en détail [55]. Tout d'abord, la boîte est en général entourée par des impuretés ou des défauts structuraux qui constituent autant de pièges de charges peu profonds. Les fluctuations temporelles de l'état de charge de ces pièges génèrent alors un champ électrique aléatoire, qui élargit la transition optique via l'effet Stark confiné

quantique [50]. De plus, si les noyaux des éléments constituant la matrice semiconductrice portent un spin, les fluctuations du champ magnétique associé (champ Overhauser) se couplent au spin électronique. Mise à part une amélioration de la qualité structurale des matériaux employés, on peut globalement distinguer deux stratégies pour atteindre la limite d'indiscernabilité.

Augmenter T_2. Pour améliorer T_2, une première idée consiste à exciter sélectivement l'émetteur, afin de limiter l'apport d'énergie aux degrés de liberté non contrôlés de son environnement. Dans le cas des boîtes quantiques, une excitation optique intra-boîte, sur les états orbitaux p, a d'abord été utilisée [88]. Une excitation strictement résonante sur la couche s donne les meilleurs résultats, au prix d'une forte complication expérimentale : il s'agit de rejeter très efficacement le signal d'excitation pour ne collecter que la fluorescence résonante de la boîte. Récemment, l'injection d'un exciton dans la boîte grâce à une impulsion de Rabi π a permis d'obtenir à la demande des photons uniques indiscernables très purs [45]. On peut également mentionner les expériences en régime continu, dans le régime de diffusion élastique (ou diffusion de Rayleigh). Le temps de cohérence des photons émis est alors directement hérité de celui du laser d'excitation [76, 69].

Diminuer T_1. Plus l'émetteur est rapide, moins il sera sensible aux phénomènes de déphasage. C'est par exemple le cas d'excitons neutres liés à une impureté unique de fluor, localisée dans un puits quantique ZnSe/ZnMgS. Ce système a permis d'observer le phénomène de coalescence de photons avec $I = 65\%$ pour deux photons émis par *deux émetteurs distincts* [87]. Les boîtes quantiques à grande force d'oscillateur, comme les boîtes GaAs/AlGaAs [94], ou les boîtes InAs/GaAs recuites [44] sont également intéressants dans ce contexte. L'accélération de la dynamique radiative peut également être obtenue en intégrant l'émetteur dans une structure photonique bien choisie, comme une microcavité [88, 34]. Nous nous intéresserons plus particulièrement à ce dernier point dans la suite du chapitre.

4.2.2 Paires de photons intriqués en polarisation

En exploitant la cascade radiative du bi-exciton neutre piégé par une boîte quantique, il est possible d'émettre des paires de photons intriqués en polarisation [119, 2, 25]. Dans la suite, nous utilisons une base de polarisations optiques linéaires $\{H, V\}$ alignée sur les axes de symétrie de la boîte. Les deux excitons brillants sont notés $\mathrm{X_H}$ et $\mathrm{X_V}$ et le bi-exciton XX. Comme illustré sur la Fig. 4.2, une cascade radiative génère l'état intriqué en polarisation [92] :

$$|\psi(\tau)\rangle = \frac{1}{\sqrt{2}}\big(|H_{\mathrm{XX}}H_{\mathrm{X}}\rangle + e^{i\phi(\tau)}|V_{\mathrm{XX}}V_{\mathrm{X}}\rangle\big). \tag{4.4}$$

La phase $\phi(\tau)$ apparaissant dans cette expression vaut $S\tau/\hbar$, avec S l'écart en énergie entre les excitons brillants (ou *splitting* de structure fine) et τ le délai aléatoire séparant l'émission de l'exciton de celle du bi-exciton. Lorsque S est nul ou négligeable devant

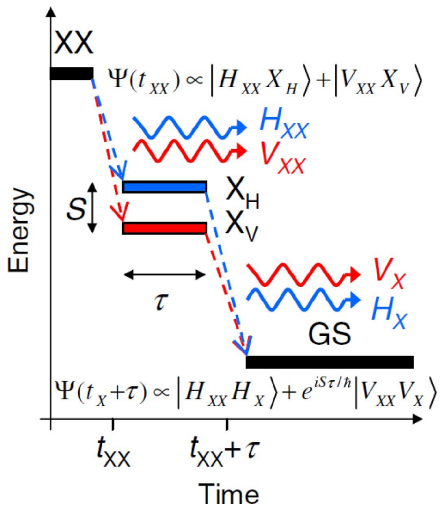

FIGURE 4.2 – **Emission de paires de photons intriqués par une boîte quantique.** On considère ici la cascade radiative bi-exciton neutre (XX) → excitons neutres brillants (X_H et X_V) → boîte vide (GS). Les états excitoniques sont séparés par un *splitting* de structure fine S — reproduit de la Ref. [92].

$\hbar/\tau$, chaque cascade radiative conduit au même état intriqué. Cette situation idéale n'est malheureusement pas la règle : en général, la boîte quantique présente une asymétrie structurale qui implique $S \neq 0$. La phase accumulée ϕ croît alors avec le délai aléatoire τ, et chaque répétition de l'expérience produit un état intriqué aléatoire différent. Si on considère $S = 5\,\mu$eV, ϕ varie de 0 à $2.4 \times \pi$ pour τ entre 0 et 1 ns. En première approche, on peut obtenir un état intriqué mieux défini en réalisant un filtrage spectral qui réduit le S apparent [2], ou une post-sélection temporelle qui réduit la dispersion de τ [92]. Toutefois, le prix à payer est une diminution considérable de la brillance de la source. En conséquence, différents groupes se sont attachés à réduire S, soit en symétrisant l'émetteur par un recuit rapide postcroissance [26], soit en utilisant un champ de contrôle externe (champ magnétique [93, 119], électrique [10], contrainte, ou une combinaison des deux [101]). L'autre stratégie consiste à diminuer la durée de vie radiative, pour diminuer la dispersion de τ. Une fois encore, cette accélération peut être obtenue au niveau de l'émetteur, ou induite par une structure photonique. La principale difficulté est ici d'accélérer simultanément les transitions bi-excitoniques et excitoniques, qui sont désaccordées spectralement. A notre connaissance, ceci n'a été réalisé qu'une fois, en exploitant deux résonances d'une molécule photonique définie à l'aide d'une technique de lithographie optique déterministe [25].

4.2.3 Une nanocavité dans une trompette photonique

Les paragraphes précédents soulignent l'intérêt d'une dynamique d'émission spontanée rapide pour réaliser des sources de lumière quantique avancées. En gardant en tête l'intérêt des émetteurs à grande force d'oscillateur, nous nous concentrons ici sur l'aspect

photonique. Dans sa forme actuelle, une antenne à fil photonique reposant sur un miroir exploite une interférence à deux ondes, et donc offre au mieux une accélération de l'émission spontanée par un facteur 1.7 (*cf* chapitre 2). Pour aller plus loin, nous proposons d'exploiter un phénomène d'interférences multiples, en d'autres termes, de définir une nanocavité dans une trompette photonique. Le facteur de qualité de la résonance optique résulte d'un compromis : il s'agit d'obtenir un effet Purcell significatif tout en préservant une bande passante raisonnable.

Modèle Fabry-Perot. Nous utilisons ici le modèle Fabry-Perot développé dans la référence [31]. On considère uniquement le mode guidé fondamental M=HE_{11} avec un indice effectif n_{eff}. Comme représenté sur la Fig. 4.3(a), on définit pour ce mode une cavité Fabry-Perot de longueur totale $L = L_b + L_t$ en introduisant deux miroirs dans le guide d'onde. On note $r_b = |r_b|e^{i\phi_b}$ et $r_t = |r_t|e^{i\phi_t}$ les coefficients de réflexion modaux associés à HE_{11}. Dans la suite, la position verticale de l'émetteur optimise les effets de renforcement interférentiel du couplage au mode guidé, ce qui impose les deux conditions suivantes :

$$\frac{2L_b n_{\text{eff}}}{\lambda} + \frac{\phi_b}{2\pi} = m, \quad m \in \mathbb{N}^\star \tag{4.5}$$

$$\frac{2L_t n_{\text{eff}}}{\lambda} + \frac{\phi_t}{2\pi} = k, \quad k \in \mathbb{N}^\star \tag{4.6}$$

Dans ces conditions, le facteur de Purcell de la cavité se décompose selon $F_p = F^{\infty}_{\text{p,wg}} \times \mathcal{F}$. Le premier facteur, $F^{\infty}_{\text{p,wg}} = \Gamma^{\infty}_{\text{M}}/\Gamma_0$, correspond au facteur de Purcell généralisé d'un guide d'onde infini ; il est donné par l'équation 1.12 du chapitre 1. Le second facteur décrit l'exaltation de l'émission spontanée due aux effets d'interférence :

$$\mathcal{F} = \frac{(1+|r_b|)(1+|r_t|)}{1-|r_b r_t|}. \tag{4.7}$$

Dans le cas où $r_t = 0$, on retrouve bien l'accélération par un facteur $(1+|r_b|)$ du couplage au mode guidé. Dans le cadre du modèle Fabry-Perot, on suppose que le couplage aux modes de fuites n'est pas perturbé par les miroirs. La fraction d'émission spontanée couplée au mode de cavité construit avec les modes M se propageant vers le haut et vers le bas s'écrit alors :

$$\beta_{\text{cav}} = \frac{\beta^{\infty}_{\text{wg}}\mathcal{F}}{\beta^{\infty}_{\text{wg}}(\mathcal{F}-1)+1}, \tag{4.8}$$

où $\beta^{\infty}_{\text{wg}}$ est la fraction d'émission spontanée couplée aux modes M pour un guide d'onde infini. La fraction de lumière $\epsilon_{\text{M}\uparrow}$ sortant de la cavité dans le mode M se propageant vers le haut peut se mettre sous la forme $\epsilon_{\text{M}\uparrow} = \beta_{\text{cav}} C_{\text{M}\uparrow}$. En notant t_t la transmission modale du miroir supérieur, le terme de collection $C_{\text{M}\uparrow}$ s'écrit :

$$C_{\text{M}\uparrow} = \frac{1}{2}\frac{|t_t|^2}{1-|r_b r_t|}\frac{1+|r_b|}{1+|r_t|}. \tag{4.9}$$

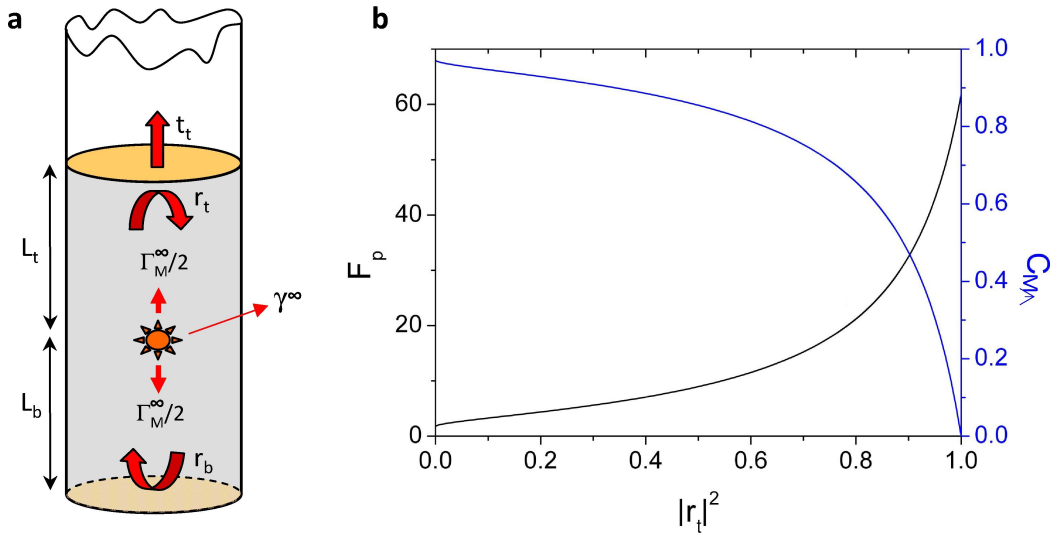

FIGURE 4.3 – **Modèle Fabry-Perot.** (a) Schéma de la géométrie considérée : une section de guide d'onde est fermée par un miroir supérieur et un miroir inférieur. Ces derniers introduisent une réflexion pour le mode guidé fondamental. Les taux d'émission spontanée représentés sont ceux du guide d'onde infini. (b) Facteur de Purcell F_p et facteur de collection $C_{\mathrm{M}\uparrow}$ à travers le miroir supérieur en fonction de $|r_t|^2$. Paramètres des calculs : $|r_b|^2 = 0.89$, $F^{\infty}_{\mathrm{p,wg}} = 0.9$, $\beta^{\infty}_{\mathrm{wg}} = 0.95$; on a de plus supposé $|t_t|^2 = 1 - |r_t|^2$.

$\lvert r_t\rvert^2$	0	0.1	0.2	0.3	0.4
F_p	1.7	3.3	4.4	5.6	7.1
$\epsilon_{\mathrm{M}\uparrow}$	0.95	0.93	0.92	0.90	0.88

TABLE 4.1 – **Facteur de Purcell F_p et efficacité de collection $\epsilon_{\mathrm{M}\uparrow}$ en fonction de la réflectivité $|r_t|^2$ du miroir supérieur.** Paramètres des calculs : $|r_b|^2 = 0.89$, $F^{\infty}_{\mathrm{p,wg}} = 0.9$, $\beta^{\infty}_{\mathrm{wg}} = 0.95$. On a supposé $|t_t|^2 = 1 - |r_t|^2$; l'efficacité de collection est calculée pour une transmission parfaite du taper.

Si on peut négliger les pertes par absorption et par conversion modale dans le miroir supérieur, alors $|t_t|^2 = 1 - |r_t|^2$. L'expression précédente se simplifie en :

$$C_{\mathrm{M}\uparrow} = \frac{1}{2}\frac{(1+|r_b|)(1-|r_t|)}{1-|r_b r_t|}. \tag{4.10}$$

Dans la suite, on considère un guide de GaAs immergé dans l'air avec $F^{\infty}_{\mathrm{p,wg}} = 0.9$ et $\beta^{\infty}_{\mathrm{wg}} = 0.95$. Comme miroir inférieur, nous retenons la couche d'or surmontée d'un espaceur de silice, qui a été discutée au chapitre précédent. Il permet d'atteindre une réflexion modale en énergie $|r_b|^2 = 0.89$. En raison de la valeur finie de $|r_b|$, la réflectivité maximale du mode supérieur est tout d'abord contrainte par un impératif de collection. La figure 4.3(b) présente le tracé simultané de F_p et $C_{\mathrm{M}\uparrow}$ en fonction de $|r_t|^2$, dans le cas où les pertes

par absorption et par conversion modale dans le miroir supérieur sont négligées. Comme attendu, lorsque $|r_t|^2$ augmente, F_p augmente et $C_{\mathrm{M}\uparrow}$ diminue. Le tableau 4.1 présente des valeurs de F_p et de l'efficacité de collection $\epsilon_{\mathrm{M}\uparrow}$ pour un miroir supérieur faiblement réfléchissant ($0 < |r_t|^2 < 0.4$). Pour $|r_t|^2 = 0.3$, il est par exemple possible d'obtenir un facteur de Purcell proche de 6 en ne dégradant la collection du mode de cavité que de 5 % par rapport à une trompette photonique "classique". L'efficacité calculée ici ne prend pas en compte la transmission modale du taper, et constitue donc une borne supérieure pour l'efficacité d'une structure complète. Toutefois, vu les transmissions très élevées discutées au chapitre précédent, l'efficacité globale sera très proche (à quelques pour cent près). Dans le dernier paragraphe de cette section, nous considérons une solution pour réaliser le miroir supérieur.

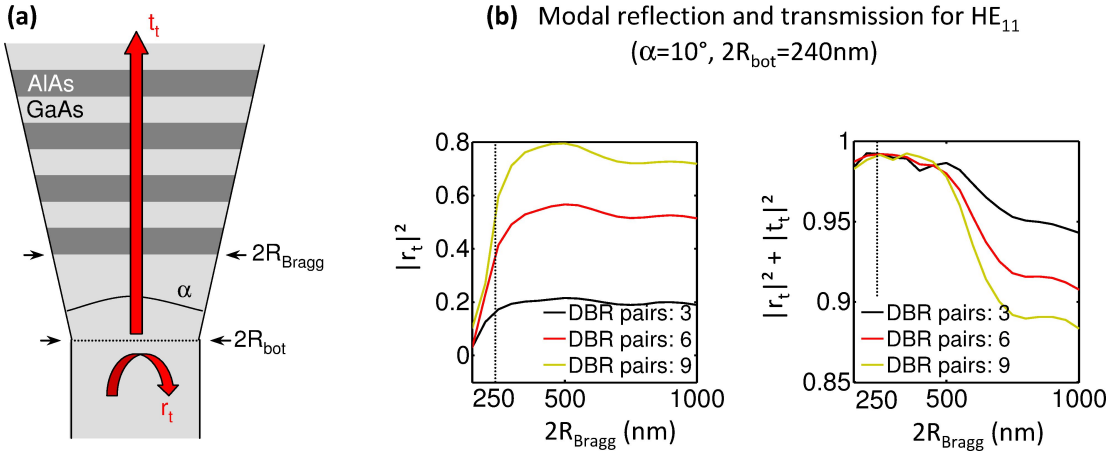

FIGURE 4.4 – **Miroir de Bragg intégré dans une trompette photonique.** (a) Schéma de la géométrie étudiée. r_t et t_t sont respectivement les coefficients de réflexion et transmission modale du miroir de Bragg. (b) $|r_t|^2$ et $|r_t|^2 + |t_t|^2$ en fonction du rayon de départ R_{Bragg} de la section avec Bragg, pour différents nombres de paires AlAs/GaAs. Les calculs sont conduits pour $\alpha = 10°$ et $2R_{\mathrm{bot}} = 240\,\mathrm{nm}$; on considère ici le mode guidé fondamental HE_{11} — adapté d'une communication privée de Niels Gregersen.

Choix du miroir supérieur. Pour réaliser la nanocavité, nous proposons d'intégrer un miroir de Bragg dans la trompette photonique, au-dessus de l'émetteur. Au vu de la discussion de la section 3.1.3 du chapitre précédent, ce choix peut sembler à première vue surprenant. Il faut cependant garder à l'esprit que nous visons une réflectivité modeste, de l'ordre de $0.3 - 0.4$. De plus, l'augmentation du diamètre lorsque l'on s'élève dans la trompette permet d'atteindre un régime où les miroirs de Bragg commencent à être efficaces. Ainsi, la Fig. 4.4 montre que dès que le diamètre atteint 500 nm, quelques paires $(4 - 5)$ de Bragg AlAs/GaAs offrent une réflectivité suffisante. De plus, il n'y a pas de pertes vers l'espace libre ou d'autres modes guidés : la transmission modale du miroir de Bragg est très proche de $1 - |r_t|^2$. Sous l'angle théorique, cette solution semble donc séduisante, reste

ensuite à réaliser ces structures. En pratique, la gravure de micropiliers de faible diamètre, réalisée assez récemment par plusieurs groupes [88, 104, 60], permet d'être optimiste, sachant que nous visons ici des miroirs composés de quelques alternances.

L'idée d'utiliser une nanocavité de facteur de qualité modéré pour obtenir un facteur de Purcell significatif sur une bande passante raisonnable a déjà été proposée ou réalisée [75, 65, 19]. Toutefois, le très fort confinement spatial dans la nanocavité conduit en général à un diagramme de rayonnement très peu directif, ce qui limite assez fortement l'efficacité de collection. Ici, la présence du taper supérieur permet de dépasser cette limitation, pour envisager des sources efficaces de photons uniques indiscernables ou de paires de photons intriqués.

4.3 Contrôle des propriétés optiques de l'émetteur par un champ externe

Dans cette section, nous discutons tout d'abord l'intérêt de l'application d'un champ externe (champ électrique, contrainte) pour contrôler les propriétés optiques d'un émetteur intégré dans une trompette photonique. En pratique, la difficulté principale est d'intégrer les éléments nécessaires à l'application de ce champ sans dégrader l'efficacité d'extraction lumineuse de l'antenne. Nous illustrons particulièrement le cas d'une trompette photonique dopée et contactée électriquement, sachant que l'application d'un champ de contrainte statique contrôlable sur la boîte ouvre des perspectives similaires.

4.3.1 Motivations

Etat de charge de la boîte. En contrôlant le potentiel électrostatique de la boîte par rapport à une électrode voisine, il est possible de stabiliser l'état de charge de la boîte de manière déterministe [109]. Dans le contexte de l'émission de photons uniques, ceci permet de maximiser l'efficacité externe de la source, en évitant que l'état de charge de la boîte (et donc la longueur d'onde d'émission) ne fluctue au cours du temps. Au-delà de cette application, la stabilisation d'un porteur de charge dans la boîte est également importante. En effet, cette charge résidente porte un spin et la recombinaison optique d'un trion peut être mise à profit pour réaliser une interface entre un qubit localisé (le spin) et un qubit volant (le photon) [23, 33].

Longueur d'onde d'un ou plusieurs émetteurs. Le contrôle fin de la longueur d'onde d'émission est nécessaire si on souhaite faire interférer des photons uniques issus de sources différentes. En effet, si on utilise des boîtes quantiques auto-assemblées, la dispersion inhomogène inhérente à ces émetteurs impose l'application d'un champ externe pour amener les différentes sources en résonance. Un tel contrôle facilite également les expériences de spectroscopie résonante sur boîte unique : on scanne alors l'énergie de l'émetteur et le laser

reste stable. En pratique, ce contrôle peut être obtenu en appliquant un champ électrique sur la boîte, qui modifie l'énergie d'émission via l'effet Starck confiné quantique [29]. De manière alternative, un champ de contrainte, qui, suivant sa structure, agit sur le gap des matériaux et/ou sur l'énergie de la bande de valence permet d'obtenir un effet similaire. Dans ce contexte, la large bande passante de l'approche fil photonique est ici cruciale : elle permet de préserver une extraction efficace de la lumière lorsque la fréquence de l'émetteur est modifiée.

De plus, lorsque plusieurs émetteurs sont couplés à un même canal optique (ici le mode fondamental guidé par le fil photonique), on peut envisager de mettre évidence des phénomènes cohérents collectifs, comme la superradiance ou la subradiance. Pour que ce couplage soit efficace, il est nécessaire de placer les émetteurs en résonance.

Splitting de structure fine. Ce point, critique pour la génération de paires de photons intriqués, a déjà été abordé au paragraphe 4.2.2.

Injection électrique des porteurs de charge. Pour utiliser une source de photons uniques dans un protocole de cryptographie quantique, ou comme source de flux lumineux calibrée, il est préférable en pratique que l'injection des porteurs dans la boîte soit réalisée par une impulsion électrique. Les éléments à intégrer à la structure (dopage électrique et prise de contacts) sont similaires à ceux nécessaires à l'application d'un champ électrique sur la boîte.

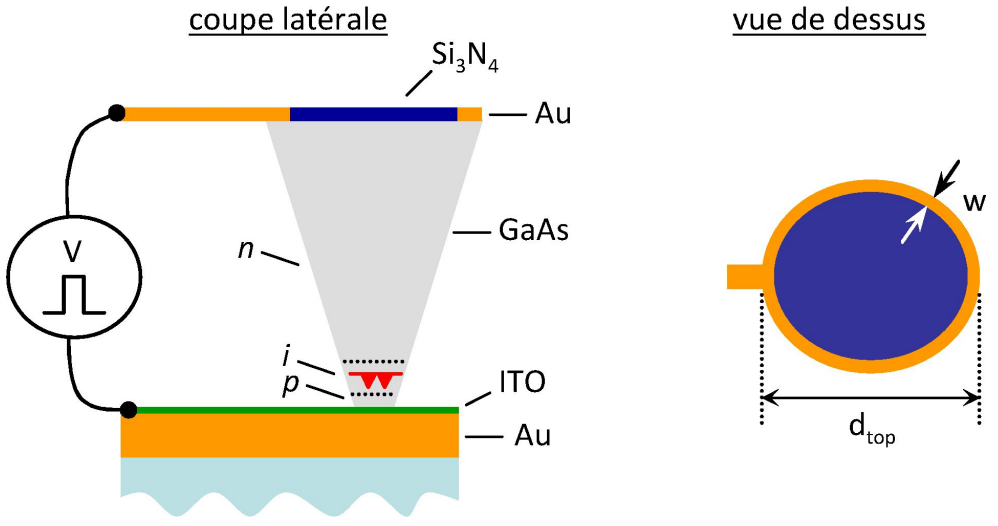

FIGURE 4.5 – **Trompette photonique contactée électriquement.** Le miroir inférieur est utilisé comme électrode. Le contact supérieur est réalisé avec une électrode annulaire, qui perturbe très peu le mode Gaussien fondamental.

4.3.2 Trompette photonique contactée électriquement

La figure 4.5 propose un *design* de trompette photonique contactée électriquement. Le matériau semiconducteur constituant la trompette est dopé et les boîtes quantiques sont intégrées dans la zone intrinsèque d'une diode p-i-n. Nous avons tout d'abord vérifié que pour des dopages de l'ordre de $10^{18}\,\mathrm{cm}^{-3}$, les pertes liées à l'absorption par porteurs libres sont négligeables (au plus quelques pour cent). La couche d'or constituant le miroir inférieur est ici utilisée comme électrode inférieure. L'espaceur de silice doit alors être remplacé par un oxyde transparent et conducteur, comme l'ITO. Les études numériques montrent que la réflectivité modale de l'ensemble est équivalente à celle du miroir or-silice. Enfin, une des difficultés principales consiste à intégrer l'électrode supérieure sans dégrader la collection des photons. Nous nous inspirons ici de l'expérience acquise pour la prise de contact sur des micropiliers gravés [12]. En effet, le mode fondamental présente un profil Gaussien, avec très peu d'intensité sur les bords de la facette : il est donc très peu perturbé par un contact annulaire. Spécifiquement, pour un diamètre $d_{\mathrm{top}} = 1.5\,\mu$m et une largeur de d'anneau $\mathrm{w} = 100\,\mathrm{nm}$, la transmission vers une optique ouverte à 0.75 n'est dégradée que de quelques pour cent. Bien sûr, ces résultats s'améliorent encore lorsque d_{top} augmente, la fraction du mode voyant l'électrode se trouvant diminuée. Pour conclure, les calculs de la Ref. [43] permettent d'espérer des efficacités d'extraction de l'ordre de 90 %. La réalisation d'une telle structure semble réaliste, mais demandera un sérieux investissement technologique.

Dans le cadre d'un projet du réseau de métrologie européen EURAMET (projet 'SIQUTE'), je suis porteur d'un 'Organisation REG' visant à réaliser une source de photons uniques pompée électriquement pour évaluer son intérêt comme étalon de faible flux lumineux. Nous sommes également partenaires du projet européen 'HANAS' dans lequel nous souhaitons réaliser une source de photons uniques brillante et agile en longueur d'onde.

Conclusion

Nous avons passé en revue dans ce dernier chapitre quelques travaux en cours qui exploitent les trompettes photoniques dans leur forme actuelle. Le couplage efficace d'une boîte quantique à un faisceau Gaussien de divergence modérée constitue bien sûr un atout pour des expériences de spectroscopie résonante. Les trompettes photoniques offrent ainsi une alternative aux structures basées sur des microcavités et leur large bande passante permet d'envisager des expériences à plusieurs faisceaux. Dans ce contexte, la cohérence de l'émetteur est un point critique. En particulier, on pourrait craindre ici que les surfaces du fils, relativement proches de l'émetteur, n'introduisent des sources supplémentaires de diffusion spectrale et/ou de déphasage. Des expériences préliminaires visant à sonder la largeur de raie de la boîte quantique sous excitation strictement résonante semblent encourageantes. A moyen terme, l'intégration d'une nanocavité dans la trompette offrira une accélération de l'émission spontanée de l'ordre d'un facteur 5 sur une bande passante d'en-

viron 10 nm. Ceci permettra d'atteindre plus facilement la limite d'indiscernabilité pour les photons émis et sera également un atout pour réaliser une source brillante de paires de photons intriqués émettant dans un mode spatial Gaussien. Un autre axe de recherche prometteur consiste à appliquer un champ externe (champ électrique ou contrainte du matériau) sur la boîte quantique pour contrôler ses propriétés optiques (état de charge, longueur d'onde, *splitting* de structure fine). Notre approche non-résonante permet ici de préserver une grande efficacité d'extraction lorsque la longueur d'onde d'émission de la boîte est modifiée. Enfin, au-delà de la photonique pure, les trompettes constituent un nouveau type de système hybride, couplant un émetteur quantique et un mode de vibration discret. Les perspectives ouvertes sont là aussi très riches.

Bibliographie

[1] A. V. Akimov, A. Mukherjee, C. L. Yu, D. E. Chang, A. S. Zibrov, P. R. Hemmer, H. Park, and M. D. Lukin. Generation of single optical plasmons in metallic nanowires coupled to quantum dots. *Nature*, 450 :402, 2007.

[2] N. Akopian, N. H. Lindner, E. Poem, Y. Berlatzky, J. Avron, D. Gershoni, B. D. Gerardot, and P. M. Petroff. Entangled photon pairs from semiconductor quantum dots. *Phys. Rev. Lett.*, 96 :130501, 2006.

[3] V. R. Almeida, R. R. Panepucci, and M. Lipson. Nanotaper for compact mode conversion. *Opt. Lett.*, 28 :1302, 2003.

[4] V. R. Almeida, Q. Xu, C. A. Barrios, and M. Lipson. Guiding and confining light in void nanostructure. *Opt. Lett.*, 29 :1209, 2004.

[5] K. Aoki, D. Guimard, M. Nishioka, M. Nomura, S. Iwamoto, and Y. Arakawa. Coupling of quantum-dot light emission with a three-dimensional photonic-crystal nanocavity. *Nature Photon.*, 2 :688, 2008.

[6] A. Auffèves, J.-M. Gérard, and J.-P. Poizat. Pure emitter dephasing : A resource for advanced solid-state single-photon sources. *Phys. Rev. A*, 79 :053838, 2009.

[7] A. Auffèves-Garnier, C. Simon, J.-M. Gérard, and J.-P. Poizat. Giant optical nonlinearity induced by a single two-level system interacting with a cavity in the purcell regime. *Phys. Rev. A*, 75 :053823, 2007.

[8] A. Badolato, K. Hennessy, M. Atatüre, J. Dreiser, E. Hu, P. M. Petroff, and A. Imamoğlu. Deterministic Coupling of Single Quantum Dots to Single Nanocavity Modes. *Science*, 308 :1158, 2005.

[9] W. L. Barnes, G. Björk, J. M. Gérard, P. Jonsson, J. A. E. Wasey, P. T. Worthing, and V. Zwiller. Solid-state single photon sources : light collection strategies. *Eur. Phys. J. D*, 18 :197, 2002.

[10] A. J. Bennett, M. A. Pooley, R. M. Stevenson, M. B. Ward, R. B. Patel, A. Boyer de la Giroday, N. Sköld, I. Farrer, C. A. Nicoll, D. A. Ritchie, and A. J. Shields. Electric-field-induced coherent coupling of the exciton states in a single quantum dot. *Nature Phys.*, 6 :947, 2010.

[11] J. Bleuse, J. Claudon, M. Creasey, N. S. Malik, J.-M. Gérard, I. Maksymov, J.-P. Hugonin, and P. Lalanne. Inhibition, Enhancement, and Control of Spontaneous Emission in Photonic Nanowires. *Phys. Rev. Lett.*, 106 :103601, 2011.

[12] C. Böckler, S. Reitzenstein, C. Kistner, R. Debusmann, A. Löffler, T. Kida, S. Höfling, A. Forchel, L. Grenouillet, J. Claudon, and J. M. Gérard. Electrically driven high-Q quantum dot-micropillar cavities. *Appl. Phys. Lett.*, 92 :091107, 2008.

[13] R. Bose, D. Sridharan, H. Kim, G. S. Solomon, and E. Waks. Low-Photon-Number Optical Switching with a Single Quantum Dot Coupled to a Photonic Crystal Cavity. *Phys. Rev. Lett.*, 108 :227402, 2012.

[14] X. Brokmann, L. Coolen, M. Dahan, and J. P. Hermier. Measurement of the Radiative and Nonradiative Decay Rates of Single CdSe Nanocrystals through a Controlled Modification of their Spontaneous Emission. *Phys. Rev. Lett.*, 93 :107403, 2004.

[15] G. Bulgarini, M. E. Reimer, T. Zehender, M. Hocevar, E. P. A. M. Bakkers, L. P. Kouwenhoven, and V. Zwiller. Spontaneous emission control of single quantum dots in bottom-up nanowire waveguides. *Appl. Phys. Lett.*, 100 :121106, 2012.

[16] G. Cassabois. *Origines et limites du modèle de l'atome artificiel pour une boîte quantique de semiconducteurs*. HDR, Université Paris VI, 2006.

[17] D. E. Chang, A. S. Sørensen, P. R. Hemmer, and M. D. Lukin. Strong coupling of single emitters to surface plasmons. *Phys. Rev. B*, 76 :035420, 2007.

[18] L. Chen and E. Towe. Nanowire lasers with distributed-Bragg-reflector mirrors. *Appl. Phys. Lett.*, 89 :053125, 2006.

[19] J. T. Choy, B. M. Hausmann, T. M. Babinec, I. Bulu, M. Khan, P. Maletinsky, A. Yacoby, and M. Lončar. Enhanced single-photon emission from a diamond–silver aperture. *Nature Photon.*, 5 :738, 2011.

[20] D. Y. Chu and S. T. Ho. Spontaneous emission from excitons in cylindrical dielectric wave-guides and the spontaneous-emission factor of microcavity ring lasers. *J. Opt. Soc. Am. B*, 10 :381, 1993.

[21] J. Claudon, J. Bleuse, N. S. Malik, M. Bazin, P. Jaffrennou, N. Gregersen, C. Sauvan, P. Lalanne, and J.-M. Gérard. A highly efficient single-photon source based on a quantum dot in a photonic nanowire. *Nature Photon.*, 4 :174, 2010.

[22] J. Claudon, N. Gregersen, P. Lalanne, and J.-M. Gérard. Harnessing Light with Photonic Nanowires : Fundamentals and Applications to Quantum Optics. *ChemPhysChem*, 14 :2393, 2013.

[23] K. De Greve, L. Yu, P. L. McMahon, J. S. Pelc, C. M. Natarajan, N. Y. Kim, E. Abe, S. Maier, C. Schneider, M. Kamp, S. Höfling, R. H. Hadfield, A. Forchel, M. M. Fejer, and Y. Yamamoto. Quantum-dot spin-photon entanglement via frequency downconversion to telecom wavelength. *Nature*, 491 :421, 2012.

[24] A. Dousse, L. Lanco, J. Suffczyński, E. Semenova, A. Miard, A. Lemaître, I. Sagnes, C. Roblin, J. Bloch, and P. Senellart. Controlled Light-Matter Coupling for a Single Quantum Dot Embedded in a Pillar Microcavity Using Far-Field Optical Lithography. *Phys. Rev. Lett.*, 101 :267404, 2008.

[25] A. Dousse, J. Suffczyński, A. Beveratos, O. Krebs, A. Lemaître, I. Sagnes, J. Bloch, P. Voisin, and P. Senellart. Ultrabright source of entangled photon pairs. *Nature*, 466 :217, 2010.

[26] D. J. P. Ellis, R. M. Stevenson, Young, A. J. Shields, P. Atkinson, and D. A. Ritchie. Control of fine-structure splitting of individual InAs quantum dots by rapid thermal annealing. *Appl. Phys. Lett.*, 90 :011907, 2007.

[27] D. Englund, A. Faraon, I. Fushman, N. Stoltz, P. Petroff, and J. Vučković. Controlling cavity reflectivity with a single quantum dot. *Nature*, 6 :857, 2007.

[28] D. Englund, D. Fattal, E. Waks, G. Solomon, B. Y. Zhang, T. Nakaoka, Y. Arakawa, Y. Yamamoto, and J. Vučković. Controlling the Spontaneous Emission Rate of Single Quantum Dots in a Two-Dimensional Photonic Crystal. *Phys. Rev. Lett.*, 95 :013904, 2005.

[29] J. J. Finley, M. Sabathil, P. Vogl, G. Abstreiter, R. Oulton, A. I. Tartakovskii, D. J. Mowbray, M. S. Skolnick, S. L. Liew, A. G. Cullis, and M. Hopkinson. Quantum-confined stark shifts of charged exciton complexes in quantum dots. *Phys. Rev. B*, 70 :201308(R), 2004.

[30] I. Friedler, P. Lalanne, J. P. Hugonin, J. Claudon, J. M. Gérard, A. Beveratos, and I. Robert-Philip. Efficient photonic mirrors for semiconductor nanowires. *Opt. Lett.*, 33 :2635, 2008.

[31] I. Friedler, C. Sauvan, J. P. Hugonin, P. Lalanne, J. Claudon, and J. M. Gérard. Solid-state single photon sources : the nanowire antenna. *Opt. Express*, 17 :2095, 2009.

[32] C. H. Gan, J. P. Hugonin, and P. Lalanne. Proposal for Compact Solid-State III-V Single-Plasmon Sources. *Phys. Rev. X*, 2 :021008, 2012.

[33] W. B. Gao, P. Fallahi, E. Togan, J. Miguel-Sanchez, and A. Imamoğlu. Observation of entanglement between a quantum dot spin and a single photon. *Nature*, 491 :426, 2012.

[34] O. Gazzano, S. Michaelis de Vasconcellos, C. Arnold, A. Nowak, E. Galopin, I. Sagnes, L. Lanco, A. Lemaître, and P. Senellart. Bright solid-state sources of indistinguishable single photons. *Nature Comm.*, 4 :1425, 2013.

[35] O. Gazzano, S. Michaelis de Vasconcellos, K. Gauthron, C. Symonds, J. Bloch, P. Voisin, J. Bellessa, A. Lemaître, and P. Senellart. Evidence for Confined Tamm Plasmon Modes under Metallic Microdisks and Application to the Control of Spontaneous Optical Emission. *Phys. Rev. Lett.*, 107 :247402, 2011.

[36] J. M. Gérard. Solid-State Cavity-Quantum Electrodynamics with Self-Assembled Quantum Dots. *Top. Appl. Phys.*, 90 :269, 2003.

[37] J. M. Gérard, B. Sermage, B. Gayral, B. Legrand, E. Costard, and V. Thierry-Mieg. Enhanced Spontaneous Emission by Quantum Boxes in a Monolithic Optical Microcavity. *Phys. Rev. Lett.*, 81 :1110, 1998.

[38] V. Giesz, O Gazzano, A. K. Nowak, S. L. Portalupi, A. Lemaître, I. Sagnes, L. Lanco, and P. Senellart. Influence of the purcell effect on the purity of bright single photon sources. *Appl. Phys. Lett.*, 103 :033113, 2013.

[39] N. Gisin, G. Ribordy, W. Tittel, and H. Zbinden. Quantum cryptography. *Rev. Mod. Phys.*, 74 :145, 2002.

[40] A. Gonzalez-Tudela, D. Martion-Cano, E. Moreno, L. Martin-Moreno, C. Tejedor, and F. J. Garcia-Vidal. Entanglement of two qubits mediated by one-dimensional plasmonic waveguides. *Phys. Rev. Lett.*, 106 :020501, 2011.

[41] P. Goy, J. M. Raimond, M. Gross, and S. Haroche. Observation of Cavity-Enhanced Single-Atom Spontaneous Emission. *Phys. Rev. Lett.*, 50 :1903, 1983.

[42] N. Gregersen, T. R. Nielsen, J. Claudon, J. M. Gérard, and J. Mørk. Controlling the emission profile of a nanowire with a conical taper. *Opt. Lett.*, 33 :1693, 2008.

[43] N. Gregersen, T. R. Nielsen, J. Mørk, J. Claudon, and J.-M. Gérard. Designs for high-efficiency electrically pumped photonic nanowire single-photon sources. *Opt. Express*, 18 :21204, 2010.

[44] A. Greilich, M. Schwab, T. Berstermann, T. Auer, R. Oulton, D. R. Yakovlev, M. Bayer, V. Stavarache, D. Reuter, and A. Wieck. Tailored quantum dots for entangled photon pair creation. *Phys. Rev. B*, 73 :045323, 2006.

[45] Y.-M. He, Y. He, Y.-J. Wei, D. Wu, M. Atatüre, C. Schneider, S. Höfling, M. Kamp, C.-Y. Lu, and J.-W. Pan. On-demand semiconductor single-photon source with near-unity indistinguishability. *Nature Nanotech.*, 8 :213, 2013.

[46] J. Heinrich, A. Huggenberger, T. Heindel, S. Reitzenstein, S. Höfling, L. Worschech, and A. Forchel. Single photon emission from positioned GaAs/AlGaAs photonic nanowires. *Appl. Phys. Lett.*, 96 :211117, 2010.

[47] K. Hennessy, A. Badolato, M. Winger, D. Gerace, M. Atatüre, S. Gulde, S. Fält, E. L. Hu, and A. Imamoğlu. Quantum nature of a strongly coupled single quantum dot-cavity system. *Nature*, 445 :896, 2007.

[48] S. T. Ho, S. L. McCall, and R. E. Slusher. Spontaneous emission from excitons in thin dielectric layers. *Opt. Lett.*, 18 :909, 1993.

[49] U. Hohenester, A. Laucht, M. Kaniber, N. Hauke, A. Neumann, A. Mohtashami, M. Seliger, M. Bichler, and J. J. Finley. Phonon-assisted transitions from quantum dot excitons to cavity photons. *Phys. Rev. B(R)*, 80 :201311, 2009.

[50] J. Houel, A. V. Kuhlmann, L. Greuter, F. Xue, M. Poggio, B. D. Gerardot, P. A. Dalgarno, A. Badolato, P. M. Petroff, A. Ludwig, D. Reuter, A. D. Wieck, and R. J. Warburton. Probing Single-Charge Fluctuations at a GaAs/AlAs Interface Using Laser Spectroscopy on a Nearby InGaAs Quantum Dot. *Phys. Rev. Lett.*, 108 :107401, 2012.

[51] J. Johansen, S. Stobbe, I. S. Nikolaev, T. Lund-Hansen, P. T. Kristensen, J. M. Hvam, W. L. Vos, and P. Lodahl. Size dependence of the wavefunction of self-assembled InAs quantum dots from time-resolved optical measurements. *Phys. Rev. B*, 77 :073303, 2008.

[52] H. J. Kimble. The quantum internet. *Nature*, 453 :1023, 2008.

[53] E. Knill, R. Laflamme, and G. J. Milburn. A scheme for efficient quantum computation with linear optics. *Nature*, 409 :46, 2000.

[54] P. Kolchin, R. F. Oulton, and X. Zhang. Nonlinear Quantum Optics in a Waveguide : Distinct Single Photons Strongly Interacting at the Single Atom Level. *Phys. Rev. Lett.*, 106 :113601, 2011.

[55] A. V. Kuhlmann, J. Houel, A. Ludwig, L. Greuter, D. Reuter, A. D. Wieck, M. Poggio, and R. J. Warburton. Charge noise and spin noise in a semiconductor quantum device. *Nature Phys.*, 9 :570, 2013.

[56] P. Lalanne, S. Mias, and J. P. Hugonin. Two physical mechanisms for boosting the quality factor to cavity volume ratio of photonic crystal microcavities. *Opt. Express*, 12 :458, 2004.

[57] G. Lecamp, P. Lalanne, and J. P. Hugonin. Very Large Spontaneous-Emission beta Factors in Photonic-Crystal Waveguides. *Phys. Rev. Lett.*, 99 :023902, 2007.

[58] K. G. Lee, X. W. Chen, H. Eghlidi, P. Kukura, R. Lettow, A. Renn, V. Sandoghdar, and S. Götzinger. A planar dielectric antenna for directional single-photon emission and near-unity collection efficiency. *Nature Photon.*, 5 :166, 2011.

[59] M. D. Leistikow, A. P. Mosk, E. Yeganegi, S. R. Huisman, A. Lagendijk, and W. L. Vos. Inhibited Spontaneous Emission of Quantum Dots Observed in a 3D Photonic Band Gap. *Phys. Rev. Lett.*, 107 :193903, 2011.

[60] M. Lermer, N. Gregersen, F. Dunzer, S. Reitzenstein, S. Höfling, J. Mørk, L. Worschech, M. Kamp, and A. Forchel. Bloch-Wave Engineering of Quantum Dot Micropillars for Cavity Quantum Electrodynamics Experiments. *Phys. Rev. Lett.*, 108 :057402, 2012.

[61] J. Li, T. P. White, L. O'Faolain, A. Gomez-Iglesias, and T. F. Krauss. Systematic design of flat band slow light in photonic crystal waveguides. *Optics Express*, 16 :6228, 2008.

[62] Y. Li, F. Qian, J. Xiang, and C. M. Lieber. Nanowire electronic and optoelectronic devices. *Materials Today*, 9 :18, 2006.

[63] V. Loo, C. Arnold, O. Gazzano, A. Lemaître, I. Sagnes, O. Krebs, P. Voisin, P. Senellart, and L. Lanco. Optical nonlinearity for few-photon pulses on a quantum dot-pillar cavity device. *Phys. Rev. Lett.*, 109 :166806, 2012.

[64] T. Lund-Hansen, S. Stobbe, B. Julsgaard, H. Thyrrestrup, T. Sünner, M. Kamp, A. Forchel, and P. Lodahl. Experimental Realization of Highly Efficient Broadband Coupling of Single Quantum Dots to a Photonic Crystal Waveguide. *Phys. Rev. Lett.*, 101 :113903, 2008.

[65] I. S. Maksymov, M. Besbes, J. P. Hugonin, J. Yang, A. Beveratos, I. Sagnes, I. Robert-Philip, and P. Lalanne. Metal-Coated Nanocylinder Cavity for Broadband Nonclassical Light Emission. *Phys. Rev. Lett.*, 105 :180502, 2010.

[66] V. S. C. Manga Rao and S. Hughes. Single quantum-dot Purcell factor and β factor in a photonic crystal waveguide. *Phys. Rev. B*, 75 :205437, 2007.

[67] A. V. Maslov, M. I. Bakunov, and C. Z. Ning. Distribution of optical emission between guided modes and free space in a semiconductor nanowire. *J. Appl. Phys.*, 99 :024314, 2006.

[68] A. V. Maslov and C. Z. Ning. Far-field emission of a semiconductor nanowire laser. *Opt. Lett.*, 29 :572, 2004.

[69] C. Matthiesen, A. N. Vamivakas, and M. Atatüre. Subnatural linewidth single photons from a quantum dot. *Phys. Rev. Lett.*, 108 :093602, 2012.

[70] S. Mazoyer, J. P. Hugonin, and P. Lalanne. Disorder-Induced Multiple Scattering in Photonic-Crystal Waveguides. *Phys. Rev. Lett.*, 103 :063903, 2009.

[71] P. Michler, A. Kiraz, C. Becher, W. V. Schoenfeld, P. M. Petroff, L. Zhang, E. Hu, and A. Imamoğlu. A Quantum Dot Single-Photon Turnstile Device. *Science*, 290 :2282, 2000.

[72] E. Moreau, I. Robert, J. M. Gérard, I. Abram, L. Manin, and V. Thierry-Mieg. Single-mode solid-state single photon source based on isolated quantum dots in pillar microcavities. *Appl. Phys. Lett.*, 79 :2865, 2001.

[73] M. Munsch, J. Claudon, J. Bleuse, N. S. Malik, E. Dupuy, J.-M. Gérard, Y. Chen, N. Gregersen, and J. Mørk. Linearly Polarized, Single-Mode Spontaneous Emission in a Photonic Nanowire. *Phys. Rev. Lett.*, 108 :077405, 2012.

[74] M. Munsch, N. S. Malik, J. Bleuse, E. Dupuy, A. Delga, J.-M. Gérard, J. Claudon, N. Gregersen, and J. Mørk. Dielectric GaAs-antenna ensuring an efficient broadband coupling between an InAs quantum-dot light emitter and a gaussian optical beam. *Phys. Rev. Lett.*, 110 :177402, 2013.

[75] M. P. Nezhad, A. Simic, O. Bondarenko, B. Slutsky, A. Mizrahi, L. Feng, V. Lomakin, and Y. Fainman. Room-temperature subwavelength metallo-dielectric lasers. *Nature Photon.*, 4 :395, 2010.

[76] H. S. Nguyen, G. Sallen, C. Voisin, Ph. Roussignol, C. Diederichs, and G. Cassabois. Ultra-coherent single photon source. *Appl. Phys. Lett.*, 99 :261904, 2011.

[77] S. Noda, M. Fujita, and T. Asano. Spontaneous-emission control by photonic crystals and nanocavities. *Nature Photon.*, 1 :449, 2009.

[78] M. Pelton, C. Santori, J. Vučković, B. Zhang, G. S. Solomon, J. Plant, and Y. Yamamoto. Efficient Source of Single Photons : A Single Quantum Dot in a Micropost Microcavity. *Phys. Rev. Lett.*, 89 :233602, 2002.

[79] E. Peter, S. Laurent, J. Bloch, J. Hours, S. Varoutsis, I. Robert-Philip, A. Beveratos, A. Lemaître, A. Cavanna, G. Patriarche, P. Senellart, and D. Martrou. Fast radiative quantum dots : From single to multiple photon emission. *Appl. Phys. Lett.*, 90 :223118, 2007.

[80] E. Peter, P. Senellart, D. Martrou, A. Lemaître, J. Hours, J. M. Gérard, and J Bloch. Exciton-Photon Strong-Coupling Regime for a Single Quantum Dot Embedded in a Microcavity. *Phys. Rev. Lett.*, 95 :067401, 2005.

[81] E. M. Purcell. Proceedings of the american physical society. *Phys. Rev.*, 69 :674, 1946.

[82] Q. Quan, I. Bulu, and M. Lončar. Broadband waveguide QED system on a chip. *Phys. Rev. A*, 80 :011810, 2009.

[83] M. E. Reimer, G. Bulgarini, N. Akopian, M. Hocevar, M. B. Bavinck, M. A. Verheijen, E. P. A. M. Bakkers, L. P. Kouwenhoven, and V. Zwiller. Bright single-photon sources in bottom-up tailored nanowires. *Nature Comm.*, 3 :737, 2012.

[84] A. Reinhard, T. Volz, M. Winger, A. Badolato, K. J. Hennessy, E. L. Hu, and A. Imamoğlu. Strongly correlated photons on a chip. *Nature Photon.*, 6 :93, 2011.

[85] J. P. Reithmaier, G. Sęk, A. Löffler, C. Hofmann, S. Kuhn, S. Reitzenstein, L. V. Keldysh, V. D. Kulakovskii, T. L. Reinecke, and A. Forchel. Strong coupling in a single quantum dot–semiconductor microcavity system. *Nature*, 432 :197, 2004.

[86] D. Roy. Two-Photon Scattering by a Driven Three-Level Emitter in a One-Dimensional Waveguide and Electromagnetically Induced Transparency. *Phys. Rev. Lett.*, 106 :053601, 2011.

[87] K. Sanaka, A. Pawlis, T. D. Ladd, K. Lischka, and Y. Yamamoto. Indistinguishable Photons from Independent Semiconductor Nanostructures. *Phys. Rev. Lett.*, 103 :053601, 2009.

[88] C. Santori, D. Fattal, J. Vučković, G. S. Solomon, and Y. Yamamoto. Indistinguishable photons from a single-photon device. *Nature*, 419 :594, 2002.

[89] C. Santori, M. Pelton, G. Solomon, Y. Dale, and Y. Yamamoto. Triggered single photons from a quantum dot. *Phys. Rev. Lett.*, 86 :1502, 2001.

[90] E. Snitzer. Cylindrical Dielectric Waveguide Modes. *JOSA*, 51 :491, 1961.

[91] G. S. Solomon, M. Pelton, and Y. Yamamoto. Single-mode Spontaneous Emission from a Single Quantum Dot in a Three-Dimensional Microcavity. *Phys. Rev. Lett.*, 86 :3903, 2001.

[92] R. M. Stevenson, A. J. Hudson, A. J. Bennett, R. J. Young, C. A. Nicoll, D. A. Ritchie, and A. J. Shields. Evolution of Entanglement Between Distinguishable Light States. *Phys. Rev. Lett.*, 101 :170501, 2008.

[93] R. M. Stevenson, R. J. Young, P. Atkinson, K. Cooper, D. A. Ritchie, and A. J. Shields. A semiconductor source of triggered entangled photon pairs. *Nature*, 439 :179, 2006.

[94] T. H. Stievater, X. Li, J. R. Guest, D. G. Steel, D. Gammon, D. S. Katzer, and D. Park. Wavelength modulation spectroscopy of single quantum dots. *Appl. Phys. Lett.*, 80 :1876, 2002.

[95] S. Strauf, N. G. Stoltz, M. T. Rakher, L. A. Coldren, P. M. Petroff, and D. Bouwmeester. High-frequency single–photon source with polarization control. *Nature Photon.*, 1 :704, 2007.

[96] J. Suffczyński, A. Dousse, K. Gauthron, A. Lemaitre, I. Sagnes, L. Lanco, J. Bloch, P. Voisin, and P. Senellart. Origin of the Optical Emission within the Cavity Mode of Coupled Quantum Dot-Cavity Systems. *Phys. Rev. Lett.*, 103 :027401, 2009.

[97] M. Tchernycheva, G. E. Cirlin, G. Patriarche, L. Travers, V. Zwiller, U. Perinetti, and J.-C. Harmand. Growth and Characterization of InP Nanowires with InAsP Insertions. *Nano Lett.*, 7 :1500, 2007.

[98] C. Thelander, P. Agarwal, S. Brongersma, J. Eymery, L. F. Feiner, A. Forchel, M. Scheffler, W. Riess, B. J. Ohlsson, U. Gösele, and L. Samuelson. Nanowire-based one-dimensional electronics. *Materials Today*, 9 :28, 2006.

[99] P. Treutlein, C. Genes, K. Hammerer, M. Poggio, and P. Rabl. Hybrid mechanical systems. *arXiv :1210.4151*.

[100] A. Tribu, G. Sallen, T. Aichele, R. André, J.-P. Poizat, C. Bougerol, S. Tatarenko, and K. Kheng. A High-Temperature Single-Photon Source from Nanowire Quantum Dots. *Nano Lett.*, 8 :4326, 2008.

[101] R. Trotta, E. Zallo, C. Ortix, P. Atkinson, J. D. Plumhof, J. van den Brink, A. Rastelli, and O. G. Schmidt. Universal recovery of the energy-level degeneracy of bright excitons in InGaAs quantum dots without a structure symmetry. *Phys. Rev. Lett.*, 101 :111912, 2012.

[102] Q. A. Turchette, R. J. Thompson, and H. J. Kimble. One dimensional atoms. *Appl. Phys. B*, 60 :S1, 1995.

[103] S. Varoutsis, S. Laurent, P. Kramper, A. Lemaître, I. Sagnes, I. Robert-Philip, and I. Abram. Restoration of photon indistinguishability in the emission of a semiconductor quantum dot. *Phys. Rev. B(R)*, 72 :041303(R), 2005.

[104] S. Varoutsis, S. Laurent, I. Sagnes, A. Lemaître, L. Ferlazzo, C. Mériadec, G. Patriarche, I. Robert-Philip, and I. Abram. Reactive-ion etching of high-Q and submicron-diameter GaAs/AlAs micropillars. *J. Vac. Sci. Technol. B*, 23 :2499, 2005.

[105] E. Viasnoff-Schwoob, C. Weisbuch, H. Benisty, S. Olivier, S. Varoutsis, I. Robert-Philip, R. Houdré, and C. J. M. Smith. Spontaneous Emission Enhancement of Quantum Dots in a Photonic Crystal Wire. *Phys. Rev. Lett.*, 95 :183901, 2005.

[106] T. Volz, A. Reinhard, M. Winger, A. Badolato, K. J. Hennessy, E. L. Hu, and A. Imamoğlu. Ultrafast all-optical switching by single photons. *Nature Photon.*, 6 :605, 2012.

[107] Q. Wang, S. Stobbe, and P. Lodahl. Mapping the Local Density of Optical States of a Photonic Crystal with Single Quantum Dots. *Phys. Rev. Lett.*, 107 :167404, 2011.

[108] Q. Wang, S. Stobbe, H. Thyrrestrup, H. Hofmann, M. Kamp, T. W. Schlereth, S. Höfling, and P. Lodahl. Highly anisotropic decay rates of single quantum dots in photonic crystal membranes. *Optics Lett.*, 35 :2768, 2010.

[109] R. J. Warburton, C. Schaflein, D. Haft, F. Bickel, A. Lorke, K. Karrai, J. M. Garcia, W. Schoenfeld, and P. M. Petroff. Optical emission from a charge-tunable quantum ring. *Nature*, 405 :926, 2000.

[110] I. Wilson-Rae, P. Zoller, and A. Imamoğlu. Laser cooling of a nanomechanical resonator mode to its quantum ground state. *Phys. Rev. Lett.*, 92 :075507, 2004.

[111] M. Winger, T. Volz, G. Tarel, S. Portolan, A. Badolato, K. J. Hennessy, E. L. Hu, A. Beveratos, J. Finley, V. Savona, and A. Imamoğlu. Explanation of Photon Correlations in the Far-Off-Resonance Optical Emission from a Quantum-Dot-Cavity System. *Phys. Rev. Lett.*, 103 :207403, 2009.

[112] E. Yablonovitch. Inhibited Spontaneous Emission in Solid-State Physics and Electronics. *Phys. Rev. Lett.*, 58 :2059, 1987.

[113] E. Yablonovitch. Photonic band-gap structures. *J. Opt. Soc. Am. B*, 10 :283, 1993.

[114] E. Yablonovitch, T. J. Gmitter, and R. Bhat. Inhibited and Enhanced Spontaneous Emission from Optically Thin AlGaAs/GaAs Double Heterostructures. *Phys. Rev. Lett.*, 61 :2546, 1988.

[115] R. Yan, D. Gargas, and P. Yang. Nanowire photonics. *Nature Photon.*, 3 :569, 2009.

[116] I. Yeo, P.-L. de Assis, A. Gloppe, E. Dupont-Ferrier, P. Verlot, N. S. Malik, E. Dupuy, J. Claudon, J.-M. Gérard, A. Auffèves, G. Nogues, S. Seidelin, J.-Ph. Poizat, O. Arcizet, and M. Richard. Strain-mediated coupling in a quantum dot-mechanical oscillator hybrid system. *Nature Nanotech.*, 9 :106, 2014.

[117] I. Yeo, N. S. Malik, M. Munsch, E. Dupuy, J. Bleuse, Y.-M. Niquet, J.-M. Gérard, J. Claudon, E. Wagner, S. Seidelin, A. Auffèves, J.-P. Poizat, and G. Nogues. Surface effects in a semiconductor photonic nanowire and spectral stability of an embedded single quantum dot. *Appl. Phys. Lett.*, 99 :233106, 2011.

[118] T. Yoshie, A. Scherer, J. Hendrickson, G. Khitrova, H. M. Gibbs, G. Rupper, C. Ell, O. B. Shchekin, and D. G. Deppe. Vacuum rabi splitting with a single quantum dot in a photonic crystal nanocavity. *Nature*, 432 :200, 2004.

[119] R. J. Young, M. R. Stevenson, P. Atkinson, K. Cooper, D. A. Ritchie, and A. J. Shields. Improved fidelity of triggered entangled photons from single quantum dots. *New J. Phys.*, 8 :1367, 2006.

[120] Z. L. Yuan, B. E. Kardynal, R. M. Stevenson, A. J. Shields, C. J. Lobo, K. Cooper, N. S. Beattie, D. A. Ritchie, and M. Pepper. Electrically driven single-photon source. *Science*, 295 :102, 2002.

[121] J. P. Zhang, D. Y. Chu, S. L. Wu, S. T. Ho, W. G. Bi, C. W. Tu, and R. C. Tiberio. Photonic-Wire Laser. *Phys. Rev. Lett.*, 75 :2678, 1995.

[122] H. Zheng, D. J. Gauthier, and H. U. Baranger. Cavity-Free Photon Blockade Induced by Many-Body Bound States. *Phys. Rev. Lett.*, 107 :223601, 2011.